ULTRASTABLE HIGH FINESSE CAVITIES FOR LASER FREQUENCY STABILIZATION

Sarika Pugla

May 2007

Contents

List of Figures

List of Tables

Acknowledgements

It is a pleasure to thank many people who have made this thesis possible.

It is difficult to overstate my gratitude to my Ph.D. supervisor, Dr. Daniel Segal. With his enthusiasm, inspiration, and great efforts to explain things clearly and simply, he helped me develop a great understanding of my PhD work and quantum optics as a whole. Throughout my thesis writing period, he provided encouragement, sound advice, good teaching, and lots of good ideas to keep on going. I would have been lost without him.

I would also like to thank Dr. Mark Oxborrow and Dr. Stephen Webster at National Physical Laboratory, Teddington for giving me an opportunity to work on such interesting experiments and supporting me all through the experiments. Furthermore, I express my gratitude to people who taught me physics: my graduate teachers at Dayalbagh Educational Institute, Agra (especially, Prof. V. G. Das, Professor Satish Kumar, Dr. C.P. Nigam, Dr. Sukhdev Roy, Dr. Markan, Prof. Ram Kumar and Dr. Vibha Satsangi). I wish to thank in addition Dr. Ling Hao, Dr. John Gallop, Dr. John Macfarlne, Dr. Patrick Gill and Dr. Hugh Klein for their extended support and help during my work at National Physical Laboratory.

I am indebted to my many student colleagues for providing emotional and mental support. I am especially grateful to Dr. Eoin Phillips and Dr. V. Letchumanan, at Imperial College London for providing me good ideas and the mental support that kept me going.

I wish to thank all my friends. Especially, Lizzie Brown, Giuseppe Marra, James Goldwater, Roohi Fakkruddin and Liz Anderson for helping me get through the difficult times, and for all the emotional support, camaraderie, entertainment, and caring they provided. I would again like to thank Lizzie for sending me the papers that I needed during my thesis writing period.

I am grateful to the secretaries and librarians in the National Physical Laboratory and Imperial College London, for helping the departments run smoothly and for assisting me in many different ways. Loli Sanchez and Pinku at Imperial College London deserve a special mention.

I wish to thank my entire extended family for providing a loving environ-

ment for me. Special thanks to my brother Sandeep Pugla and sister−in−law Pragati Pugla for all their love and support. My cousins, uncles and aunts have also been particularly supportive.

I am glad that my husband Vinay Dhamija can actually see what I have been doing all these years. I want to thank him for all the support that he gave me during the years I have been working on this thesis, especially all the weekends that he sacrificed to give me time to write, to think and to talk to him about the thesis.

My parents, Ramesh Chand Pugla and Shashi Pugla have been an inspiration throughout my life. They have always supported my dreams and aspirations. I'd like to thank them for all they are, and all they have done for me. To them, I dedicate this thesis.

Abstract

Lasers with stability of the order of $\approx 10^{-15}$ or more form the basis of frequency metrology and several other experiments including, gravitational wave detection, high−precision spectroscopy, tests of relativity, etc. The work described in this thesis is about the frequency stabilization of 1064nm, Nd:YAG lasers to ultra−stable, high finesse Fabry−Perot cavities using the Pound−Drever−Hall locking scheme. These lasers will be used as flywheel oscillators for optical atomic clocks. Most of the work described in this thesis is about the design and development of a stable laser using a cryogenic, all−sapphire, high finesse Fabry−Perot cavity. Two similar systems have been developed and the beat frequency between the two has been measured. This beat frequency measurement provides a measure of relative stability of the laser. A few experiments have also been performed with ULE (ultra−low expansivity) glass cavities.

Chapter 1

Introduction

Electromagnetic radiation stabilized to transitions in atoms or molecules forms the basis of modern precision measurement of time and frequency. It has been a goal for many years to use a laser in conjunction with a nearly unperturbed atom (or cloud of atoms) or an ion to create a reference that provides a very stable frequency standard.

The frequency ν of light is related to its wavelength λ by a factor c, the speed of light, through

$$\nu = \frac{c}{\lambda}. \tag{1.1}$$

In the SI system, the speed of light c has a defined value. A very stable frequency standard would thus, in turn, lead to a very stable wavelength standard. It is also possible, in principle, to compare other physical quantities, such as electric current and mass, with frequency provided the elementary electric charge, e and Planck's constant, h have defined values[1] [1]. Thus, frequency measurements can form the basis of all the other physical measurements. Presently, in the SI system only the speed of light, c has a defined value [2] , and so by definition, only length can be related to frequency. However, the construction of a very stable frequency standard could lead to the redefinition of other units in the SI system.

The most stable frequency standard developed so far, is the microwave transition based caesium atomic fountain. It has a short-term stability of about one part in 10^{15} in 1s. Only a few standards laboratories around the world have been able to develop this type of standard due to the complicated design and the costs involved. The other laboratories still use a microwave transition-based caesium atomic beam clock as the primary standard of time interval and frequency.

[1] Josephson effect can be used to relate frequency to voltage and other electrical units, and a current balance can be used to measure mass

The stability ($\Delta f/f$) of an atomic frequency standard is inversely proportional to the Quality factor Q of the reference transition that defines the frequency [3].

$$\frac{\Delta f}{f} \propto \left(\frac{1}{Q}\right)\left(\frac{1}{\sqrt{N}}\right)\left(\frac{1}{\sqrt{\tau}}\right) \tag{1.2}$$

where N is the the number of trapped atoms or ions and τ is the time interval over which the frequency is measured. Q is given by

$$Q = \frac{\nu}{\Delta\nu} \tag{1.3}$$

Where ν is the transition frequency and $\Delta\nu$ is the linewidth of the reference transition. Optical transition frequencies are 10^5 times greater than those in the microwave region of the spectrum, whereas the natural linewidth of the reference transition can still be of the order of 1Hz or less. These transitions thus offer, a much higher Q and potentially a much higher fractional frequency stability of about one part in 10^{18} [3] in a second[2].

Recent advances in high resolution optical spectroscopy have demonstrated the potential of using a narrow optical transition in an atom or an ion as the basis for an ultra-high stability frequency standard [4]. Realization of spectroscopic transition linewidths of around 1Hz or less (stabilities of $\sim 10^{-15}$) depends critically on the lasers available to probe the transition. The most-stable commercially available laser is the 1064nm diode-pumped, non-planar ring oscillator (NPRO) type Nd:YAG laser, which has a linewidth $<$ 5kHz in 5msec, corresponding to a short term stability of few parts in $\sim 10^{10}$ [5]. Such laser systems, however, cannot be used for probing an optical transition as their wavelength lies in the infra-red region of the spectrum and cannot be tuned. A laser that is broadly-tunable and commercially available is the coherent MBR110 Ti-Sapphire laser. The frequency of this laser can be tuned from 700nm to 1000nm and has a specified linewidth of $<$ 100kHz [6] (although, the linewidth measured in the laboratory is a few MHz [3]). Lasers used as local oscillators for frequency-metrology purposes, thus, need to be prestabilized. Prestabilization of a laser to an optical Fabry-Perot reference cavity can provide a suitable *flywheel*[4] oscillator for

[2]It is important to note that, changing from a microwave to an optical frequency, the Q-factor increases by a factor of 10^5, while the stability increases only by a factor $\sim 10^3$, depending on the system. This is due to other factors (systematic effects) which come into play at such levels of stability.

[3]The laser is supplied with its own tunable reference cavity to which the laser must be locked in order to achieve the best stability. The specification sheet actually specifies the measure of lock-stability as the linewidth.

[4]An oscillator that is sufficiently stable in the short term so that it can be used while the measurements are made on the reference.

frequency-metrology and high resolution spectroscopy experiments.

The work described in this thesis is on the prestabilization of lasers to ultrastable optical Fabry-Perot reference cavities using the Pound-Drever-Hall frequency stabilization scheme. The stabilization techniques applied to these lasers will be used for future frequency standards based on optical transitions, which, when completed, will exceed the performance of microwave frequency standards.

1.1 Clocks - History

According to the American National Standard for Telecommunications [7], time can be defined as *the quantity which characterizes, or is characterized by, the observed and apparently irreversible continuum of ordered events.* Time was *invented* to coordinate human activities and to understand the world around us.

> Space and time are modes by which we think, not conditions under which we live - Albert Einstein

Time and frequency signals are widely used throughout the world by scientists, navigators, industries, transportation systems, communication systems and the general public for a number of applications requiring precise time and frequency references. The technological advancements in industry, communication systems, scientific measurements and other fields require very precise and accurate time measurement.

Time is measured with an instrument called a clock. The spinning of the earth on its axis served as the earliest clock (3500 BC). It was the crudest form of time measurement. With the advancements, from one civilization to another, several other ways of measuring time were developed. Mechanical clocks came into use around 1285 AD. These clocks often installed in a building that acted as a focal point for the community (ie, church) had a 'verge' and a 'foliot' which were used for a mechanism that rang a bell. In the 14th century AD, large mechanical time indicators were installed in the bell towers, and were given the name *clock*, which originally means a *bell*. These clocks were not accurate and the development of industry from one civilization to another, demanded accurate clocks. By this time it was clear, that a clock is comprised of two components: an oscillator that produces the oscillations or *ticks* and a device to count the oscillations.

The most significant advance in the history of clocks was Huygen's pendulum clock in 1656, which was accurate to less than 1 minute a day. Later

refinements to his clock reduced the error to less than 10 seconds a day. The time period of a pendulum is defined by its length, l and the acceleration due to gravity, g.

$$T = 2\pi\sqrt{\frac{l}{g}} \tag{1.4}$$

Considering acceleration due to gravity, g to be a constant, the time period of a pendulum clock is defined only by the pendulum's length. Any temperature variations in the surroundings, lead to changes in the length of the pendulum and hence cause inaccuracies in the time measurement. George Graham increased the accuracy of the pendulum clocks to about one second a day by compensating for the changes in the pendulum's length due to temperature variations. Friction due to moisture and dust in the air also caused inaccuracies in the time measurement. John Harrison, a carpenter and a self-taught clock-maker, refined Graham's temperature compensation techniques and developed new methods for reducing friction. In 1761, he constructed a marine chronometer with a spring and balance wheel escapement that was used as a means of determining longitude to within one-half degree after a voyage to West Indies from England [8]. It was capable of keeping time with an accuracy of about one-fifth of a second a day onboard a moving ship, which was as good as a pendulum clock could do on land.

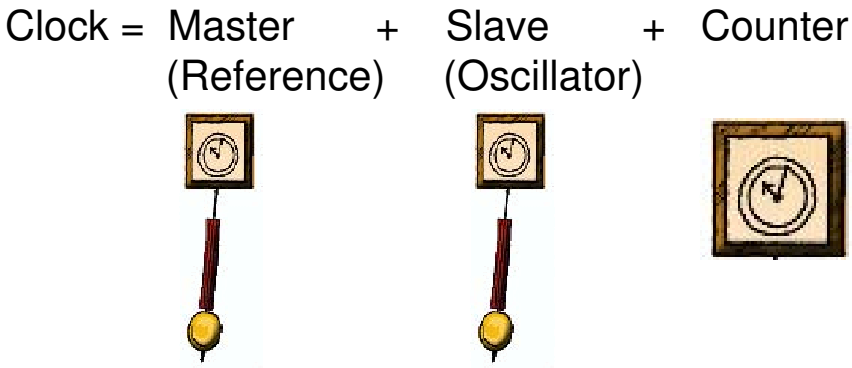

Figure 1.1: Components of a clock

In 1889, Siegmund Riefler developed a clock with a nearly free pendulum, which attained an accuracy of a hundredth of a second a day and became the standard clock in many astronomical observatories. Later in 1898, R.J.Rudd introduced a true free-pendulum principle, which led to the development of several free-pendulum clocks. The most significant one was developed by W.H.Shortt in 1921. It consisted of two pendulums: a slave and a master.

The slave pendulum drives the clock's hands and also keeps the master pendulum in motion, by pushing it gently when required. In this way, the master pendulum remained free from mechanical tasks that disturbed its regularity. Shortt's clock replaced Riefler's clock in several observatories. Shortt's clock provided a revolutionary concept which forms the basis of the present day clocks. It consists of an oscillator, a frequency reference and a counter.

In the 1930s, quartz crystal clocks were developed, which were accurate to about 1 minute a year. These accuracies were surpassed by microwave-transition based caesium-beam (atomic) clocks. Although the technology is very different, the basic concept is entirely analogous to Shortt's clock. The atomic reference serves as the master pendulum, the microwave oscillator (flywheel) performs the functions of the slave and an electronic counter is used to measure the frequency.

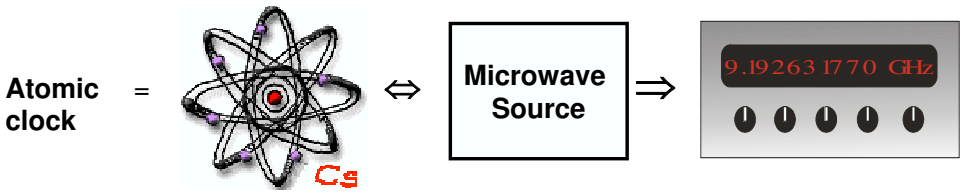

Figure 1.2: Components of an atomic clock

A caesium-beam atomic clock has an accuracy of about 2ns per day or 1 second in 1.4 million years. A modified version of the caesium beam clock is the caesium atomic fountain which has an accuracy of about 50ps a day or 1 second in 4.5 million years. These developments led to the redefinition of the second.

In 1967, the 13th General Assembly on Weights and Measures defined the International System (SI) unit of time (the second) in terms of atomic time rather than the motion of the earth. The second is now defined as *the duration of the 9,192,631,770 cycles of microwave radiation absorbed or emitted by the hyper-fine transitions of cesium-133 atoms in their ground state undisturbed by external fields.*

1.2 How an Atom defines Time

In order to understand how an atom defines time, it is necessary to consider the interaction of an atom with light in more detail.

An atom consists of a small nucleus, surrounded by a relatively large cloud of electrons. For our purposes typically, the electrons are arranged in

some stable configuration that corresponds to their lowest energy distribution or level called the *ground state*. According to the quantum-mechanical theory [9], an atom can exist with its electron cloud in only certain specific configurations corresponding to only certain values of energy. That is the electrons cannot have any random amount of energy, instead they exist in *discrete* energy levels. The idea of discrete energy levels rather than a continuous range of energies is known as *quantization*.

The *transition* between the two discrete atomic states is associated with the absorption or the emission of light of a specific frequency (Figure 1.3).

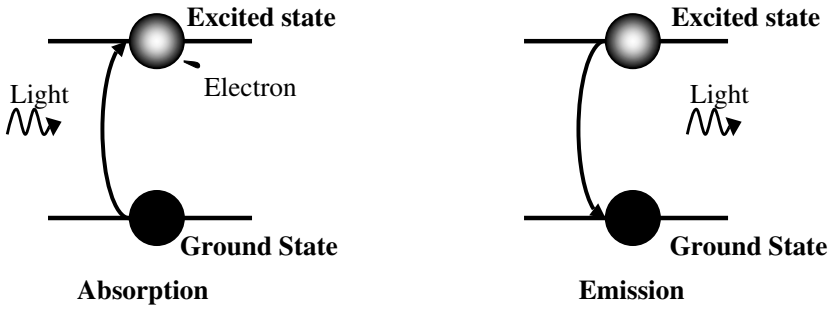

Figure 1.3: The absorption and emission of light from an atom

The amount of energy that incident light possesses is directly proportional to its frequency.

$$E = h\nu \tag{1.5}$$

where h is the Plank's constant and ν is the frequency of the incident light.

Although several quantum transitions are possible; atomic clocks utilize those that refer to a change in the electron and nuclear spin or *hyperfine energy levels*[5] of the ground state. The advantage of using such transitions is that the frequencies of these transitions occur in microwave region, where they can be counted electronically. In 1937, I.I.Rabi [10] and his associates [11] developed a method for accurately measuring the frequency of hyperfine transitions using atomic-beam resonance, which was crucial for the development of the Cs beam clock.

A caesium clock operates by exposing Cs-133 atoms to microwaves which are tuned to be in resonance with the transition frequency between two hy-

[5]Fundamental particles have *intrinsic angular momentum* called spin and different arrangements of the relative orientation of the spins of the particles that compare the atom led to subtly different energy levels called hyperfine energy levels.

perfine energy levels and then counting the corresponding cycles as a measure of time.

1.3 Some important parameters-Definitions

Stability

Stability is an inherent characteristic of an oscillator that determines how well it can produce the same frequency over a given time interval. It does not indicate whether the frequency is right *or* wrong*, but only whether it remains the same* [12]. It is specified by Allan deviation (refer to section 2.3.2).

Accuracy

Accuracy is the degree of conformity of a measured or a calculated value to its definition. It is related to offset from an ideal value [13].

Precision

Precision characterizes the degree of mutual agreement among a series of individual measurements, values, or results [14]. Mathematically, it is defined as the number of significant digits in a measurement.

Reproducibility

Reproducibility is a measure of repeatability of a measurement when performed by different experimentalists or laboratories using the same method [15].

1.4 Optical clocks

An atomic clock has three principal components: an oscillator, an atomic reference that controls the frequency of the oscillator and a counter. In a caesium atomic clock, the frequency of the microwave oscillator is *locked* to the frequency of the ground state hyperfine transition of the caesium atom and high-speed electronics are used to count the frequency of the reference oscillator. Similarly, for an optical clock, the frequency of the oscillator (an *ultrastable* laser) needs to be stabilized to the frequency of a narrow atomic transition of the chosen atom or the ion (in the visible region), and to be counted in some way. However, the problem with constructing such a clock is that optical frequencies are too high to be counted electronically. A lot of

research has been conducted in various parts of the world to overcome the problem of counting optical frequencies.

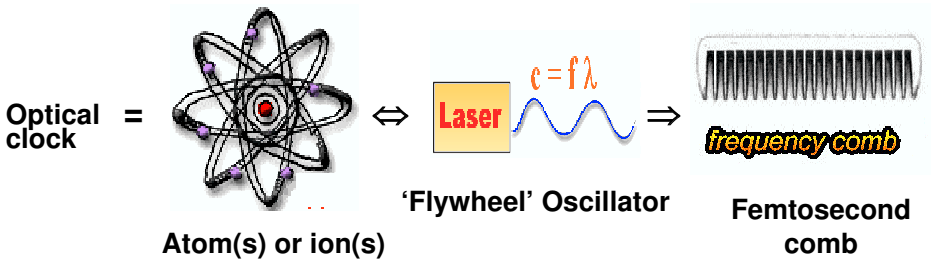

Figure 1.4: Components of an Optical Clock. A *Flywheel* oscillator has an extremely good short term stability but is prone to drift in the long term.

One way to measure optical frequencies is to use a harmonic frequency chain, which is based on frequency multiplication from the microwave to the optical domain. The frequency multiplication is performed with a nonlinear device, called a mixer. However, there is no mixer available, which is fast enough to do the microwave to optical conversion in just one step. Therefore, it is necessary to synthesize a chain of intermediate frequencies that lead to the optical frequency. Such a frequency chain involves a variety of nonlinear mixing elements and intermediate frequency sources, which makes the system very complex. Each stage in the chain uses different technology, which, makes it very expensive and difficult to construct and maintain. Also, each chain is specific to a particular frequency measurement and adapting it for a different optical frequency is not simple. A few phase-coherent harmonic frequency chains, have been constructed at NPL (UK), PTB (Germany) and NRC (Canada). However, these harmonic frequency-chains because of their complexity cannot be used as counters for the optical clock.

It was demonstrated in the late 1990s [16], that the spectrum of light emitted by mode-locked femtosecond laser could be used as a precise frequency *ruler*; as this gives rise to a series of regularly spaced frequency spikes called a *frequency comb*. The width of such a *frequency comb* can be broadened using non-linear optical effects (such as the Kerr effect). The output of such a device, when referenced to a radio-frequency source can be used to measure an optical frequency. Long-Sheng Ma et al. [17, 18] in their measurements using a frequency comb were able to relate two frequencies in the optical regime with an accuracy of about 1 part in 10^{19}. This result is quite remarkable and suggests that optical clocks are not very far from realization.

At present, the best microwave time standard based on transitions within

caesium atoms has an accuracy of about one part in 10^{15} in 1s, whereas the best optical frequency standards (spectroscopy of laser cooled single atoms and ions) are expected to approach a level of one part in 10^{18} in 1s [3]. With the development of optical frequency standards and femtosecond frequency synthesizers or frequency combs, it will be possible to construct a functional atomic clock with such an accuracy. Such a development will undoubtedly lead to new discoveries and advances in a wide range of fields of science and technology. For example, such highly accurate clocks can be used to measure fundamental constants with increased precision. These measurements may lead to the observation that the *fundamental constants* vary spatially or change with time and to the realization of the Grand Unification theory. On a more applied level, this new technology of optical frequency metrology will have applications in satellite navigation, communications and the synchronization of computer networks.

1.5 Ultrastable Cavities

As mentioned at the beginning of the chapter, a laser locked to a resonance of a Fabry-Perot cavity can be used as an oscillator in a number of applications. The resonance frequency, ν of a Fabry-Perot cavity is given by

$$\nu = \frac{nc}{2L} \tag{1.6}$$

where n is an integer, c is the speed of light and L is the length of the cavity. Hence, the frequency of a cavity-stabilized laser depends critically on the length of the cavity. Changes in the temperature, the optical power dissipated in the cavity and mechanical forces, all contribute to changes in the length of the cavity. To use a cavity for frequency stabilization, it is essential to keep its length constant. This is achieved by reducing the level of external disturbances and by making the cavity itself less sensitive to such disturbances.

A Fabry-Perot cavity consists of a spacer and two mirrors stuck on either end of the spacer. To have an extremely stable frequency reference, the mirrors are made from the same material (with extremely low thermal expansion coefficient) as the spacer and are optically contacted on either end. The most successful material to date, is ULE (ultra-low expansivity glass), which has a thermal expansion coefficient ($\sim 1 \times 10^{-8}\mathrm{K}^{-1}$) at room temperature. Lasers with sub-hertz linewidth have been constructed by locking their frequencies to a mode of such a cavity [20]. The long-term stability of such lasers is still an issue, due to the stress relaxation in ULE [22], which is amorphous

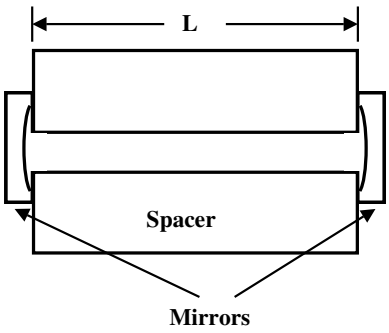

Figure 1.5: A Fabry-Perot (FP) cavity. L denotes the length of the cavity.

or microcrystalline. The drift related to ULE cavities has been extensively studied [22, 23, 24] and measured. Drifts of the order of few kHz per day have been reported [23]. To overcome the problem of the drift associated with ULE cavities, cryogenic monocrystalline silicon [25] and sapphire [26, 28, 29] cavities have been used as an alternative.

High-purity mono-crystalline sapphire, when held at liquid-He temperatures (4.2K), has an extremely low thermal expansion coefficient ($\sim 1 \times 10^{-8}\mathrm{K}^{-1}$ along its c-axis) and high thermal diffusivity [27] which favours it as a material for the spacer and mirrors for Fabry-Perot cavities. Schiller's group at Konstanz in Germany has reported frequency instability of 0.7 Hz for 20 s [27, 37] corresponding to 2.3×10^{-15} fractional instability, for a laser locked to a cryogenic sapphire cavity. These lasers are being used for performing tests of fundamental physics (Michelson-Morley experiment [30, 31], test for local position invariance [32, 33], tests of relativity [34, 35, 36] etc.).

The work presented in this thesis is on the stabilization of lasers to cryogenic sapphire and ULE cavities. At the outset the intention was to work exclusively with cryogenic sapphire cavities, however, various experimental delays and setbacks made it necessary for me to spend some of my time working on the alternative ULE based schemes.

1.6 Thesis Guide

The work discussed in this thesis involves frequency stabilization of NPRO type Nd:YAG lasers using cryogenic sapphire and ULE (ultra-low expansivity) glass. The theory of the frequency stabilization scheme (Pound-Drever-Hall) used in these experiments is discussed in chapter 2. Chapter 3 is a survey of the applications of such lasers. The experimental design and setup for both cryogenic sapphire and ULE glass cavities are discussed in chapter

4. Chapter 5 presents the results obtained in both the experiments. The final chapter summarizes the contributions of this thesis and discusses future work that has been or will be carried out to further improve the frequency stability of such lasers.

Chapter 2

Theory and Background

2.1 Introduction

The term laser is an acronym for *Light Amplification by Stimulated Emission of Radiation*. One of the main features of laser light is its monochromaticity. Laser light is certainly monochromatic as compared to other sources of light. However, frequency and intensity fluctuations in the laser light make the laser linewidth finite (i.e, a finite spread of frequencies or wavelengths). There has been a continuous effort in recent years to reduce both intensity and frequency fluctuations in lasers used as *flywheel* oscillators for atomic clocks [3, 4] and other experiments such as high resolution spectroscopy [4], precision tests of fundamental physics [32, 33],tests of relativity [34, 35, 36] and precision interferometry for gravitational wave detection [48].

This chapter contains the theory of the processes involved in producing laser light and a review of work which has been done in the past to reduce the noise associated with it. An account of the various schemes used for stabilizing the frequency of a laser is also given. Of these schemes, the Pound-Drever-Hall technique [45] is described in detail since it is the method of choice in all ultrastable laser systems [37, 38, 39].

2.2 Laser - basics

In its most basic form a laser cavity consists of a gain medium placed between two mirrors, as shown in figure 2.1 .

The operating frequency of a laser is determined by the optical path length L between the mirrors and the energy difference ΔE of the two energy levels between which the stimulated emission occurs. The two relations given

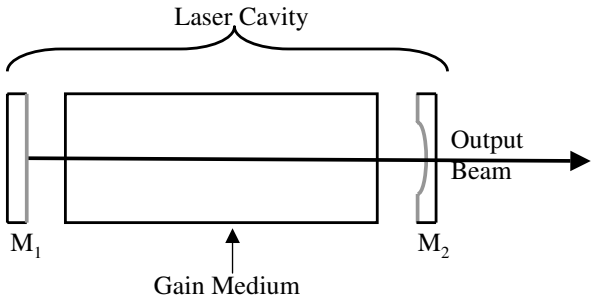

Figure 2.1: Laser cavity: M1 and M2 are mirrors that form the cavity along with the gain medium.

below must be simultaneously satisfied [40]:

$$\nu = \frac{mc}{2nL} \tag{2.1}$$

and

$$\nu = \frac{\Delta E}{h} \tag{2.2}$$

where m is an integer, c is the speed of light, h is Planck's constant and n is the refractive index of the gain medium between the cavity mirrors. Equation 2.1 gives the so called longitudinal mode frequencies of the longitudinal modes of the cavity and the integer m corresponds to the mode number.

A number of distinct processes can occur in the gain medium that are relevant to a laser's operation: absorption, stimulated emission, spontaneous emission and radiative de-excitation (figure 2.2). Absorption is the process in which the energy of a photon of particular frequency is absorbed by an atom such that the valence electrons of that atom make a transition between two electronic energy levels. When a photon of energy $h\nu$ is incident on an excited atom and its energy is equal to the energy gap between the excited and the ground state; the atom is de-excited and two photons of the same frequency as the incident photon are emitted. This process is termed *stimulated emission.* When an atom jumps from a higher level to a lower level without any external influence, the process is called *spontaneous emission.* At a more fundamental level, spontaneous emission results from the atom being perturbed by *vacuum fluctuations.* When an atom jumps from a higher to a lower energy level without emitting a photon, the process is termed *non-radiative de-excitation.* This can happen via collisional processes. Of these, stimulated emission is the dominant process in the case of lasers but spontaneous emission in the laser gain medium contributes to the line broadening of the laser output. Apart from spontaneous emission, there are other processes, for example,

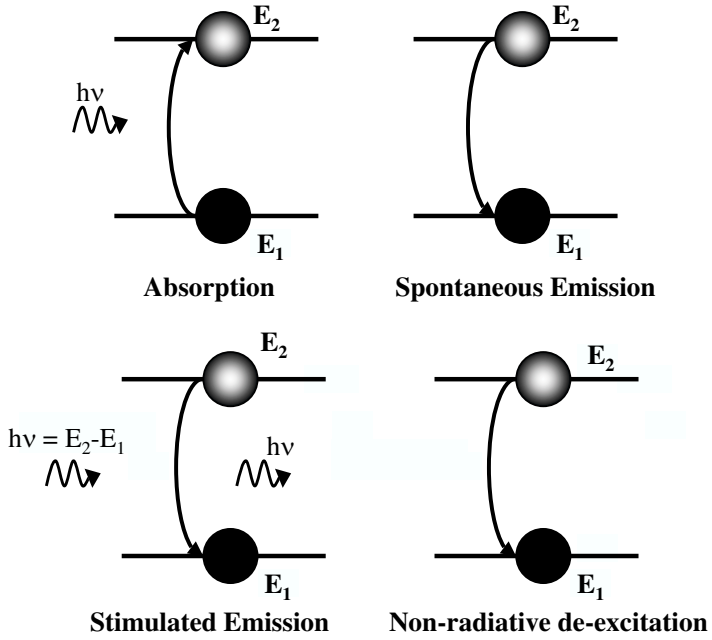

Figure 2.2: Processes involved in the laser medium: Absorption, Spontaneous emission, Stimulated Emission and Non-radiative de-excitation

collisions and atomic motion in gas lasers[41] and lattice vibrations [41] in diode lasers that contribute to line broadening of the laser output. There is thus a finite gain bandwidth, which is a measure of the range of frequencies, which satisfy equation 2.2. Thus equation 2.2 should be written as

$$\nu = \frac{\Delta E \pm \delta E/2}{h} \tag{2.3}$$

where δE is the total energy spread of the energy gap ΔE due to different processes that take place inside the laser gain medium. The gain due to stimulated emission reaches a maximum at a frequency corresponding to the average value of change in energy, ΔE.

Figure 2.3 shows the spread of frequencies due to equation 2.3 simultaneously with the frequencies allowed by equation 2.1. Laser gain reaches a maximum at the average value of the energy spread, $\langle \Delta E \rangle$. Usually, a laser cavity allows several longitudinal modes, each defined by a different m, to fall within the gain bandwidth. In some cases, such as gas lasers, several such modes can *lase* simultaneously. These modes have different frequencies and in general no coherence with respect to each other[1]. Interference between the

[1]A process called *mode locking* can be used to force the modes to be coherent. This process is important in frequency combs

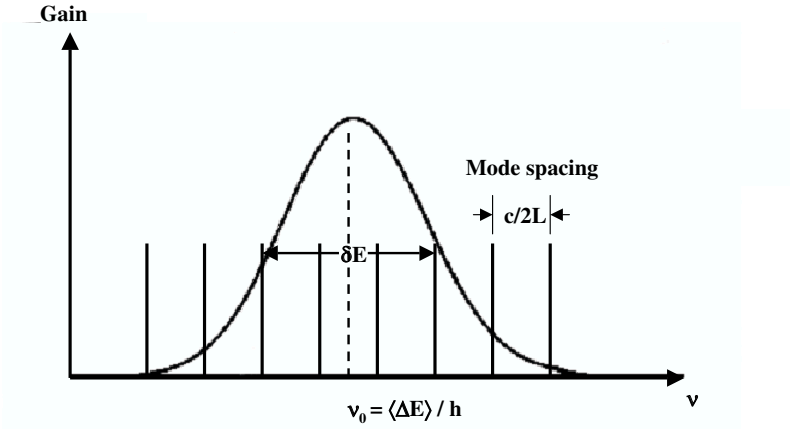

Figure 2.3: Laser gain profile showing the spread of frequencies due to equation 2.3 and the frequencies allowed by equation 2.1

modes leads to uncontrollable random behaviour in the output of the laser. Much of this undesirable behaviour can be avoided by forcing the laser to operate in a single longitudinal mode. There are a number of techniques by which single mode operation can be achieved. The most common is to insert a Fabry-Perot etalon into the laser cavity, which suppresses oscillation of all, but the desired mode. Several other ways of obtaining single mode operation can be found in any standard textbook on lasers [42].

According to equation 2.1, frequency noise in the laser output can arise from fluctuations in refractive index, n and the length of the cavity, L, both of which can be easily perturbed by environmental influences. The process of spontaneous emission, due to its random nature also gives rise to frequency fluctuations. This process is completely uncorrelated to the stimulated emission that occurs inside the laser medium. The noise generated by the spontaneous emission is fundamental in nature and gives rise to *phase noise* in the laser output [43]. Amplitude or intensity noise originates mainly from the pumping process because the phenomenon of gain saturation [41] quickly damps out any internally generated intensity fluctuations. However, there is a fundamental source of intensity noise due to the fact that light is composed of photons that have particle-like properties. This noise termed *photon shot noise* also gives rise to *phase noise* in the laser output, and is associated only with the detection of laser light.

The laser noise (frequency and amplitude) can, thus, be classified as: *fundamental* noise, that is inherent in the lasing process (or the *quantum phase noise*), and *technical* noise, which is mainly due to environmental perturbations. Several ways of reducing the technical noise have been developed,

which are discussed in section 2.6, but the fundamental noise imposes a lower limit to the stability that can be achieved for a free running laser and is discussed in section 2.4. This is the so called *Schawlow-Townes limit*. It is worth noting that if the laser is not free-running, but has had its frequency actively *locked* to an extremely stable frequency reference, then the spontaneous emission noise, can in principle [38] be reduced. This leaves *photon shot noise* as the fundamental limit to the stability of the system as a whole.

2.3 Measures of laser noise

There are three main measures of the laser noise [44], viz, power spectral density of fractional frequency fluctuations, Allan variance and linewidth. All the three parameters are related to each other mathematically however; they are used to quantify different aspects of the laser noise. Lasers are characterized by the power spectral density of the fractional frequency fluctuations in the frequency domain and by Allan variance in the time domain.

Sometimes the stability of a laser is described by the frequency fluctuation, $z(t)$

$$z(t) = \frac{\nu(t) - \nu_0}{\nu_0} \tag{2.4}$$

where ν(t) is the instantaneous frequency and ν_0 is the nominal (average) frequency of the laser.

2.3.1 Power spectral density

Power spectral density imposes a scale to the amplitude axis of frequency spectra of random signals such that meaningful comparisons between signals of different strengths can be made. It is used to characterize the short-term behavior of an oscillator and is measured using a radio-frequency spectrum analyzer. For a specified bandwidth of radiation consisting of a continuous frequency spectrum, *power spectral density is defined as the total power in the specified bandwidth divided by the bandwidth* [49].

If $y_i(t)$ is the i-th value[2] of a time series of N samples of $y(t)$ with sampling period Δt, then a parameter E proportional to the energy content of the

[2] $y_i(t)$ can be any quantity, for example frequency fluctuation, temperature fluctuation etc. In our case, $y_i(t)$ denotes a change in frequency (frequency fluctuation) at a particular time.

signal can be defined[3] as:

$$E = \sum_{i=1}^{N-1} \mid y_i(t) \mid^2 \Delta t \tag{2.5}$$

In a similar way, a parameter P proportional to the power defined as energy per unit time can be written as

$$P = \frac{E}{N\Delta t} = \frac{1}{N} \sum_{i=1}^{N-1} \mid y_i(t) \mid^2 \tag{2.6}$$

Hence, the power spectral density $S_y(f)$ [49] by its definition is given by

$$S_y(f) = \frac{1}{N} \sum_{i=1}^{N-1} \frac{\mid y_i(t) \mid^2}{B} \tag{2.7}$$

where B is the specified frequency bandwidth. In other words, the rms variation of a quantity $y(t)$ is given by its power spectral density:

$$\int_0^\infty < y^2(t) > dt = \int_0^\infty S_y(f) df \tag{2.8}$$

The power spectral density $S_y(f)$ of any quantity $y(t)$ has the dimension of [dimension of $y(t)]^2$/Hz. For frequency stabilized lasers, a measure of laser noise is obtained by the power spectral density of the frequency fluctuations which has a dimension of Hz^2/Hz. In some publications [38], square root of the spectral density of frequency fluctuations $\sqrt{S_y(f)}$ is referred to as the linear spectral density of frequency fluctuations denoted by S_f. The unit of linear spectral density S_f is thus Hz/$\sqrt{\text{Hz}}$.

It has been found experimentally that, for a remarkably wide range of systems, a power law can approximate the spectral densities of high stability frequency standards [52]. According to this approximation the spectral density of fractional frequency fluctuations is equal to the sum of terms, each of which varies as an *integer* power of the Fourier frequency f. The integer powers are restricted to $-2, -1, 0, 1, 2$ and each integer describes a different type of noise. Thus, there are two quantities that completely specify $S_y(f)$

[3]Electric power consumed by a load is proportional to the square of voltage across it and the kinetic energy of a moving mass is proportional to the square of its velocity. In the same way, the square of a random signal describes its *energy content* [49].

for a particular power-law process: the slope on a log-log plot, α for a given range of f and the amplitude h_α. Thus, $S_y(f)$ can be written as

$$S_y(f) = \sum_{\alpha=-2}^{2} h_\alpha f^\alpha \tag{2.9}$$

for $0 \leq f \leq f_h$, where f_h is an upper cut off frequency. The names given to different types of noise are shown in figure 2.4.

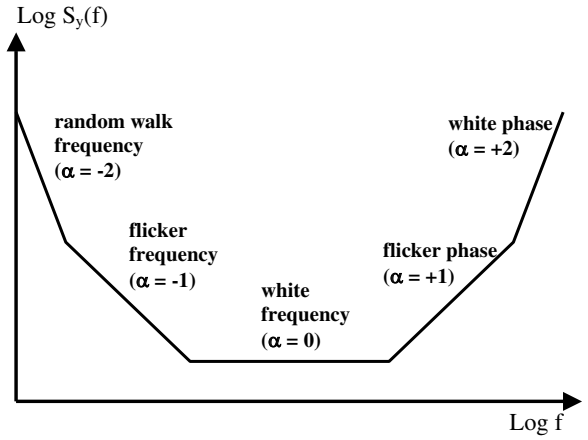

Figure 2.4: Power law for the Power spectral density of high-stability frequency standards [44]

2.3.2 Allan Variance

Allan variance is used to measure the fractional frequency stability of a frequency standard in a set time interval [50]. It can be measured using a frequency counter.

Let us consider an oscillating signal $V(t) = [V_0 + \epsilon(t)]\sin[2\pi\nu_0 t + \phi(t)]$ is applied to a frequency counter, where V_0 is the amplitude of the signal, with amplitude fluctuations $\epsilon(t)$, and ν_0 is the frequency of the oscillation with phase fluctuations $\phi(t)$. Considering $\epsilon(t)$ and $\frac{\partial\phi}{\partial t}$ to be small, fractional frequency fluctuations in the signal can be defined as

$$y(t) = \frac{\phi(t)}{2\pi\nu_0} \tag{2.10}$$

and the average fractional frequency fluctuation between time t_i and $t_i + \tau$, where τ is the measurement time is given by

$$\bar{y}_i = \frac{1}{2\pi\nu_0\tau}\int_{t_i}^{t_i+\tau} \phi(t)\partial t = \frac{\phi(t_i+\tau) - \phi(t_i)}{2\pi\nu_0\tau} \tag{2.11}$$

and Allan variance ${\sigma_y}^2(\tau)$ of the fractional frequency fluctuations defined as the infinite time average of $\bar{y}_i$ is

$$ {\sigma_y}^2(\tau) = \left\langle \frac{(\overline{y}_{i+1} - \overline{y}_i)^2}{2} \right\rangle \tag{2.12} $$

which can be estimated as [46]

$$ {\sigma_y}^2(\tau) = \frac{1}{m-1} \sum_{i=1}^{m-1} \frac{(\bar{y}_{i+1} - \bar{y}_i)^2}{2} \tag{2.13} $$

A power law, similar to that of the power spectral density, can approximate the Allan variance (figure 2.5)

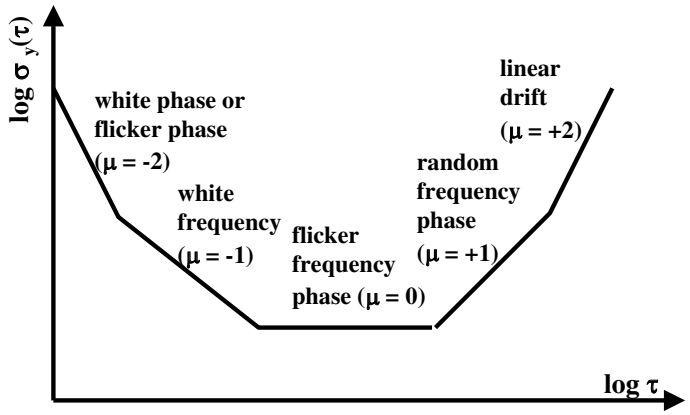

Figure 2.5: The Allan Variance [44]

$$ \sigma_y^2(\tau) = \tau^{\mu} \tag{2.14} $$

The main advantage of using the Allan variance over the power spectral density is that it can cope with linear drifts in the measurement, where as no tractable model exists for the power spectral density.

> If the measurement drifts as $y(t) = Dt$, then the root Allan variance, $s_y(\tau)(= \sqrt{{\sigma_y}^2(\tau)})$ is given by $D\tau/\sqrt{2}$ [46].

However, when the Allan variance of a time varying random signal is specified; it is not possible to distinguish between white phase noise ($\alpha = +2$) and flicker phase noise ($\alpha = +1$), as the slope is identical for both the cases. This limitation is overcome by the use of modified Allan variance, which is explained by Rutman and Allan [46, 47].

2.3.3 Allan variance and spectral density relation

If the spectral density of frequency fluctuations $S_y(f)$ is known, then the Allan variance can be expressed as [46] (refer to appendix A.1),

$$\sigma_y^2(\tau) = 2\int_0^\infty S_y(f)\frac{sin^4(\pi f\tau)}{(\pi f\tau)^2}df \tag{2.15}$$

However, in general it is not possible to convert back from Allan variance to spectral density, as some of the information is lost in the conversion process.

Allan [47] has shown that in the case of power law approximations, given by equation 2.9 and 2.14, the spectral density exponent, α and Allan variance exponent, μ are related by:

$$\begin{array}{ll} \mu = +2 & \alpha \text{ undefined} \\ \mu = -\alpha - 1 & -3 < \alpha \leq 1 \\ \mu = -2 & \alpha \geq 1 \end{array}$$

The Allan variance derived by Cutler [51] from equations 2.9 and 2.15 is thus given by:

$$\sigma_y^2(\tau) = h_{-2}\frac{(2\pi)^2\tau}{6} + h_{-1}2\ln 2 + \frac{h_0}{2\tau} + h_1\frac{1.038 + 3\ln(2\pi f_h\tau)}{(2\pi)^2\tau^2} + h_2\frac{3f_h}{(2\pi)^2\tau^2} \tag{2.16}$$

The value for each coefficient h_α can be obtained using standard regression techniques and is used to calculate the Allan variance. This result is summarized in table 2.1.

Type of noise	α	$S_y(f)$	$\sigma_y^2(\tau)$
Frequency random walk	-2	$h_{-2}f^{-2}$	$6.58h_{-2}$
Frequency *flicker*	-1	$h_{-1}f^{-1}$	$1.39h_{-1}$
White frequency	0	h_0	$1.39h_0/\tau$
Phase *flicker*	$+1$	h_1f^1	$0.02h_1/\tau^2 + 0.165h_1f_h/\tau$
White phase	$+2$	h_2f^2	$0.76h_2f_h/\tau^2$

Table 2.1: Relationship between Allan variance and spectral density [57]

2.3.4 Linewidth

Linewidth is defined as FWHM (Fullwidth at half maximum) of the power spectral density function of frequency fluctuations in the laser output. It is a measure of coherence[4] in the laser output [54, 55]. The coherence of a laser beam is defined by its auto-correlation function given by equation 2.19 [56]. This can be made more clear by invoking the Weiner-Khintchine theorem, according to which, the power spectrum of a signal is the Fourier transform of its auto-correlation function measured in the time domain and vice versa (equation 2.17 and 2.18) [49]:

$$S_y(f) = \int_{-\infty}^{\infty} R_y(\tau) exp(-j\omega\tau).d\tau \tag{2.17}$$

and

$$R_y(\tau) = \int_{-\infty}^{\infty} S_y(f) exp(-j\omega\tau).df \tag{2.18}$$

where $R_y(\tau)$ is the auto-correlation function.

$$R_y(\tau) = \lim T \rightarrow \infty \frac{1}{T} \int_0^T y(t)y(t+\tau)d\tau \tag{2.19}$$

Replacing, the auto-correlation function $R_y(\tau)$ given by equation 2.19 in equation 2.17 gives the power spectral density of frequency fluctuations $S_y(f)$ and linewidth is measured from the power spectral density function. Thus, linewidth gives a measure of coherence in the laser output.

2.3.5 Spectral density and linewidth relation

The spectral density of fluctuations in a laser's frequency can be related to its linewidth, in the following way [58]:

> *For a laser with a white noise linear spectral density of frequency fluctuations, S_ν specified for a bandwidth B and no other noise outside the specified bandwidth, if the rms fluctuations in frequency of the laser, $d\nu_{rms} \ll B$, then the laser lineshape is Lorentzian and the linewidth is equal to*

$$\Delta\nu_L = \frac{\pi(\delta\nu_{rms})^2}{B} = \pi S_\nu^2 \tag{2.20}$$

[4] If the phase of two electromagnetic waves maintain a constant relationship at any two instants in time then waves are said to be coherent. Coherence is defined by the cross-correlation function of the two waves.

However, if the rms fluctuations $d\nu_{rms} \gg B$, then the lineshape is Gaussian and the linewidth is equal to

$$\Delta\nu_L = 2.35\delta\nu_{rms} = 2.35S_\nu\sqrt{B} \tag{2.21}$$

In practice, the spectral density of frequency fluctuations shows a flicker frequency noise at low frequencies and the above formula cannot be used. In that case, the only way of getting an estimate of linewidth from the spectral density is by calculating the FWHM (Fullwidth at half maximum) of the function obtained by solving equation 2.17 and 2.19.

2.4 Fundamental limitations to the stability of a free running laser

As mentioned in the section 2.2, there are two main sources of the fundamental noise that limit the stability of a free-running laser: the spontaneous emission in the gain medium and the *photon shot noise*.

2.4.1 Spontaneous emission noise: Schawlow-Townes linewidth

There are two processes by which the atoms in the laser gain medium radiate light at the laser wavelength: stimulated emission and spontaneous emission. Of the two, stimulated emission is the dominant mechanism, whereby, an incident photon stimulates an atom in the excited state to emit a second photon at the same frequency as the incident photon. Hence, the two photons that are emitted are in phase with each other. However, there are always some spontaneously-emitted photons that have random phase compared to the other photons (emitted by stimulated emission). Spontaneously-emitted photons thus produce a random phase change in the phase of the total output light of a laser. Successive spontaneous emission events make the phase of the total output field diffuse in a manner analogous to a particle undergoing Brownian motion, hence this effect is called *phase diffusion* and the type of noise is the *phase noise*.

The instantaneous frequency of the laser light is the time derivative of the phase.

$$\nu(t) = \frac{\omega}{2\pi} = \frac{1}{2\pi}\frac{d\phi}{dt} \tag{2.22}$$

where ϕ denotes the phase of the laser output and ν is its frequency. Thus, a small change in the phase also produces a small frequency deviation. For

a standard free-running laser, the spontaneously emitted radiation has an inherent, Lorentzian distribution of frequencies [42], and the linear spectral density of frequency fluctuations [41, 38] is given by

$$S_{f,ST} = \delta\nu_L \sqrt{\frac{2h\nu}{P}} \tag{2.23}$$

where P is the laser power and $\delta\nu_L$ is the intrinsic linewidth of the laser defined as

$$\delta\nu_L = \frac{c(1-R)}{2\pi L} \tag{2.24}$$

where c is the speed of light, R is the reflectivity of the mirrors and L is the length of the cavity. An oscillator with a white noise linear spectral density of frequency noise S_f has a linewidth $\Delta\nu = \pi S_f^2$ (refer to section 2.3.5). Thus, $\Delta\nu$ is given by

$$\Delta\nu_{L,ST} = \frac{2\pi h\nu\delta\nu_L^2}{P} = \frac{h\nu}{2\pi}c^2\frac{(1-R)^2}{PL^2} \tag{2.25}$$

where, $h\nu$ is the average photon energy and the $\delta\nu_L$ is the laser cavity linewidth. Spontaneous emission therefore sets a fundamental lower limit on the laser linewidth. This limit is termed *Schawlow-Townes linewidth*. It can be as low as 1Hz for output powers of 1mW in a diode pumped Nd:YAG laser because of the low crystal loss and resultant very narrow laser cavity linewidth, $\delta\nu_L$. However, the measured linewidth of a typical Nd:YAG laser is around $<$ 5kHz in 1msec. This is due to amplitude fluctuations in the pump laser that disturb the optical path length of the system as a whole [38]. These frequency fluctuations can be detected and suppressed using the *active* frequency stabilization described in section 2.6.2.

When the frequency of a laser is stabilized to a highly stable reference, then the achievable laser stability depends on how well the fluctuations in the laser's frequency are detected and removed. In this case, the fundamental limit to the achievable laser stability is the noise inherent in the detection process over the bandwidth of the control loop and is given by the photon shot noise discussed in the next section.

2.5 Photon Shot noise

Photon shot noise is due to the quantum-mechanical nature of the light. According to quantum theory, the energy of a light beam is delivered in discrete quanta (or photons). Thus, when a light beam is incident on a photodetector, there is a certain randomness associated with the arrival of the photons and therefore in the generation and flow of mobile charge carriers

that produce the output current. It has been proven that for a standard free running laser, the arrival of photons follows Poisson statistics [41]. Thus, the probability $P_n(T)$ of counting n photons in a fixed time interval T is given by

$$P_n(T) = \frac{\bar{n}}{n!} e^{-\bar{n}} \tag{2.26}$$

where $\bar{n}$ is the average number of photons counted in time T and the root-mean-square (rms) deviation $\Delta n(T)_{rms}$ of number of photons $n(T)$ from its average $\bar{n}$ is

$$\Delta n(T)_{rms} = \sqrt{\bar{n}} \tag{2.27}$$

Consequently, the randomness in the generation and flow of charge carriers that produce the output current also follow Poisson statistics. The spectral density function of fluctuations in the current measured at the photo-detector in the frequency interval ν and $\nu + \Delta\nu$ is given by [41]

$$\bar{i^2}_n(\nu) = S_n(\nu)\Delta\nu = 2e\bar{I}\Delta\nu \tag{2.28}$$

where $\bar{I}$ is the average current measured at the photo-detector in the frequency interval ν and $\nu + \Delta\nu$ and e is the charge of the particle responsible for current flow. It is interesting to note that if the charge of the particle responsible for the current flow, e tends to zero then the shot noise would disappear. This is a reflection of the fact that shot noise is due to the discreteness of the charge carriers and the random electron emission. Equation 2.28 can be re-written in terms of laser power as

$$\bar{i^2}_n(\nu) = S_n(\nu)\Delta\nu = \frac{2e^2 P\eta}{h\nu}\Delta\nu \tag{2.29}$$

where P is the average power incident on the photodetector in the frequency interval ν and $\nu+\Delta\nu$, $h\nu$ is the incident photon energy and η is the detection efficiency of the photodetector.

For a frequency-stabilized laser, the photon shot noise limit is determined by the type of mechanism that is used for the detection of frequency fluctuations.

2.6 Frequency stabilization of lasers

In order to reduce the noise of lasers, many *passive* and *active* stabilization techniques have been developed. Passive stabilization techniques involve designing the laser for rigidity, thermal stability and reducing the intrinsic linewidth $\delta\nu_L$ of the laser (equation 2.24) by judicious choice of parameters

(such as, cavity length and reflectivity of the mirrors). When the improvement accrued from passive stabilization have been exhausted it is still possible to reduce the laser noise further by employing *active* stabilization techniques. These involve detection of frequency fluctuations in the laser output and correcting for these fluctuations using a feedback loop. In this section, both the passive and active stabilization techniques used for the frequency stabilization of lasers are discussed.

2.6.1 Passive Stabilization

According to equation 2.25, the Schawlow-Townes linewidth of a laser can be dramatically reduced, by increasing the cavity length, L and reflectivity of the mirrors, R. In case of a diode laser, one of the simplest ways to achieve this is to insert the diode in an external cavity with highly reflecting mirrors. Since, the output beam of a diode is very divergent, one needs a collimating lens to keep the size and radii of curvature of the external cavity mirrors reasonable.

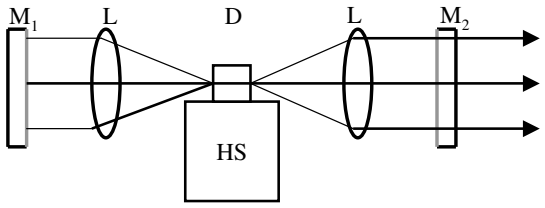

Figure 2.6: Passive stabilization of a diode laser D by placing it in an external cavity formed by mirrors M_1 and M_2. L denote the collimating lenses and HS is the heatsink on which the diode is mounted [40]

With careful mechanical design of such a laser some three orders of magnitude of linewidth narrowing, from 15MHz to 30kHz, can be achieved [61]. There are several other schemes [59, 60] besides the one mentioned above for stabilizing diode lasers with optical feedback. The most intensively used passively stable diode lasers are Extended Cavity Diode Lasers (ECDL) which are used to achieve narrow linewidths necessary for atomic spectroscopy experiments. This is achieved by coupling laser light to an extended cavity, which incorporates a diffraction grating as a wavelength-selective element. The extended cavity provides optical feedback to the laser, reduces the threshold current, narrows the linewidth and provides broad tunability. Two common optical configurations used are: the *Littrow* and *Littman* configurations.

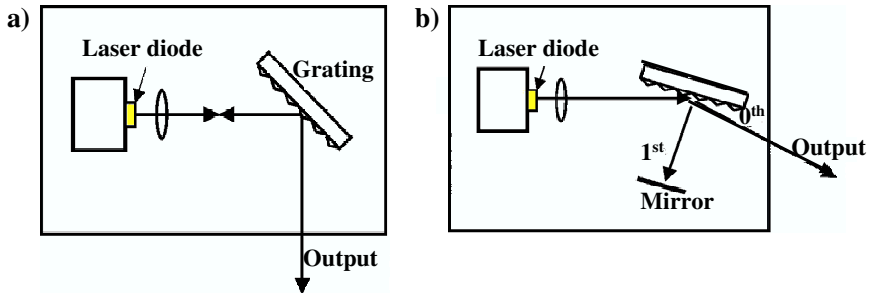

Figure 2.7: a) Littrow configuration for passive frequency stabilization of a diode laser. The wavelength of the laser is tuned by changing the angle of the grating and 0^{th} order beam is the output. b) Littman configuration for passive frequency stabilization of a diode laser. The wavelength of the laser is tuned by rotating the mirror and 0^{th} order beam is the output.

In the *Littrow* configuration [66, 64](figure 2.7a), the grating is aligned so that the first order diffracted beam goes back directly into the laser. The lasing wavelength is then determined by the angle of the grating with respect to the laser; and is tuned by changing this angle. The zeroth order reflected beam is the output. This configuration offers the advantage that almost all of the laser light (up to 80 percent of the chip output) is available for the experiment. A disadvantage of using the Littrow configuration is that the output beam angle changes slightly as the laser is tuned.

In the *Littman* configuration [63, 62](figure 2.7b), the grating is kept fixed at an angle of incidence near 90 degrees, and the wavelength is tuned by rotating a special tuning mirror. The tuning mirror changes the wavelength for which the laser sees optical feedback. The zeroth order reflected beam off the grating is again used as the output. Since the grating in this configuration does not move, the output beam angle does not change as the laser is tuned. However, the disadvantage is that the zero-order reflection of the beam reflected by the tuning mirror is lost, hence, the output power is somewhat lower than for a *Littrow* laser [65].

Passive stabilization explained above has led to dramatic reduction in free-running laser linewidths. The most significant achievement is in case of the NPRO (non planar ring oscillator) type Nd:YAG lasers, whereby, free running linewidths of the order of $\sim 3-10$ kHz in 1msec have been realized, corresponding to a free running stability of $\sim 10^{-12}$ [68]. However, lasers used for frequency metrology purposes and other experiments, such as, gravitational wave detection, high-resolution spectroscopy, etc. require much higher frequency stability ($\sim 10^{-15}$ or less) than that achieved by passive stabilization of lasers. The passively stable laser used in most of these exper-

iments is a diode pumped NPRO (non planar ring oscillator) type Nd:YAG laser. The primary reason of using NPRO is that it is the most stable, commercially available laser. The free running spectral noise density of NPRO type Nd:YAG laser is of the order of 1kHz/$\sqrt{}$Hz at 10Hz and falls as $1/f$ at high frequencies [69]. Hence, both passive and active frequency control is necessary to satisfy the requirements. Active frequency stabilization of lasers is explained in detail in the next section.

2.6.2 Active electronic stabilization

As described by Day in his thesis [69], laser frequency stabilization can be considered as a problem in control theory. Figure 2.8 shows the schematic of a laser frequency stabilization control loop.

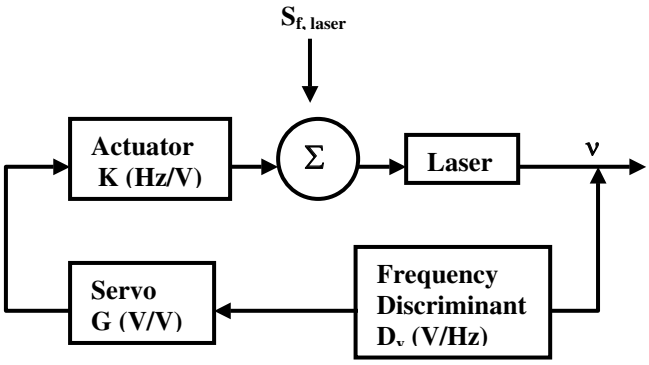

Figure 2.8: Laser frequency stabilization as problem in control theory [69]

In figure 2.8, the *laser* whose frequency is to be controlled is modelled as a plant that produces a fixed frequency ν and is perturbed by some noise process ($S_{f,laser}$). $S_{f,laser}$ denotes the linear spectral density of rms frequency fluctuations in the laser frequency in 1Hz bandwidth and has units Hz/$\sqrt{}$Hz. The instantaneous frequency of the laser is monitored with a *discriminator* that converts the optical frequency fluctuations into voltage fluctuations with a conversion gain D_v and produces an *error signal*[5]. This error signal is amplified in the *servo* that has a dimensionless frequency dependent gain coefficient $G(\omega)$. The output of the servo is then fed back negatively to the *actuator*, which converts the voltage fluctuations back to the frequency fluctuations with a conversion gain K(Hz/V). In this way, frequency fluctuations in the laser output are monitored and suppressed actively. A brief description of each element of the control loop, with reference to our experiment is given below.

[5]a measure of frequency-fluctuations in the laser's output

2.7 Elements of a laser frequency control loop

2.7.1 Laser

The laser whose frequency has to be stabilized in our experiment is a 1064nm, diode-pumped NPRO (non-planar ring oscillator) type Nd:YAG laser manufactured by Innolight, Model No. Mephisto 1200 NE. As described in section 2.6.1, the main reason for using this laser system is the fact that it is the most stable commercially available system. This laser system is chosen to demonstrate that very high stabilities can be achieved in such experiments. However, in case of designing an optical atomic clock, a tunable laser will be required, such that an arbitrary atomic reference can be reached. The free running stability of the Mephisto 1200 NE, as measured by tracking its lineprofile on a spectrum analyzer, is $\sim$ 1kHz in 100 milliseconds [71], corresponding to a dimensionless frequency stability of the order of $\sim 10^{-12}$ in 100ms.

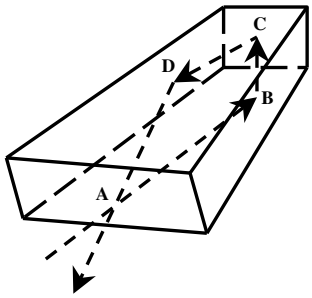

Figure 2.9: Nd:YAG laser crystal

Figure 2.9 shows the shape of the Nd:YAG laser crystal. The non-planar ring oscillator (NPRO) is a monolithic Nd:YAG laser crystal in which the non-planar ring laser path is formed by three total internal reflections and one dielectric mirror. It was invented by Kane and Byer [67] in 1985. Diode pumping, monolithic construction and non-planar geometry of the Nd:YAG crystal account for the high free running stability of a diode pumped NPRO laser. Diode laser pumping avoids the noise associated with flashlamps, monolithic construction provides efficient temperature control of the laser and the non-planar geometry of the crystal provides feedback isolation that eliminates spatial hole burning[6] and therefore forces single mode operation [70].

[6]a spatially dependent distortion of the gain profile in a laser medium caused by saturation effects of a standing wave is called *spatial hole burning*. This effect can make it difficult to achieve single frequency operation in lasers, because the lasing mode experi-

This non-planar geometry causes a slight rotation of the polarization direction in each round-trip. Furthermore, if a small magnet is attached to the laser crystal, its magnetic field can cause an additional polarization rotation via the Faraday effect. For one of the two oscillation directions, the two polarization rotations partly cancel, leading to a lower optical loss when the beam hits the output coupler face of the crystal (because the coating has a slightly polarization-dependent reflectivity). The other oscillation direction leads to a higher loss and is thus firmly suppressed. In this way it is possible to obtain unidirectional operation and hence avoid any standing-wave patterns (except very near to the reflection points), which would cause spatial hole burning. It is therefore possible to obtain stable single-frequency operation with non-planar ring oscillators. Since the round-trip length in case of NPRO type laser is rather short (typically around few centimeters), the NPRO cavity has a relatively large free spectral range. Hence it is possible to achieve continuous (mode-hope free) frequency tuning over several GHz [135].

The frequency of a diode laser changes with temperature and hence the temperature of such a laser needs to be stabilized. Likewise, the frequency of a NPRO depends on the temperature of the crystal. Hence, the temperatures of both the diode laser and Nd:YAG crystal inside the Mephisto are stabilized using two independent temperature controllers. The temperature controller used for stabilizing the Nd:YAG crystal has typical drifts of 100μK/min, corresponding to a variation in laser frequency of $<$ 1MHz/min [72].

2.7.2 Frequency Discriminator

The preliminary requirement for active stabilization of a laser system is the generation of an error signal, which is a measure of frequency fluctuations in the laser's output. The *frequency discriminator* performs the function of generating this error signal. It responds to optical frequency fluctuations of the laser and provides an output voltage linearly proportional to them. The most common method of obtaining an error signal is to compare the laser's frequency with a frequency reference. The discriminator provides the frequency reference to which the laser's frequency is compared. The difference between the two frequencies is the error signal.

Many different types of frequency reference have been used for active stabilization of lasers. These frequency references can be divided into two categories: *intrinsic* references (such as the peak of the laser transition, Lamb

ences stronger gain saturation that the competing non-lasing modes [79]. This leads to *mode-hopping* in which the laser makes sudden jumps between different lasing modes in response to the maximum available gain.

dip[7] in gas lasers) and *extrinsic* references (such as an atomic or a molecular spectral line or the resonance of a stable Fabry-Perot interferometer). The widths of intrinsic frequency references of a laser are of the order of few hundreds of kHz or more and therefore, the slope of the frequency discriminant obtained by using an intrinsic reference is not high enough to provide a good reference frequency. However, a few experiments were performed in the 1960's where the Lamb dip was used as a frequency reference for stabilizing a gas laser and stabilities of the order of $\sim 10^{-10}$ [80] were obtained, limited mainly by vibrations. After a few years, it was realized that an extrinsic reference such as an *atomic* or *molecular spectral line* or *resonance frequency of a high finesse Fabry-Perot interferometer* can provide a sharp frequency reference and hence a better stability. There are several candidates that can be used as extrinsic references for frequency stabilization of lasers. Table 2.2 compiles a list of all the available types of extrinsic frequency references.

Categories	Types	Materials
Interferometers	Fabry Perot Waveguide Resonators	Air, Quartz, ULE (Ultra low expansivity glass), Sapphire
Atomic transitions	Normal Absorption	Rb, Cs, Na, K, Ba, Bi, etc.
	Optogalvanic effect (absorption in discharge)	Ar I, Kr I, Ne I, Xe I, etc.
Molecular transitions	Diatomic molecules	I_2, Cs_2, Na_2, K_2, Rb_2, O_2, HF, HI, etc.
	Polyatomic molecules	H_2O, NH_3, HCN, C_2H_2, CH_4, H_2CO, SF_6, OsO_4, etc.

Table 2.2: Types of extrinsic frequency reference

The advantage of using an atomic or a molecular spectral line as a frequency reference is that most of these transitions are narrower than the intrinsic and are reproducible. However, the Bandwidth theorem dictates that narrow transitions must be weak and are therefore difficult to detect. This problem can be overcome by using a resonance of a Fabry-Perot cavity as a frequency reference. Extremely narrow resonances can be obtained by

[7] In an inhomogeneously broadened gas laser, the interaction between the two counter-propagating beams inside the laser cavity and the random thermal motion of the gas molecules lead to a reduction of the output power as the laser frequency is scanned through the peak of the gain curve. This is called the Lamb dip.

making the mirrors of the cavity highly reflective. The best cavities are made by optically contacting mirrors onto a spacer. The resonance frequency ν of a Fabry-Perot cavity is given by

$$\nu = \frac{mc}{2L} \tag{2.30}$$

where m is an integer, c is the speed of light and L is the length of the cavity. Considering the speed of light c to be a constant, the resonances of a Fabry-Perot cavity are defined by its length. For a cavity of length, $L = 10$cm even a small change in the length of the cavity $\delta l = 1\mu$m would change the resonance frequency by ~ 15kHz. It is therefore virtually impossible to build a cavity with a prescribed set of resonant frequencies. Hence, these resonances are extremely difficult to reproduce. This lack of reproducibility accounts for the fact that lasers stabilized to such cavities can only be used as *flywheel* oscillators and not primary sources. Moreover, the length of the cavity is perturbed by ambient fluctuations (such as, temperature, pressure, vibrations, etc.), which lead to fluctuations in resonance frequencies. In all the frequency stabilization experiments the difference frequency between the frequency of the source and the reference is controlled, which results in relative stabilization of the source frequency. In order to get high frequency stability with a Fabry-Perot cavity, the ambient fluctuations of the environment (such as, pressure, temperature and vibrations) need to be controlled and minimized.

As explained by Day [69] in his thesis, the properties of the frequency discriminant determine the overall performance of the system. The frequency discriminator is, therefore, considered to be a critical element of the control loop. This can be made more clear, by considering the block diagram shown in Figure 2.10,where each element in the loop is modeled to have a noise component associated with it that adds to the noise output and degrades the system performance. $S_{f,laser}$ is composed of two terms, the noise inherent to the laser and the actuator noise, which is indistinguishable from the laser noise. $S_{v,disc.}$ and $S_{v,servo}$ are the spectral densities of voltage noise associated with the frequency discriminator and servo, respectively. The total closed loop linear spectral density of frequency noise [69] is thus, given by

$$S_{f,cl} = \frac{\sqrt{S_{f,laser}^2 + |KS_{v,servo}|^2 + |KGS_{v,disc}|^2}}{|1 + KGD_v|} \tag{2.31}$$

When the gain of the loop is high, the discriminator noise contribution dominates all the other terms and the minimum closed loop spectral density of frequency noise [69] is

$$S_{f,clmin} = \frac{S_{v,disc}}{D_v} \tag{2.32}$$

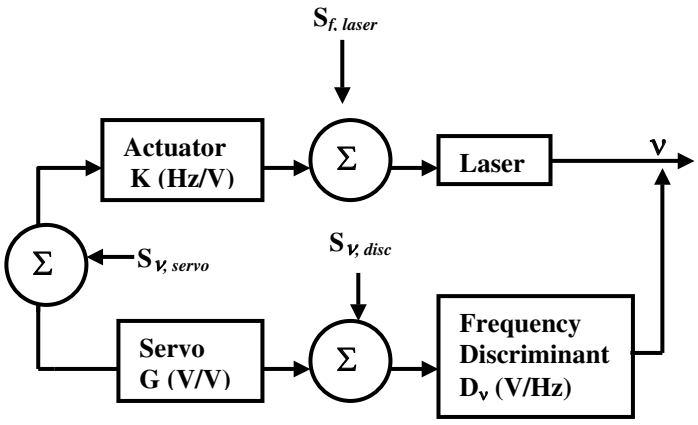

Figure 2.10: Laser frequency control block diagram with excess noise contributions from individual control elements [69]

Equation 2.32 shows that the minimum spectral density of frequency noise associated with a frequency stabilized laser depends on the slope of the discriminator D_v and its noise contribution $S_{v,disc}$. The discriminator noise comprises the technical noise associated with the discrimination technique (such as, the fluctuations in the frequency reference, $1/f$ noise in the discriminant amplifiers, etc.) and the quantum noise associated with the detection of the laser frequency or the *photon shot noise*. For a carefully designed frequency controller the contribution of the technical noise can be made negligible and the fundamental limit to the laser's noise is set by the photon shot noise. The overall performance limit of the system is then determined by the slope of the discriminator and the photon shot noise associated with the detector. The discriminator thus forms a critical element of the frequency control loop.

The frequency discriminator employed for the experiments described in this thesis are high-finesse Fabry-Perot cavities made of either cryogenic-sapphire or Ultra-low-expansivity glass. One of the resonances of these Fabry-Perot cavities is used as the frequency reference. The instantaneous frequency of the laser is compared to the resonance of the Fabry-Perot cavity and an error signal proportional to the difference is generated. This error signal contains the following information: to which side and how far is the laser's frequency from the frequency reference. Several frequency discrimination techniques have been used in past years to obtain the desired error signal (namely, side-of-fringe locking [74, 75, 76], Hänsch and Couillaud locking [73], Pound-Drever-Hall locking [45], etc.). One of the most common techniques used for obtaining an error signal is the side-of-fringe locking technique.

In the side-of-fringe locking scheme, the frequency of a laser is locked

to a half power point of transmitted intensity obtained from a Fabry-Perot cavity. At the half-power point, the transmitted intensity is linearly proportional to the changes in the laser frequency and the discriminator slope is maximum. The discriminator slope can be further increased by increasing the finesse[8]. This however increases the time delay associated with the transmission through the cavity and frequency fluctuations faster than the cavity response time (i.e., inverse of cavity linewidth, $\delta\nu_c$) are hugely attenuated with a time delay in the frequency control loop [75]. Furthermore, at low frequencies the amplitude fluctuations in the laser light are interpreted as frequency fluctuations by the system. These amplitude fluctuations thus need to be suppressed. A locking scheme that overcomes both of these problems is the Pound-Drever-Hall (PDH) locking scheme. This scheme has been used to stabilize the Nd:YAG lasers in our experiment and is described in detail in the next section.

2.7.3 Frequency Discrimination Technique: PDH locking

In the PDH locking scheme, a laser's frequency is measured in reflection from a high-finesse Fabry-Perot cavity and is locked to a resonance (or the zero intensity point) [77]. Figure 2.11 shows the reflected signal from a Fabry-Perot cavity near resonance.

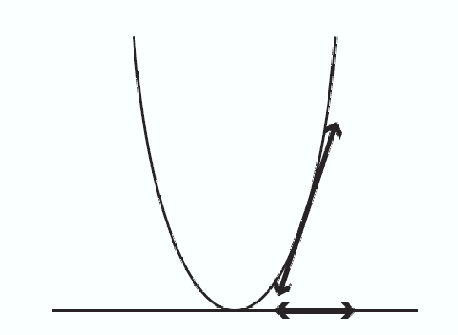

Figure 2.11: Reflected light intensity from a Fabry-Perot cavity as a function of laser frequency near resonance. If the laser frequency is modulated, it is possible to tell which side of the resonance is the laser's frequency by looking at changes in the reflected power [77]

[8]Finesse of a Fabry-Perot cavity is defined as the ratio of free spectral range of the cavity to its linewidth. It is given by the following equation $\mathcal{F} = \nu_{fsr}/\delta\nu$, where ν_{fsr} is the cavity free spectral range and $\delta\nu$ is its linewidth

It is clear from the above figure 2.11 that the intensity of the reflected beam is symmetric about resonance and does not contain enough information to be used as an error signal. It can only tell how far the laser's frequency is from the reference but not to which side. However, the derivative of the reflected intensity is asymmetric about resonance and therefore also contains information about which side of the resonance the laser frequency is. Hence, the derivative of the reflected intensity can be used as an error signal. PDH locking scheme is used to measure the derivative of the reflected intensity [77]. Figure 2.12 shows the block diagram of the Pound Drever Hall frequency stabilization scheme.

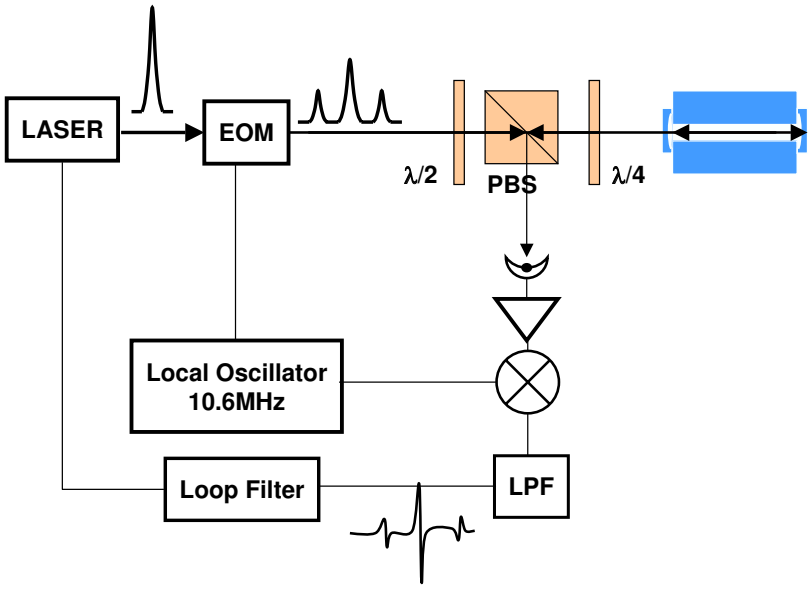

Figure 2.12: Block diagram of PDH locking scheme. EOM is the electro-optic modulator, PBS is the polarizing beam splitter and LPF is a low pass filter. The optical signals are denoted arrows where as electrical signals are denoted by thin lines.

In this method, the laser's output is mode matched to a high finesse Fabry-Perot cavity and is phase modulated using an EOM at an RF frequency, Ω greater than the cavity linewidth ($\Omega \gg \delta\nu_c$). The phase modulation sidebands never enter the cavity and are therefore reflected from the cavity with no relative phase shift. However, near resonance, the carrier experiences a strongly dispersive phase shift [43, 77, 69].

A very good explanation of this fact on the basis of reflection of a monochromatic beam from a Fabry-Perot cavity is given by Black [77]. The beat frequency between the phase shifted carrier and its sidebands is mea-

sured on a high frequency photodetector. The output of the photodiode contains an amplitude modulated term at the modulation frequency Ω with an amplitude proportional to the sine of the round trip phase shift (θ) [69]. Near resonance, this term is directly proportional to the frequency offset $\sin\theta \sim \theta = 2\pi\Delta\nu/\nu_{fsr}$ where ν_{fsr} is the free spectral range of the cavity and $\Delta\nu$ is the difference between the laser frequency and the cavity resonance frequency [41, 77, 69]. An error signal is then obtained by mixing the output of the photodiode with a portion of the RF modulation drive and passing it through a low pass filter.

2.7.4 Pound Drever Hall error signal: Theory

The theory of PDH error signal is described by Black [77] in a very understandable way. A more rigorous description of the error signal and its frequency response is given by Day in his thesis [69]. A description of the PDH error signal that closely follows the source is presented here, as PDH locking forms a key part of our experiment. The laser field that is incident on the Fabry-Perot cavity can be written as

$$E_{inc} = E_0 \exp(j(\omega_0 t)) \tag{2.33}$$

After the phase modulation, the electric field has a phase-modulated term associated with it and is written as

$$E_{inc} = E_0 \exp(j(\omega_0 t + \beta \sin\Omega t)) \tag{2.34}$$

where β is the phase modulation index and Ω is the phase modulation frequency. The above equation can be expanded using Bessel functions

$$\begin{aligned} E_{inc} &\approx E_0[J_0(\beta) + 2jJ_1(\beta)\sin\Omega t]e^{j\omega_0 t} \\ &= E_0[J_0(\beta)e^{j\omega_0 t} + J_1(\beta)e^{j(\omega_0+\Omega)t} - J_1(\beta)e^{j(\omega_0-\Omega)t}] \end{aligned} \tag{2.35}$$

where J_0 and J_1 are the Bessel functions of order 0 and 1 (note that higher order terms at harmonics of the modulation frequency have been neglected in this expression). It is clear from equation 2.35 that there are three beams incident on the Fabry-Perot cavity: a carrier with angular frequency ω_0, and two sidebands with frequency $\omega_0 \pm \Omega$ [77]. When the modulation index is small ($\beta < 1$), almost all the power is in the carrier and the sidebands. If $P_0 \equiv |E_0|^2$ is the total power in the incident beam then

$$P_c + 2P_s \approx P_0 \tag{2.36}$$

where $P_c = J_0^2(\beta)P_0$ is the power in the carrier and $P_s = J_1^2(\beta)P_0$ is the power in the phase modulation sidebands (note that interference effects have been neglected).

The electric field of the beam reflected from the Fabry-Perot cavity is the total sum of the electric field of three incident beams (carrier and the two sidebands) multiplied by the reflection coefficient of the cavity[9] at the respective frequency [77].

$$\begin{aligned} E_{ref} = E_0[&F(\omega_0)J_0(\beta)e^{j\omega_0 t} \\ &+ F(\omega_0+\Omega)J_1(\beta)e^{j(\omega_0+\Omega)t} \\ &- F(\omega_0-\Omega)J_1(\beta)e^{j(\omega_0-\Omega)t}] \end{aligned} \tag{2.38}$$

where $F(\omega_0), F(\omega_0+\Omega)$ and $F(\omega_0+\Omega)$ are the reflection coefficients of the Fabry-Perot cavity at frequency $\omega_0, \omega_0+\Omega$ and $\omega_0-\Omega$, respectively. Hence, power in the reflected signal ($P_{ref} = |E_{ref}|^2$) measured at the output of the photodetector is

$$\begin{aligned} P_{ref} = &P_c|F(\omega_0)|^2 + P_s\{|F(\omega_0+\Omega)|^2 + |F(\omega_0-\Omega)|^2\} \\ &+ 2\sqrt{P_cP_s}\{Re[F(\omega_0)F^*(\omega_0+\Omega) - F^*(\omega_0)F(\omega_0+\Omega)]\cos\Omega t \\ &+ Im[F(\omega_0)F^*(\omega_0+\Omega) - F^*(\omega_0)F(\omega_0+\Omega)]\sin\Omega t \\ &+ (2\Omega terms) \end{aligned} \tag{2.39}$$

This signal is a wave with a nominal frequency ω_0 and an envelope displaying the beat pattern between the two frequencies. The Ω terms arise from the interference between the carrier and the sidebands, and the 2Ω terms come from the sidebands interfering with each other. The term that is important for the PDH error signal is the one at modulation frequency Ω as it samples the phase of the reflected carrier. At high modulation frequencies ($\Omega \gg \delta\nu_c$, where $\delta\nu_c$ is the linewidth of the cavity) the sidebands are totally reflected, $F(\omega_0 \pm \Omega) \approx -1$. Then,

$$F(\omega_0)F^*(\omega_0+\Omega) - F^*(\omega_0)F(\omega_0+\Omega) \approx -i2Im\{F(\omega_0)\} \tag{2.40}$$

[9]Reflection coefficient $F(\omega)$ is defined as the ratio of the reflected to the incident field. For a symmetric cavity with no losses, it is given by [43]

$$F(\omega) = \frac{E_{ref}}{E_{inc}} = \frac{r(\exp j\frac{\omega}{\nu_{fsr}} - 1)}{1 - r^2\exp j\frac{\omega}{\nu_{fsr}}} \tag{2.37}$$

where r is the amplitude reflection coefficient of each mirror and $\nu_{fsr} = c/2L$ is the free spectral range of the cavity.

and only the sine term at modulation frequency Ω in the equation 2.39 survives. Equation 2.39 can thus be written as

$$P_{ref} \approx 2P_s - 4\sqrt{P_c P_s} Im\{F(\omega_0)\} \sin\Omega t + (2\Omega terms). \tag{2.41}$$

The error signal ϵ is then obtained by mixing[10] the output of the photodiode with a part of the RF modulation signal that provides the phase modulation and passing it through a low-pass filter. It is written as

$$\epsilon \approx -4\sqrt{P_c P_s} Im\{F(\omega_0)\} \tag{2.42}$$

However, in practice there are unequal phase delays in two signal paths at the input of the mixer: the RF signal used for phase modulation and the sine term measured in reflection using the photodiode at the modulation frequency Ω. A phase shifter is required to compensate for these phase delays. Unequal phase delays change the shape of the error signal by affecting the size of signal near resonance.

In the vicinity of the resonance, we can write [77]

$$\frac{\omega_0}{\nu_{fsr}} = 2\pi(N + \frac{\Delta\nu}{\nu_{fsr}}) \tag{2.43}$$

where N is an integer, ν_{fsr} is the free spectral range of the cavity and $\Delta\nu$ is the deviation in the laser frequency from resonance. For a Fabry-Perot cavity with very high finesse (which in our case is ~ 100000) $\mathcal{F} \approx \pi/(1-r^2)$. The reflection coefficient $F(\omega_0)$, is then given by

$$F(\omega_0) \approx \frac{j}{\pi} \frac{2\pi\Delta\nu}{\delta\nu_c} \tag{2.44}$$

where $\delta\nu_c \equiv \nu_{fsr}/\mathcal{F}$ is the cavity's linewidth. The error signal ϵ is then proportional to changes in the laser frequency $\Delta\nu$

$$\epsilon \approx -8\sqrt{P_c P_s} \frac{\Delta\nu}{\delta\nu_c} \tag{2.45}$$

Equation 2.45 shows that the error signal is linear near resonance for a high finesse cavity and its slope D (with units of Hz^{-1}) is

$$D \equiv \frac{-8\sqrt{P_c P_s}}{\delta\nu_c} = \frac{16\mathcal{F}L\sqrt{P_c P_s}}{c} \tag{2.46}$$

The above equation shows that the slope of the error signal depends on the cavity linewidth $\delta\nu_c$ and the power in the carrier P_c and the sidebands P_s.

[10]Mixer is a device whose output is the product of its inputs.

The ratio of the power in the sidebands to the carrier for which the slope is maximum is $P_s/P_c = 1/2$ [77].

There are two main advantages of using the PDH locking scheme for frequency stabilization of a laser. Firstly, in the PDH locking scheme the laser's frequency is locked in reflection to the zero intensity point. This decouples the frequency noise in a laser's output from its intensity noise. Secondly, the error signal obtained using the PDH technique is not limited by the bandwidth of the cavity [45]. This can be explained on the basis of the fact that the reflected beam comprises of two beams [77]: the *promptly reflected* beam (the beam that gets reflected off the first mirror and never enters the cavity) and the *leakage* beam (the small part of the reflected carrier that leaks back through the first mirror). Whenever there is a phase mismatch between the two beams (the *promptly reflected* and the *leakage* beam), an error signal is obtained. When the variations in the frequency of the incident beam

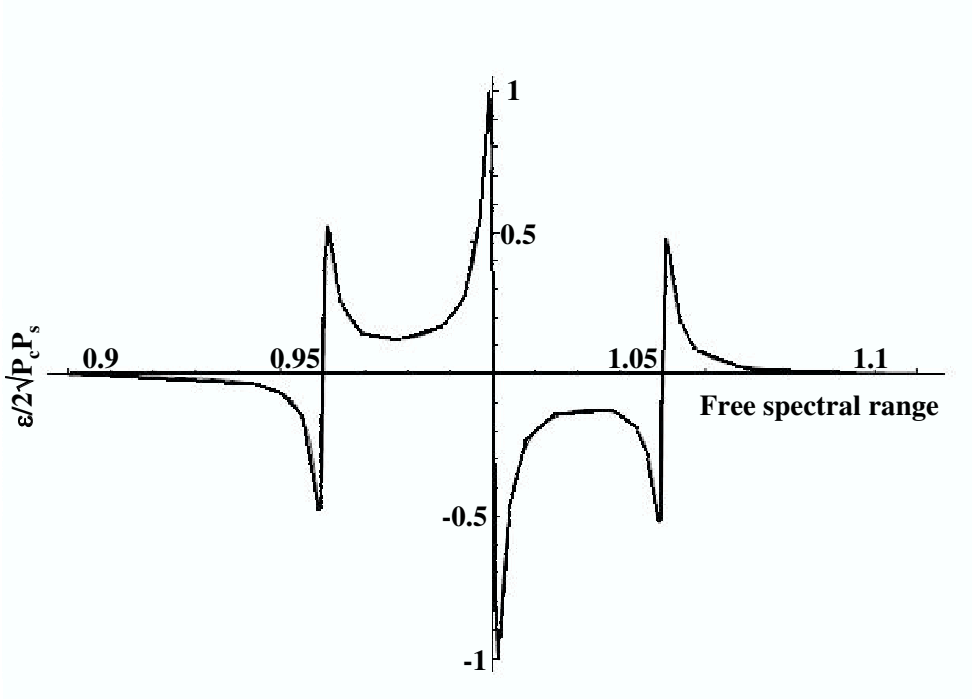

Figure 2.13: The Pound-Drever-Hall error signal, $\epsilon/2\sqrt{P_c P_s}$ [77]

(and the promptly reflected beam) are faster than the storage time of the Fabry-Perot cavity, the cavity's internal field is not in equilibrium with its input [45]. The leakage beam thus provides a stable reference for any fast changes in the frequency of the incident and the promptly reflected beam, by averaging the frequency and the phase of the laser's output over the storage

time of the cavity [77]. Figure 2.13 shows a typical PDH error signal.

2.7.5 The servo

The servo in a control loop amplifies the voltage fluctuations measured by the frequency discriminant and drives the actuator. In low bandwidth control systems, the overall frequency response of a control loop is determined by response of the servo. This is due to the fact that in such systems the response of the actuator and that of the frequency discriminant are flat across the loop bandwidth [69]. Extremely high frequency stabilities $\sim 10^{-15}$ leading to subhertz linewidths can be obtained by suppressing the large $1/f$ component in the spectral density of laser frequency noise at low frequencies below the quantum limit. This is achieved by keeping the gain of the servo loop as high as possible at low frequencies and maintaining a unity gain at frequencies where the lasers become quantum limited in frequency noise. The Nd:YAG lasers used in our experiment become quantum limited in frequency noise at $\sim$ 50kHz and therefore unity gain frequencies of $60 - 100$kHz are adequate [69].

Before discussing the circuit used in our experiment in detail, it will be useful to point out the characteristic features of a Pound-Drever-Hall error signal.

> For frequency fluctuations $\delta\nu$ less than the cavity linewidth $\delta\nu_c$, the PDH error signal acts as a frequency discriminator, whereas outside the cavity linewidth, it is a phase discriminator [45].

$$\epsilon = \begin{cases} f(\nu) & \delta\nu < \delta\nu_c \\ f(\phi) & \delta\nu > \delta\nu_c \end{cases} \tag{2.47}$$

and

$$\nu(t) = \frac{d\phi(t)}{dt} \tag{2.48}$$

Thus

$$\phi(t) = \int d\phi = \int \nu(t)dt \tag{2.49}$$

Equations 2.47 and 2.49 imply that when $\delta\nu > \delta\nu_c$, the PDH error signal is a measure of the integral of frequency fluctuations with time, whereas for $\delta\nu > \delta\nu_c$, it is just a measure of frequency fluctuations. This enables us to use a loop filter circuit with two integral stages, as shown in figure 2.14. The gain of the above circuit has a slope of 12dB/octave at low frequencies and it drops down to 6dB/octave at higher frequencies with unity gain frequency

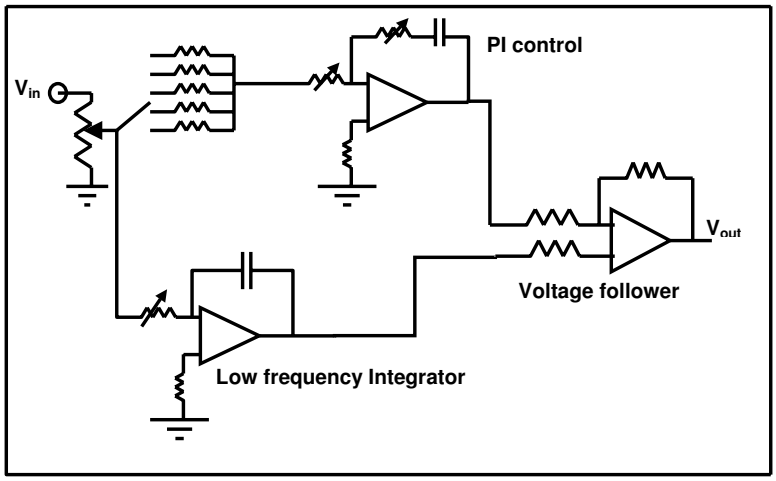

Figure 2.14: Loop filter with by-pass topology. V_{in} is the voltage input, PI is the proportional-integral gain circuit with a cut-off at high frequency and V_{out} is the voltage output of the loop filter.

of $\sim 50 - 100$kHz (see figure 2.16). This can be explained by using a simpler block diagram of the circuit shown in figure 2.15.

> *The two golden rules for working out the behavior of an op-amp are* [78]:
>
> 1. *The output of an op-amp attempts to do whatever is necessary to make the voltage difference between the inputs zero.*
> 2. *The input of an op-amp does not draw any current.*

The following equations can be derived by applying the above-mentioned rules in case of figure 2.15:

$$\frac{V_{in} - V1^-}{Z_1} + \frac{V_{01} - V1^-}{Z_2} = 0 \tag{2.50}$$

$$V1^- = V1^+ = V_{02} \tag{2.51}$$

$$\frac{V_{in} - V2^-}{Z_3} + \frac{V_{02} - V2^-}{Z_4} = 0 \tag{2.52}$$

$$V2^- = V2^+ = 0 \tag{2.53}$$

From equation 2.50, the output of the circuit V_{01} can be written as

$$V_{01} = -\frac{Z_2}{Z_1}(V_{in} - V1^-) + V1^- \tag{2.54}$$

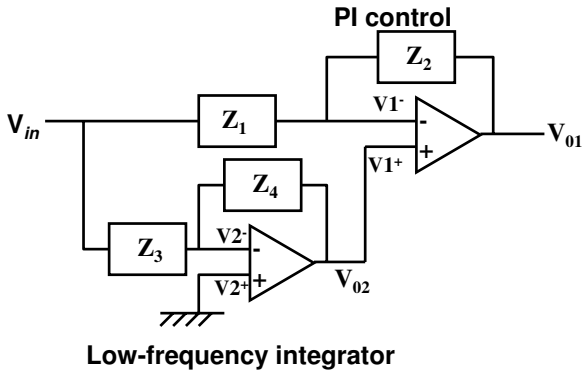

Figure 2.15: Simplified circuit for loop filter shown in figure 2.14. The voltage follower is not included in this circuit. PI control is the Proportional Integral control. Z_1, Z_2, Z_3 and Z_4 are impedances used in the PI control and low frequency integrator circuit respectively.

and substituting equation 2.53 in 2.52, we get

$$V_{02} = -\frac{Z_4}{Z_3}(V_{in}) \tag{2.55}$$

Substituting equation 2.55 and 2.51 in 2.54, the gain of the circuit shown in figure 2.14 is

$$\frac{V_{01}}{V_{in}} = -\left(\frac{Z_2}{Z_1} + \frac{Z_2}{Z_1}\frac{Z_4}{Z_3} + \frac{Z_4}{Z_3}\right) \tag{2.56}$$

In general, the total gain G of the circuit can be written as

$$G = G1 + G1G2 + G2 \tag{2.57}$$

where $G1 = Z2/Z1$ is gain of the first op-amp and $G2 = Z2/Z1$ is gain of the second op-amp. The gain versus frequency plot of the circuit when $G1 > G2$ is shown in the figure 2.16

The first roll-over occurs at frequency f_2 corresponding to the cavity linewidth $\delta\nu_c$. For frequency fluctuations greater than $\delta\nu_c$, the error signal is already an integral measure of the frequency fluctuations. With no roll-off at this frequency, the circuit will oscillate due to the high integral gain. f_2 is the unity gain frequency; it corresponds to the point where the lasers become quantum limited in frequency noise. The second roll-over occurs at f_3 to avoid oscillations in the circuit at very high frequencies. In all, the circuit described above has a very high gain at low frequencies and exploits the full potential of PDH error signal to obtain high frequency stability leading to narrow linewidths.

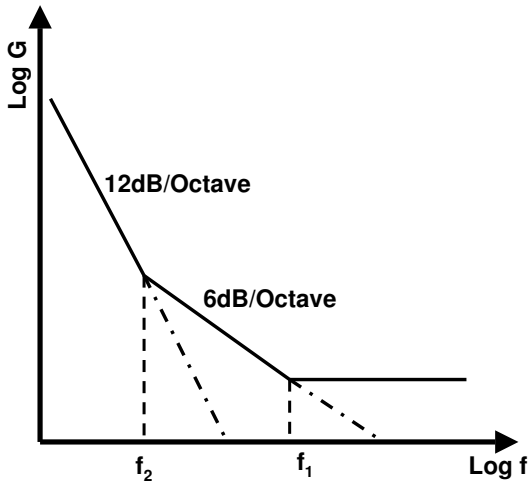

Figure 2.16: Plot of the total gain of the circuit with respect to frequency, when $G1 > G2$. $G1$ is the gain of the PI control circuit and $G2$ is the gain of the low frequency integrator. f_2 is the cut-off for the low frequency integrator and f_1 is the cut-off for the PI control.

2.7.6 Actuator

An actuator in the control loop converts the amplified voltage fluctuations at the output of the servo to frequency changes in the laser. There are several ways in which this can be achieved in a Mephisto 1200 NE or any other commercially available laser. The actuating element available in almost all the commercially available laser systems is a PZT (piezo electric transducer). In the Mephisto system, the PZT has a tuning coefficient of 1-2MHz/V. It is attached to Nd:YAG laser crystal that is non planar ring oscillator resonator. When a modulating signal is applied to the PZT optical beam path changes due to the stress induced birefringence [133, 134], which, in turn, changes the frequency of the laser. High frequency modulation ($\sim$ 100kHz) of the laser's frequency can be obtained using a PZT. However, the voltage that can be applied to the PZT is limited in the range of -100V to $+100$V, which limits the tuning range to few hundreds of MHz.

Slow frequency ($\sim$ 1Hz) tuning of the laser's frequency can be obtained by applying low frequency modulation to the temperature of the laser crystal. It has a tuning coefficient of -3GHz/K. The temperature of the laser crystal changes by 1K/V when a modulating voltage is applied to the temperature controller's modulation input. This input is used to compensate for slow frequency drifts associated with the temperature controller inside the laser system. This will be discussed in more detail in the next chapter.

Another actuating element in an Nd:YAG laser system is the current

input of the pump laser diode. A modulation signal applied to the current input of the pump diode, modulates the pump power and therefore the temperature of the NPRO mode volume. This is similar to the temperature control of the laser crystal. However, the volume that is controlled in this manner is small and thus the response can be fast ($\sim$ 1kHz) compared to the direct temperature modulation of the laser crystal.

The actuating element in the control loop determines its bandwidth. Large bandwidths are required to provide better frequency control. The PZT is therefore the obvious choice as the actuator for a frequency control experiment. In our experiment fast frequency control is obtained using the PZT attached to the laser crystal inside Mephisto 1200 NE. The temperature control of the laser crystal is used as the actuating element for compensating the slow drifts in the laser frequency.

2.7.7 Fundamental limits - how good can we get?

According to equation 2.32, the minimum closed loop spectral density of laser frequency noise in the case of sufficiently high servo gain, is determined by the discriminator slope and its noise spectral density. Equation 2.46 gives the slope of the discriminator and in an optimally designed system the noise spectral density of a discriminator is determined by the quantum limited shot noise in the photo-detector output [69]. However, it is clear from equations 2.38 and 2.37 that on resonance in an impedance matched cavity ($F(0) = 0$), only the DC contribution from the sideband power, $2{J_1}^2(\beta)P_i$ contributes to the shot noise at the photodetector. Therefore, the discriminator shot noise spectral density of current, $S_{\mathrm{A,disc}}$ ($\mathrm{A}/\sqrt{\mathrm{Hz}}$), with that power level is given by

$$S_{\mathrm{A,disc}}(\mathrm{A}/\sqrt{\mathrm{Hz}}) = \sqrt{2}\sqrt{2eI} = \sqrt{2}\sqrt{2e\left(2{J_1}^2(\beta)\frac{e\eta P_i}{h\nu}\right)} \tag{2.58}$$

where I is the detector photo-current induced by the DC power level, ${J_1}^2(\beta)P_i$, and $h\nu$ is the energy of the detected photons. This implies that the frequency stability in case of a PDH locking scheme is limited just by the photon shot noise in the photodetector.

2.8 Conclusion

The theory and background behind the frequency stabilization techniques used in this thesis has been discussed in this chapter. The major components

of the frequency control system were identified as the laser, the frequency discriminator, the servo and the actuator. A detailed description of the various measures of the laser noise and frequency stabilization has also been presented.

Chapter 3

Ultrastable cavities for fundamental physics experiments: a review

3.1 Introduction

As discussed in chapter 1, optical resonators with frequency stabilities of the order of $\sim 10^{-15}$ or higher are required for several fundamental physics experiments, namely, Tests of relativity [31, 34, 36], Lorentz invariance [32, 33], Gravitational wave detection, etc. This chapter discusses some of the experiments that are being performed using ultrastable cavities.

3.2 Tests of Special Relativity

Einstein's theory of special relativity forms the basis of all accepted theories of physics at the fundamental level. It is, therefore, necessary to test this theory with ever increasing precision. Experimental tests of the Special theory of Relativity(SR) attempt to either validate it or find discrepancies leading to tiny violations. These tests are stimulated by an attempt to unify gravity with the other forces of nature. It is hoped that in this way a deeper understanding of physical reality might emerge. One such 'unified' theory is Quantum Gravity. This is an attempt to reconcile quantum mechanics, which underpins the standard model of electro-weak and strong interactions, with general relativity, currently the most complete theory of gravitation.

The two main postulates of Special Relativity as stated by Einstien in his classic paper on 1905 [83] can be stated in more modern language as follows:

1. The laws of physics are the same in any inertial (that is, non-accelerated) frame of reference. This means that the laws of physics observed by a hypothetical observer traveling with a relativistic particle must be the same as those observed by an observer who is stationary in the laboratory.

2. The speed of light is the same for all observers no matter what there relative speeds are.

According to the kinematical analysis of Robertson [82], Mansouri and Sexl [81], the three experiments that test the basis of Special Relativity are: the isotropy of space (Michelson-Morley experiments), the independence of the speed of light from the velocity of the laboratory (Kennedy-Thorndike (KT) experiments), and time dilation[1](Doppler spectroscopy experiments). The Robertson-Mansouri-Sexl framework describes a general transformation between a moving frame S with velocity v with respect to a preferred frame Σ (Figure 3.1). The speed of light, c, is assumed to be constant in Σ and in general transforms to a non-constant value, $c_S(\theta, v)$ dependent on the angle θ of light propagation with respect to the direction and magnitude velocity, v of the moving frame. The fractional difference between c and $c_S(\theta, v)$ according

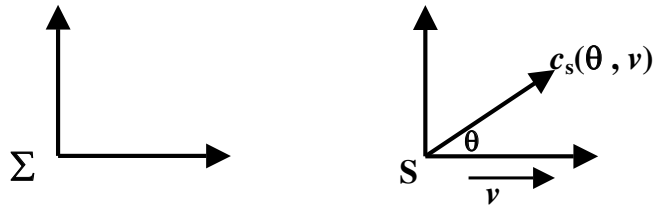

Figure 3.1: Schematic of the moving frame S, with respect to the preferred frame

to this transform is given by the Robertson-Mansouri-Sexl (RMS) equation :

$$\chi(\theta, v) = \frac{c_S(\theta, v)}{c} \tag{3.1}$$

and thus,

$$\chi(\theta, v) = \chi_{MM}(v)\sin^2(\theta) + \chi_{KT}(v) \tag{3.2}$$

[1]According to Einstein's theory of special relativity, the observed time for events is dependent upon the speed of the observer relative to the speed of the reference frame in which the events are occurring. This is termed as time dilation. For example, a moving clock running with a velocity v in an inertial frame appears to run slower to a stationary observer.

where,

$$\chi_{MM}(v) = (\frac{1}{2} - \beta + \delta)\left(\frac{v}{c}\right)^2 \tag{3.3}$$

and

$$\chi_{KT}(v) = (\beta - \alpha - 1)\left(\frac{v}{c}\right)^2 \tag{3.4}$$

In equation 3.1, α is the time dilation parameter, β the length contraction parameter parallel to v, and δ the length contraction parameter perpendicular to v. The Michelson-Morley(MM) experiment tests the first term in the above equation, while, the Kennedy-Thorndike(KT) experiment tests the second term. Because of the $\sin^2(\theta)$ dependence, length contractions occur at twice the frequency of the rotation of the experimental setup.

3.2.1 Michelson-Morley(MM) Experiment

The isotropic nature of the speed of light forms a central feature of the Einstein's theory of Special Relativity. The Michelson-Morley experiment is an effective tool to test the isotropy of the speed of light. Originally this experiment was carried out by Michelson and Morley to test the ether theory in 1887. Before Michelson and Morley carried out this experiment, it was believed that space was filled with a transparent substance called ether. This substance facilitated the movement of electromagnetic and gravitational forces through empty space. Michelson and Morley conducted an experiment to measure the earth's velocity through this ether assuming the earth is not special and therefore not at rest with respect to the ether. The classical set-up (Figure 3.2) of a Michelson-Morley experiment involved comparing the speed of light c in two equal orthogonal interferometer arms by observing the interference fringes.

Light from a arc/vapour lamp source S is divided into two orthogonal paths AB and AC using a beam-splitter at point B. The two light beams are then reflected back by mirrors at point A and C and combined at the beam-splitter to form interference fringes, which are viewed by the telescope. Isotropy of the speed of light c is then tested by rotating the whole set-up (using either the Earth's rotation or a turntable) and measuring movement of the interference fringes. A finite movement of the fringes would imply a violation in the isotropic nature of the speed of light. In the initial experiment, the light was repeatedly reflected back and forth along the arms AB and AC of the interferometer such that the path length was increased to 11m. Thermal and vibrational effects were reduced by setting up the experiment in a closed room in the basement of a stone building. Vibrations were further reduced by building the apparatus on top of a huge block of marble, which

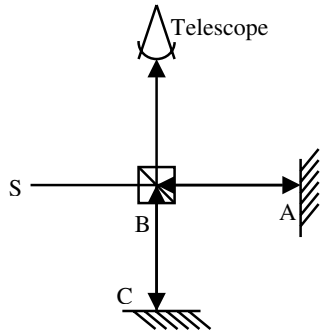

Figure 3.2: Schematic of Michelson Morley experiment. Light from a source S is divided into two orthogonal paths AB and AC using a beam-splitter at point B. The two light beams are then reflected back by mirrors at point A and C and combined at the beam-splitter to form interference fringes that are viewed on a telescope.

was then floated in a pool of mercury. However, a null result was obtained in this experiment with a calculated measurement accuracy of $\sim 1/100$th of a fringe [84] limited mainly by the linewidth of their source. This led to the conclusion that ether did not exist. In 1905, when Einstein published his 'Special Theory of Relativity' (which showed that all motion is relative), the whole concept of the ether was abandoned. However, it was hard for physicists to accept this theory without any experimental evidence. Hence, several improvements in the experimental set-up have since been made, to improve the accuracy of the measurement.

In recent versions of the Michelson-Morley experiment, increased accuracy has been achieved by using frequency stabilized lasers rather than a simple light source. The Brillet and Hall experiment [88] conducted in 1979 measured a laser's frequency after stabilization to a resonance of an ultra-stable Fabry-Perot cavity (Figure 3.3). As, frequency can be measured more accurately than wavelength (in fact, frequency is the most accurately measured quantity in science), this approach provided a distinct advantage by converting the length measurement of Michelson-Morley experiment (fringe-shift) to a frequency measurement.

The frequency of such a resonance is given by $\nu_{cav}(= mc/2L)$, where L denotes the cavity length, c the speed of light and $m = 1, 2, ...$ is the mode number. Any violation of the isotropy of the speed of light would be detected by rotating the Fabry-Perot cavity and looking for a resulting variation in the cavity resonance frequency ν_{cav}. This is measured by comparing the frequency of the cavity stabilized laser to a suitable reference. This measurement put a limit on such an anisotropy of $(3 \pm 5) \times 10^{-15}$. The ultra

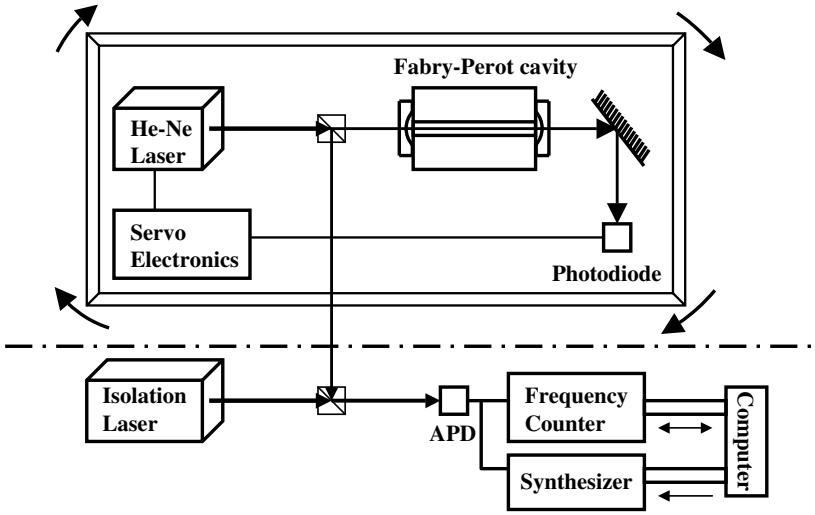

Figure 3.3: Schematic of Brillet and Hall Experiment. A He-Ne laser (3.39μm)is servo-stabilized to a transmission fringe of an isolated and highly stable Fabry-perot cavity, with a provision of rotating the whole system. A small portion of this laser beam is picked off using a beam splitter and a heterodyne beat measurement is performed with an 'isolation laser' which is stabilized to CH_4-stabilized reference laser. The beat frequency is shifted and counted under mini computer control, these frequency measurements being synchronized and stored relative to the table's angular position. After 30 minutes of signal averaging the data are fourier transformed and printed and the experiment is re-initialized [88].

low expansivity glass cavities used in this experiment suffer from isothermal creep (drift rates $\sim$ 10 kHz/day) due to their amorphous nature. This creep is significant over 6 hours (90 degree rotation time of the earth) and therefore it is not possible to use the earth's rotation solely for the experiment. Hence, a turntable that can be rotated at a faster rate (i.e. faster than the effects of the creep) is required to overcome this drift. The precision in Brillet and Hall's experiment is therefore limited by systematic effects associated with the rotation table.

In 2003, another modified Michelson-Morley experiment was performed by Müller *et al.* using cryogenic optical resonators (COREs) made from mono-crystalline sapphire. The basic principle behind this modern Michelson-Morley experiment is to compare the velocity of light in two orthogonal directions c_x and c_y. In the experimental setup (Figure 3.4), the frequencies of two Nd:YAG lasers are '*locked*' (stabilized) to the resonances ν_x and ν_y of two similar mono-crystalline sapphire Fabry-Perot cavities mounted in orthogonal directions inside the same liquid He cryostat. A variation in the difference between the two frequencies $(\nu_x - \nu_y)$ induced by the rotation of the experimental set-up implies a violation of the isotropy of the speed of light c, in contrast to the postulates of special relativity.

High stabilities of cryogenic optical resonators (COREs) made from crystalline sapphire (thermal expansion coefficient $\sim 10^{-10}$ at 4.2K and relatively low isothermal creep of ≤ 0.1 Hz/hour) make them a valuable tool for such an experiment. The absence of isothermal creep allows one to solely use the earth's rotation for the Michelson-Morley experiment as compared to previous experiments where a rotating turntable was used to overcome the drift rates of $\sim$ 10 kHz/day in ULE cavities that is significant over 6 hours (90 degree rotation time). The two cryogenic cavities used in the experiment performed by Müller *et al.* have lengths $L = 3cm$ and feature linewidths of 100 and 50 kHz respectively (Finesses $\sim 10^5$). The frequencies of two diode pumped Nd:YAG lasers at 1064nm were stabilized to resonances of these cryogenic cavities located inside a liquid He cryostat, using the Pound Drever Hall frequency stabilization scheme. A minimum relative frequency instability of $\sim 7 \times 10^{-16}$ (Figure 3.5) was achieved over a few minutes. An isotropy violation parameter, $\beta - \delta - \frac{1}{2} = (-2.2 \pm 1.5) \times 10^{-9}$ within the Robertson-Mansouri-Sexl (RMS) framework [82] was calculated. The test data were taken over a period of a year and fitted into the Standard Model Extension framework. The Standard Model Extension (SME) [98, 99] framework extends the Robertson-Mansouri-Sexl framework, which yields equation 3.1, to incorporate the modern string and quantum gravity theories. The SME starts from a Lagrangian of the Standard Model, adding all possible observer

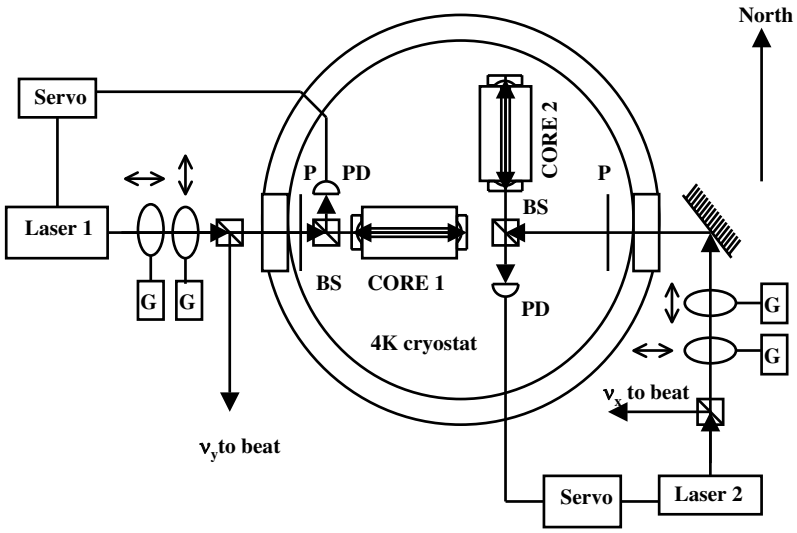

Figure 3.4: Experimental setup of Müller's [30] Michelson Morley experiment. Inside a 4K cryostat, two COREs are located in a copper block to provide common mode rejection of thermal effects. LN_2 is filled every ~ 3 h, LHe manually every ~ 2 days. Laser beams are coupled to the COREs via windows, with polarizers P and lock detectors PD inside the cryostat. For active beam positioning, beams pass through galvanomter (G) mounted glass plates. The horizontal and vertical displacements are adjusted to maximize coupling into the cavities, as measured using the $2f_m$ signal from the detector in reflection.

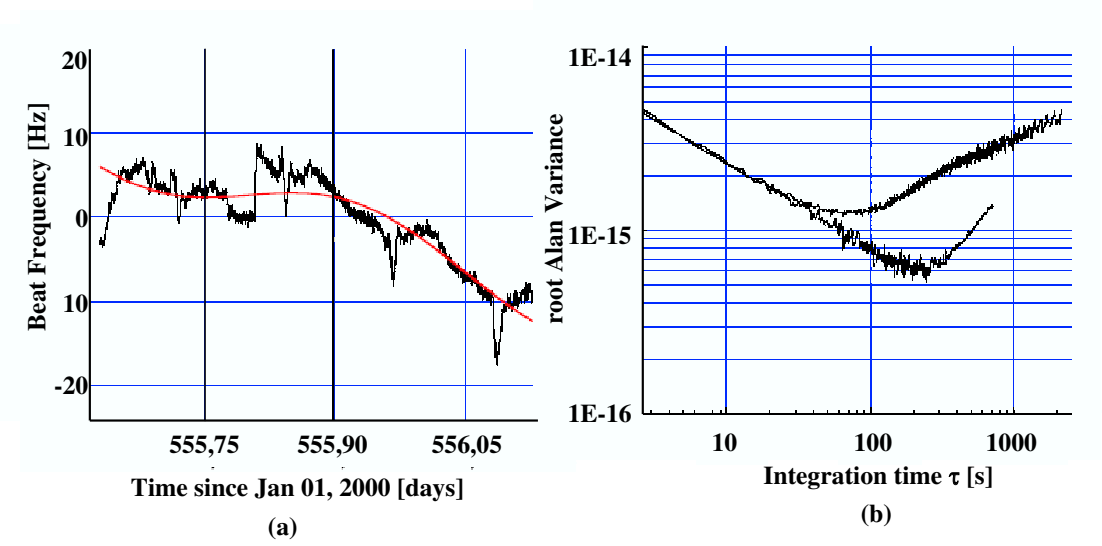

Figure 3.5: (a) Beat frequency data measured over time fitted with a 12h sine amplitude, a linear drift, and a constant offset. Peaks occur due to automatic LN_2 refill. (b) The upper curve shows root Alan variance of the beat frequency calculated from the beat frequency data shown in (a). Lower curve shows the root Alan variance from the data taken during a quiet part between two LN_2 refills (118 min starting at 555.87 days) [30].

Lorentz scalars that can be formed from the known particles and Lorentz tensors. In what is known as the 'photonic sector' Lagrangian is given by

$$L = -\frac{1}{4}F^{\mu\nu}F_{\mu\nu} + \frac{1}{2}(k_{AF})^{\kappa}\varepsilon_{\kappa\lambda\mu\nu}A^{\lambda}F^{\mu\nu} - \frac{1}{4}(k_F)_{\kappa\lambda\mu\nu}F^{\kappa\lambda}F^{\mu\nu} \tag{3.5}$$

where F_μ is the electromagnetic field tensor and A_μ is the vector potential.

An upper bound to the anisotropy in the speed of light, c of $\triangle c_\theta/c_0 \sim (2.6 \pm 1.7) \times 10^{-15}$ was calculated.

A further ten-fold improvement in the above result has been achieved by Antonini *et al.* [89] by setting up the same experiment on an active rotation table. An active rotation table requires the apparatus to be stable over individual rotation periods rather than stationary experiments that must be stable over 12 hours. Moreover, the data acquisition rate of a stationary experiment is much lower than that of a rotating experiment. In stationary experiments only four data points can be measured over a 12 hour period, as compared to rotating experiments where 2 data points can be measured for each rotation. In the above experiment the chosen rotation period is 10 min and the data are acquired over a period of 72 hours. These data are analyzed using the Robertson-Mansouri-Sexl framework and an isotropy violation parameter of $\beta - \delta - \frac{1}{2} = (-0.5 \pm 3) \times 10^{-10}$ has been reported.

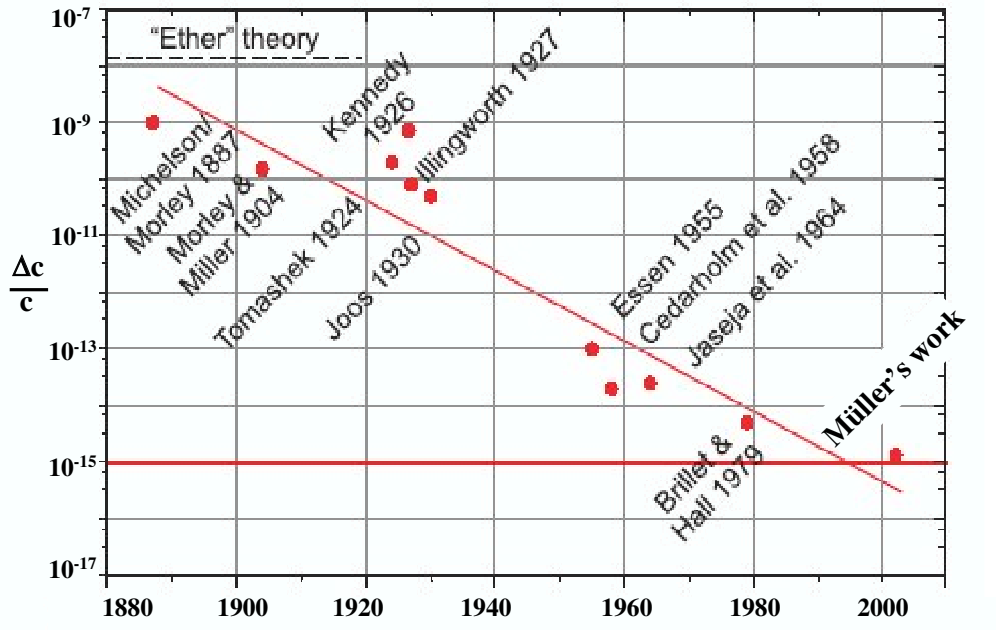

Figure 3.6: Accuracy of tests of the isotropy of electromagnetic wave propagation. Experiments until 1930 were performed using optical interferometers, later experiments using electromagnetic cavities. The last three used lasers [30].

Figure 3.6 summarizes the results obtained by various experiments that test the isotropic nature of the speed of light.

3.2.2 Kennedy-Thorndike(KT) Experiment

The original Kennedy-Thordike experiment was conducted in 1932 and was a modified form of the Michelson-Morley experiment discussed in section 3.2.1. This experiment is an important tool to test the independence of the speed of light, c with respect to the velocity of the laboratory v. The main difference between the two experimental setups was to make the length of the two interferometer arms unequal. Figure 3.7 shows the Kennedy and Thorndike experimental setup. The mathematical analysis of Michelson-Morley experiment described by Rothman in Appendix III of his book [87] shows that by making the interferometer with unequal arms, one can measure the effect of the earth's motion on the velocity of light, if such an effect exists.

In the Kennedy-Thorndike experiment, measurements had to be taken over extended periods of time and thus it was necessary to avoid changes in the length of the interferometer arms due to temperature fluctuations. The length fluctuations were kept down to 2×10^{-10} by making the essential parts of the apparatus out of fused quartz, which has a very low thermal

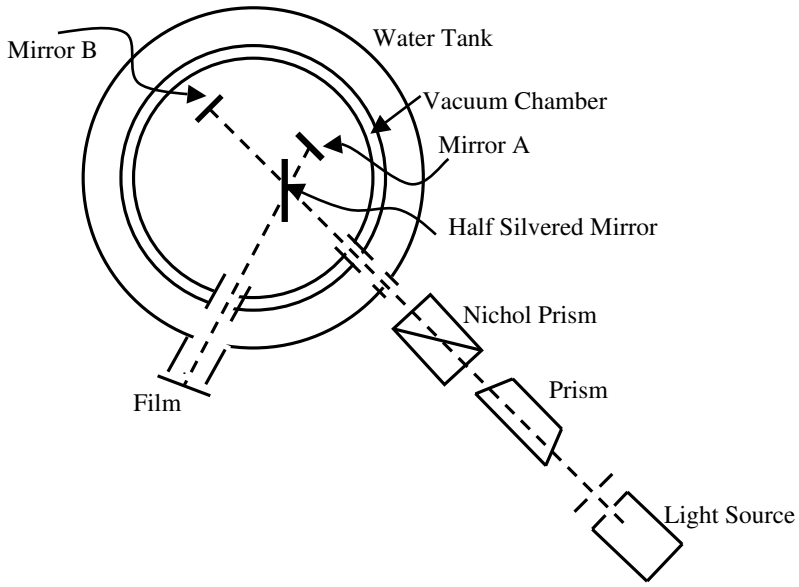

Figure 3.7: Kennedy-Thorndike apparatus. The light source used was a Mercury arc lamp. The beam was sent through the prism to select only single spectral line and then a Nichol's prism was used to polarize the light. The water tank and vacuum chamber were designed to ensure a constant temperature across the interferometer arms [87].

expansion coefficient, and thermostatically controlling the temperature of the water tank in which the vacuum chamber was enclosed. A further reduction in temperature fluctuations was achieved by keeping the apparatus inside two rooms-within-rooms that were temperature controlled. It was possible to achieve a temperature stability of ~ 0.001 degrees using the above setup. The experiment was performed by setting up the interferometer to obtain interference fringes using the mercury green line at 546nm. The interference fringes were photographed on a plate and six sets of measurements were obtained by changing the distance of the film, at half hour intervals. After twelve hours, the same measurements were repeated keeping the distance change in each measurement the same as the previous one. The plates were then microscopically examined to search for any fringe shift due to rotation of the earth. Further sets of measurements were taken every three months for nine months to study effects due to the orbital motion of the earth. However, the fringe shift that was observed was so small that it was considered to be a null measurement.

The Kennedy-Thorndike experiment was repeated in 1990 by Hills and Hall [90]in Boulder, Colorado using cavity stabilized lasers. This version of the experiment transforms the measurement of a fringe shift into a relative frequency measurement. The experimental setup(figure 3.8) consisted of two lasers, one stabilized to a very stable Fabry-Perot cavity made of ULE(ultra-low expansivity) glass and other to a molecular absorption line in I_2. The frequencies of these lasers were compared using optical heterodyne detection. The velocity v of the laboratory is calculated with respect to Microwave Background frame as suggested in the Robertson-Mansouri-Sexl framework. The main sidereal[2] components found by working in the earth's equatorial frame are given by equation 3.6

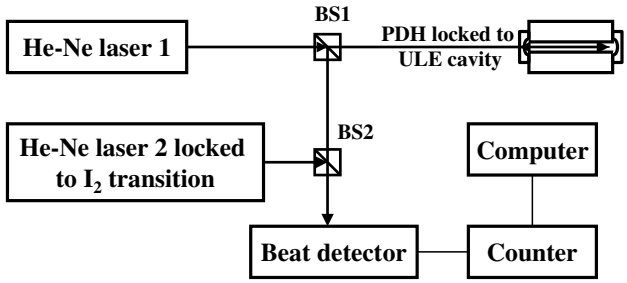

Figure 3.8: Schematic of the laser based Kennedy-Thorndike experiment. BS1 and BS2 are the beam splitters used to pick off small portions of each laser beam to perform heterodyne beat detection.

[2]measured relative to the stars

$$\frac{v^2}{c} = \left(\frac{u}{c}\right)^2 + 2\left(\frac{u}{c}\right)\left(\frac{\omega R_\oplus}{c}\right) \times \cos\phi_L \cos\delta_\mu \sin[\omega(t - t_s) + \Phi] \qquad (3.6)$$

where $u = 377 \pm 14$ km/s is the velocity of Earth with respect to the microwave background frame, $\omega = (2\pi/P_\oplus)$ with $P_\oplus$ being the sidereal period and $R_\oplus$ the Earth radius, $\phi_L = 40^\circ$ is the latitude of Boulder and $\delta_\mu = -6.4^\circ \pm 1^\circ$ is the observed inclination of the microwave background velocity vector and Φ is the phase at the start of analysis. Equations 3.6 and 3.1 imply that determination of the factor $\beta - \alpha - 1$ depends on the ability to measure 24 hour sidereal variation of the beat frequency. The beat frequency is counted over 40 seconds and several sets of readings were taken including continuous periods of 15 and 90 days. The calculated value of $\beta - \alpha - 1$ was determined to be $< 6.6 \times 10^{-5}$. The main drawback of this experiment was that the ULE cavity used in this experiment suffers from isothermal creep due to the *aging* effects (relaxation) in the material. This effect implies a beat frequency drift of ~ 1.65 Hz/s (3×10^{-10}/day or 1.1×10^{-7}/year) and needs to be subtracted from the measurement.

In 2002, Braxmaier *et al.* from Müller's group, repeated this experiment using cryogenic optical resonators (CORE) [36]. Figure 3.9 shows the setup of their Kennedy-Thorndike experiment. The cryogenic optical resonators at liquid Helium temperature used in this experiment do not suffer from isothermal creep as in case of the Ultra Low Expansivity (ULE) glass cavities used in Hall's experiment. This isothermal creep in ULE cavities (of the order of $\sim$ 1kHz/hour) limits their use to search for daily variation in the speed of light $c(v)$ with respect to speed of laboratory v. In contrast to ULE cavities, crystalline resonators operated at liquid Helium temperatures have no discernable drift and this allows a 100 fold larger orbital modulation of velocity of the laboratory v. A Nd:YAG laser is stabilized to the frequency of a cryogenic optical resonator (CORE) using the Pound Drever Hall frequency stabilization scheme. As a reference, a second laser is stabilized to an electronic transition ν_{mol} between two rotation-vibrational levels of different electronic states of the iodine molecule I_2. The finesse of the CORE used in this experiment is $\sim 100,000$ and its temperature is stabilized at 4.3K for the whole measurement. The beat between the two frequency stabilized laser systems is measured. With such an arrangement no systematic drift was observed on the time scale of a few hours. The standard Allan deviation was measured to be about 6×10^{-13} for integration times between 1 and 10^4 secs. The frequency difference $\nu_{res} - \nu_{mol}$ between an I_2 molecular frequency reference and a cryogenic optical resonator (CORE) was measured over 190 days. The laboratory velocity $v(t)$ has contributions from the following:

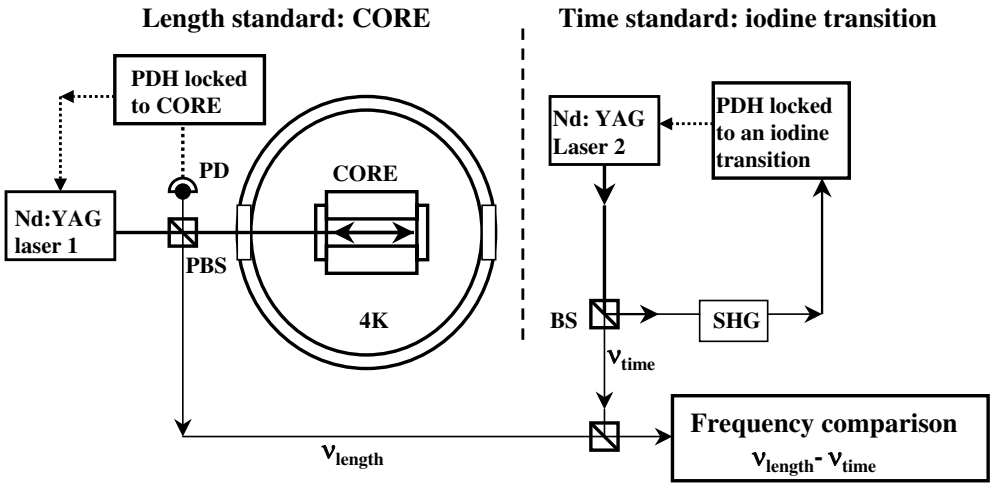

Figure 3.9: Experimental setup for Braxmaier *et al.* experiment. Nd:YAG laser 1 is locked to the cryogenic optical resonator using PDH locking scheme where PBS is the polarizing beam splitter and PD is the photodiode. Frequency of Nd:YAG laser 2 is doubled using single harmonic generation (SHG) and then locked to an iodine transition using the PDH locking scheme.

- motion of the sun through the microwave background Σ with a constant velocity, $v_s = 377Km/s$
- Earth's orbital motion around the sun, orbital velocity, $v_e = 30$Km/s, and
- Earth's daily rotation velocity, $v_d \approx 330$Km/s in Konstanz where the experiment was performed.

Equation 3.7 defines the velocity of the laboratory with respect to the motion of the earth [36].

$$v(t) = v_s + v_e \sin[\Omega_y(t - t_0)] \cos \Phi_E + \nu_d \sin[\Omega_d(t + t_d)] \cos \Phi_A \qquad (3.7)$$

where $\Phi_A \approx 8^\circ$ is the angle between the earth equatorial plane and the velocity of the sun, $\Phi_E = 6^\circ$ is the declination between the plane of the Earth's orbit and the velocity of sun, $2\pi/\Omega_y = 1yr$, $2\pi/\Omega_d = 1$ sidereal day. t_0 and t_d are determined by the phase and start date of the measurement, respectively. a relative signal amplitude $\Delta\nu/\nu = \Delta c/c = (4.8 \pm 5.3) \times 10^{-12}$ was measured with a laser frequency of $\nu_{res} = 282$ THz, which implied $(\beta - \delta - 1) = (1.9 \pm 2.1) \times 10^{-5}$. This result is a three-fold improvement to the Hall's result is by far the most accurate measurement in the Kennedy Thorndike (KT) experiment.

3.3 Optical Frequency Standards and Measurements

The next generation of high accuracy and high-stability frequency standards are likely to be based on spectrally narrow optical transitions in atoms or ions probed by ultra-stable lasers. The advantages of using optical frequencies as compared to microwave frequencies have already been described in chapter 1. Realization of ultrastable lasers and an innovative practical scheme for measuring optical frequencies have provided scientists essential tools to realize the potential of optical frequency references. Lasers locked to ultrastable cavities described in this thesis form the basis of precision spectroscopic measurements of laser cooled atoms or ions.

In 1983, Jennings *et al.* demonstrated for the first time that optical frequencies can be measured using a harmonic frequency chain [91, 92]. This technique is termed as *Optical Frequency Synthesis*. Their experiment involves locking a series of radiation sources with ever-increasing frequencies in a sequence of harmonics from the microwave to the visible part of the spectrum. This led to the first ever direct measurement of the frequency of the 633 nm line of the iodine-stabilized helium-neon laser [91], and the frequency of 576 nm line in iodine [93] to few parts in 10^{10}. From 1983 to the late 1990s, optical frequency measurements continued to improve in terms of fractional frequencies, from $\approx 10^{-10}$ to 10^{-13}. However, with improvements in laser stabilization techniques, better atomic references using cold atoms and ions and femtosecond-optical-frequency metrology, optical frequency measurements have advanced considerably ($\sim$ 3 orders of magnitude) in the last few years.

The major breakthrough in the field of optical frequency measurements was achieved by Hänsch's group in 1999 [94, 95], when they demonstrated for the first time that mode-locked femtosecond lasers can be used to span large optical frequency intervals accurately. In such a set-up, the output of a mode-locked Ti-sapphire ring laser with a repetition rate of 1GHz is broadened inside a non-linear microstructure fiber. A broad description of the physics of the broadening mechanism associated with the fibre, non-linear microstructure fiber can be found in references [124, 125]. The repetitive train of pulses produced by stable mode-locked laser appears in the frequency domain act as a comb of discrete modes separated by the frequency associated with the pulse repetition rate f_r. Figure 3.10 shows the broadening of the laser beam after it has passed through the non-linear microstructure fiber. If the evenly spaced comb of optical frequencies were extrapolated to zero frequency, there would, in general, be an offset from zero by some amount

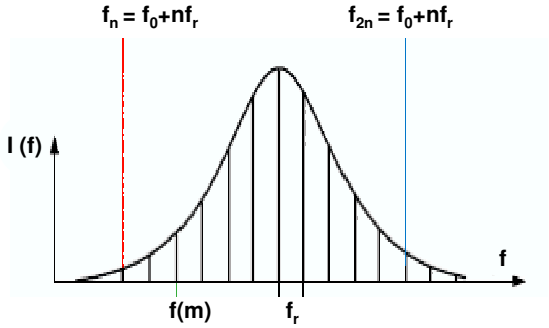

Figure 3.10: Intensity versus frequency graph after laser beam has passed through the non-linear microstructure fiber. f_r denotes the pulse repetition rate and f_m denotes the mode frequency.

f_0. The offset f_0 results from the difference between the group and phase velocities of the ultrashort pulses traversing the laser cavity [94, 126]. Hence, the frequency of any mode of the optical comb can be given by the following equation:

$$f(m) = f_0 + m \times f_r \tag{3.8}$$

where, f_{rep} is the spacing between the modes given by the pulse repetition rate, f_0 is the offset frequency and m is an integer. The repetition rate f_{rep} is detected in a fast photodiode that monitors light coming out of the microstructure fiber. The offset frequency can be detected using the *self-referencing* method developed at JILA and MPQ [126, 127]. This method is shown schematically in figure 3.11. The infrared portion of the optical comb f_n (near 1100 nm) from the microstructure fiber is frequency doubled in a $KNbO_3$ crystal to generate light at 520 nm, which is then recombined (after an optical delay) on a photodiode with f_{2n} (520-nm) light generated in the microstructure fiber. The resulting beat-note gives the desired offset frequency.

$$f_0 = 2f_n - f_{2n} = 2(f_0 + n \times f_r) - (f_0 + 2n \times f_r) \tag{3.9}$$

The offset frequency f_0 is locked to the H-maser (Hydrogen maser) via the electro-optic modulator in pump beam. f_r is controlled by another servo system that drives the PZT on the Ti:Sapphire laser's ring cavity. This setup has been used to measure the absolute frequencies of Hg^+ and Ca standard relative to the Cs primary frequency standard at NIST [128]. The frequencies of the mercury ion and calcium, $f(Hg^+)$ and $f(Ca)$ relative to the caesium (Cs) clock frequency were measured to be:

$$f(Hg^+) = 1{,}064{,}721{,}609{,}899{,}143(10) \text{ Hz}$$

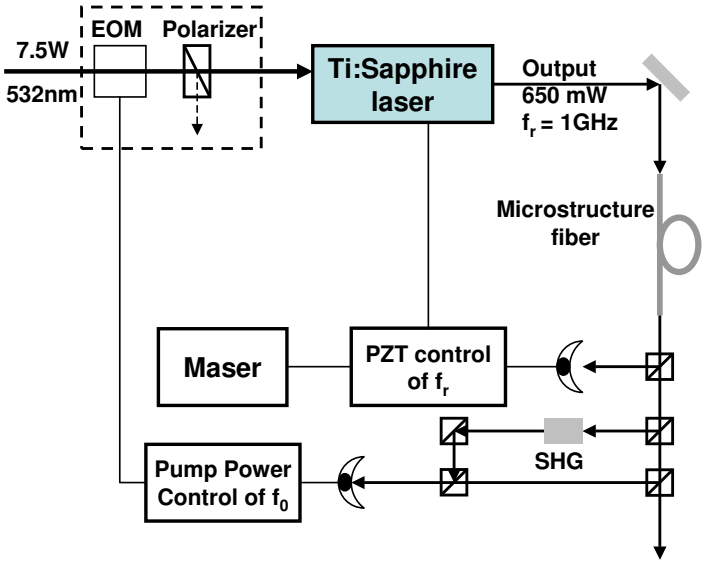

Figure 3.11: Femtosecond-laser-based optical *clockwork* with a one gigahertz repetition rate. The output of the mode-locked Ti : sapphire ring laser is broadened in a microstructure fiber. The IR portion is then frequency-doubled using single harmonic generation (SHG) back to the green using $KNbO_3$ and recombined with the original green from the fiber. This produces a signal at the offset frequency (f_0) that is locked to the H-maser via the electrooptic modulator in the pump beam. A second servo system drives the PZT on the ring cavity to control the repetition rate f_r [3].

and

$$f(\mathrm{Ca}) = 455{,}986{,}240{,}494{,}158(26)\ \mathrm{Hz}$$

This corresponds to an accuracy $\Delta f(\mathrm{Hg}^+)/f(\mathrm{Hg})^+ \simeq 9.4 \times 10^{-15}$ for mercury ion and $\Delta f(\mathrm{Ca})/f(\mathrm{Ca}) \simeq 5.7 \times 10^{-14}$ for calcium. Further improvements were made to this experimental setup and an absolute frequency measurement for mercury ion was reported in the year 2006, where $f(\mathrm{Hg}^+) = 1,064,721,609,899,144.94(97)$. This implies a fractional frequency uncertainity of 9.1×10^{-16}. This measurement represents the most accurate absolute measurement of an optical frequency to date. Ever since the development of femtosecond comb lasers, several laboratories have reported absolute frequency measurements of various other neutral atoms (such as, I_2, Rb) and ions including In^+, Sr^+, Yb^+. Taking into account rapid developments in the field of frequency metrology, it is quite clear that highly stable and accurate optical clocks will soon outperform Cs clocks.

3.4 Other Experiments

The basics of some of the experiments that are being performed using Ultrastable lasers are described in this chapter. Apart from the experiments described here, there are several other experiments (such as, measuring quantum fluctuations of space and time [96], tests of general relativity [32, 33, 48, 97] that have been performed using ultrastable laser cavities. The explanation of all these experiments is beyond the scope of this thesis.

Chapter 4

Experimental Design

4.1 Introduction

The main aim of the experiments described in this thesis is to develop lasers with frequency stabilities of few parts in 10^{15} or less measured over a few seconds. This is achieved by locking the laser's frequency to a resonance of a high finesse, Fabry-Perot cavity using the Pound-Drever-Hall frequency stabilization scheme. It is not possible to get a direct measure of the frequency stability of such highly stable laser systems. However, an estimate of the frequency stability can be obtained by building two identical cavity locked laser systems and measuring their relative stability. Careful experimental design is necessary to construct such a system. The main points that need to be considered are:

- selection of a laser system (whose frequency has to be stabilized), that is well suited to this application
- construction of a high-finesse Fabry-Perot cavity and its temperature control
- realization and optimization of the Pound-Drever-Hall lock
- a method for characterizing the frequency stability of the system

The overall performance of a cavity stabilized laser system is determined by noise associated with the cavity (see chapter 2). Fabry-Perot cavity design is therefore crucial to the design of a cavity stabilized laser system. The experiments described in this thesis have been performed using sapphire and ULE (ultra-low expansivity) glass cavities. In each case, two identical PDH

locked systems have been developed and a radio-frequency beat note is obtained by overlapping picked-off portions of each of the two cavity-locked laser beams on an avalanche photodiode. The frequency of this rf beat note is then counted electronically to obtain a measure of the relative frequency stability of the lasers. Since the two laser systems are identical, the absolute frequency stability of an individual system can be derived by dividing the relative stability by factor of $\sqrt{2}$. This chapter deals with the experimental set-up and design of the two types of cavity stabilized laser systems developed at the National Physical Laboratory, UK.

Figures 4.1 and 4.2 show the setups for the sapphire experiment and the ULE experiment respectively.

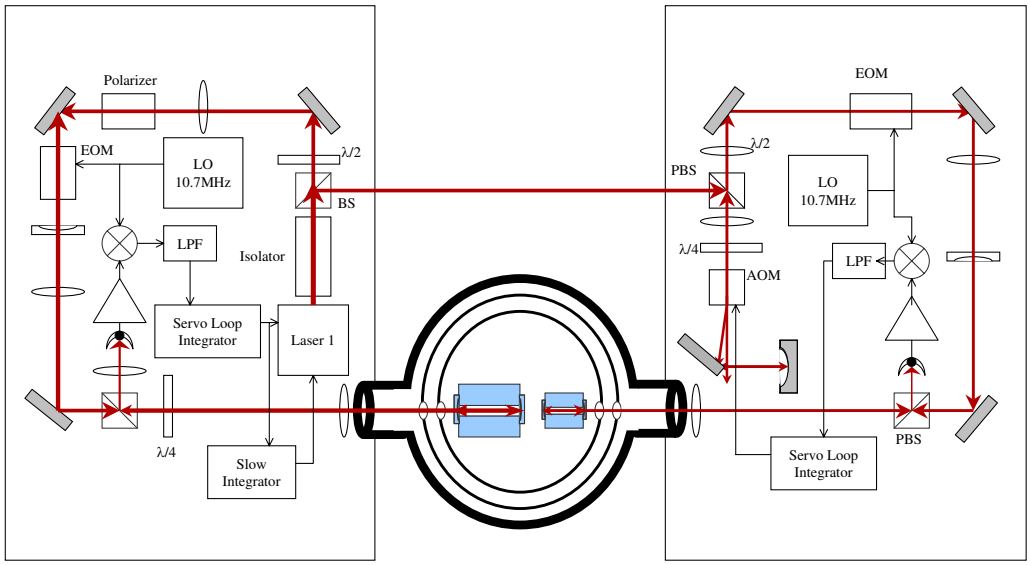

Figure 4.1: Experimental setup for the sapphire cavities. Abbreviations used: AOM - Acousto-optic modulator, BS - beam splitter, EOM - Electro-optic modulator, LO - local oscillator, LPF - low pass filter and PBS - polarizing beam splitter

4.2 The Laser

The laser whose frequency is being stabilized in these experiments is a 1064nm, diode-pumped, NPRO (non planar ring oscillator) type Nd:YAG laser manufactured by Innolight (Mephisto 1200 NE). The choice is based on the fact that NPRO type Nd:YAG lasers are the most-stable commercially available

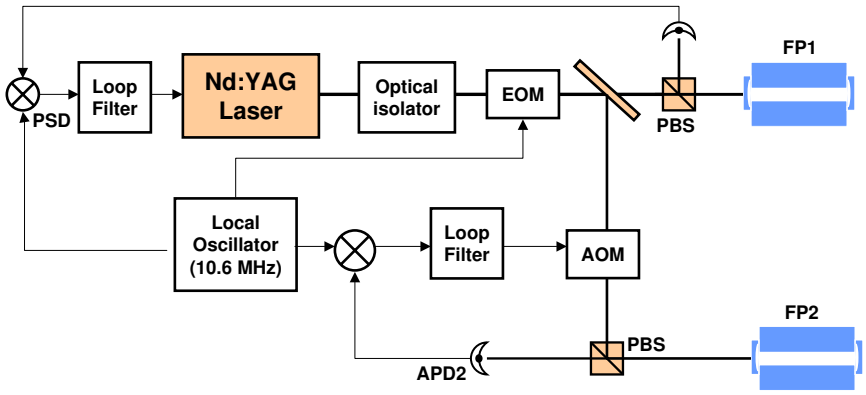

Figure 4.2: Experimental setup for the ULE cavities. Abbreviations used: AOM - Acousto-optic modulator, APD - avalanche photo-diode, EOM - Electro-optic modulator, FP1 - Fabry-perot cavity 1, FP2 - Fabry-perot cavity 2, PBS - polarizing beam splitter and PSD - phase sensitive detection

laser systems in terms of frequency. The free running stability of a Mephisto 1200 NE, as measured by tracking its lineprofile on a spectrum analyzer, is $\sim$ 1kHz in 100 milliseconds [71], which corresponds to a dimensionless frequency stability of $\sim 10^{-12}$ in 100ms. The advantages of using such a system have already been discussed in section 2.6.1.

4.3 Fabry-Perot Cavity

The basics of Fabry Perot cavities have been presented in section 1.5 . In the interest of continuity some of the more important features are recapitulated here. Fabry-Perot cavity consists of a spacer with a bore through its center and two mirrors attached to its ends. Figure 4.3 shows a typical Fabry-Perot cavity.

The equation for the transmission of an ideal Fabry-Perot cavity is given by the Airy function:

$$T = \left[1 + \frac{4R}{(1-R^2)}\sin^2(\frac{\phi}{2})\right]^{-1} \tag{4.1}$$

where T is the transmission, R is the reflectivity and ϕ is the round trip phase change of the light. Figure 4.4 shows the transmission through a Fabry-Perot cavity. The free spectral range (FSR) $\Delta\nu$ is related to the full-width half-maximum (FWHM) $\delta\nu$, of any one transmission band by a quantity known

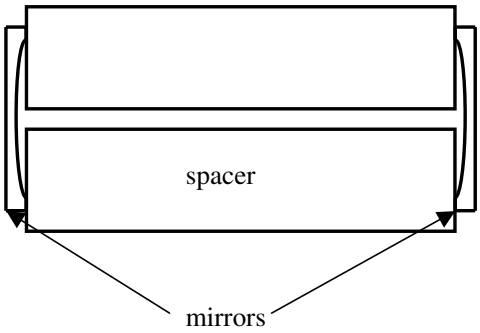

Figure 4.3: A Fabry-Perot cavity

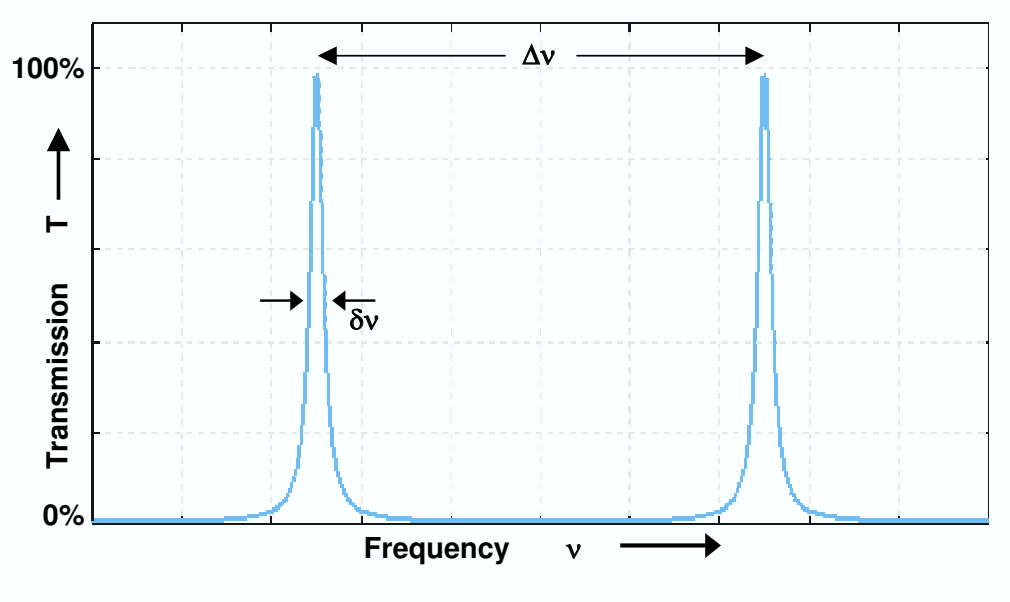

Figure 4.4: Frequency-dependent transmission through a Fabry-Perot cavity with mirror reflectivities of 90% [136]

as the *finesse*:

$$\mathcal{F} = \frac{\Delta\nu}{\delta\nu} \tag{4.2}$$

The resonance frequency ν of a Fabry-Perot cavity is given by the following equation:

$$\nu = \frac{nc}{2L} \tag{4.3}$$

where n is an integer, c is the speed of light and L is the length of the cavity. If we consider speed of light c to be a constant, resonances of a Fabry-Perot cavity are defined by its length. Any change in length of the cavity translates to a change in the resonance frequency and hence affects the stability of the system as a whole. Environmental fluctuations (such as, pressure, temperature and vibrations) perturb the length of the cavity which in turn lead to perturbations in the resonance frequency. A careful design of the cavity is therefore essential to minimize the effects of environmental perturbations to its length and hence the resonance frequency to provide an extremely stable reference for frequency stabilization. Cavity design thus forms an integral part of the Pound-Drever-Hall frequency stabilization scheme.

Environmental temperature fluctuations are related to the fluctuations in length of the cavity by a factor α equal to the thermal expansion coefficient of the material used for construction of the cavity. The effects of temperature fluctuations can thus be reduced by constructing the cavity from a material that has an extremely low thermal expansion coefficient. The two main types of material that have been used for construction of ultrastable cavities in experiments described in this thesis are: ULE (Ultra Low Expansivity) glass at or near room temperature and mono-crystalline sapphire at 4K. ULE glass has a thermal expansion coefficient of $\sim (0 \pm 30) \times 10^{-9}$ K^{-1} near room temperature. However, it suffers from isothermal creep due to the relaxation effects present in amorphous solids. This creep limits the long-term stability that can be achieved by ULE cavities. Sapphire being a covalently-bonded crystal has no isothermal creep, but has a thermal expansion coefficient of $\sim 8.4 \times 10^{-6}$ K^{-1} near room temperature. However, Debye theory states that thermal expansion coefficient, α of any crystal follows a T^3 law.

$$\alpha \propto T^3 \tag{4.4}$$

Sapphire thus has an extremely low thermal expansion coefficient of $\sim 2.05 \times 10^{-11}$ K^{-1} at 4K, which makes it suitable for construction of ultrastable cavities. A comparison of properties of ULE glass with mono-crystalline sapphire is given in Table 4.1.

Apart from choosing the material with an extremely low thermal expansion coefficient, the length of the cavity is kept constant by providing

Properties	**Sapphire**	**ULE Glass**
Thermal Expansion coefficient	$\sim 2.05 \times 10^{-12}\mathrm{K}^{-1}$ at 4K	$\sim (0 \pm 30) \times 10^{-9}\mathrm{K}^{-1}$ near room temperature
Operating temperature	Cryogenic 4K $\Longrightarrow$ Increased vibration noise.	Room temperature $\Longrightarrow$ Active and Passive isolation can be used.
Solid-state properties	Covalently bonded crystal, no ageing effects: creep free.	Amorphous solid. Ages or creeps with time.
Temperature control	High thermal diffusivity at 4K: fast temperature control required.	Slower temperature control required: Better isolation.

Table 4.1: Comparison of Sapphire with ULE

an active temperature control, reducing the vibration sensitivity of the cavity and maintaining an extremely low pressure across the spacer hole in the cavity such that change in refractive index of the cavity is minimized. To provide an efficient temperature control it is necessary to maintain a uniform thermal expansion coefficient throughout the length of the cavity. This is obtained by constructing the mirrors and spacers used for the cavities from the same material and optically contacting the mirrors to the spacer. Optical contacting is a process by which two surfaces are adhered together through molecular attraction without the use of an adhesive. The contacting surfaces of the spacer and the mirrors are polished to be extremely flat and cleaned to an exceptionally high degree. These surfaces are then brought together in a clean environment and they stick to each other forming a single block. A detailed explanation of the cleaning process is given in section 4.5.1.

It is also worth pointing out at this stage that high purity, mono-crystalline sapphire at liquid-He temperatures (4.2K) has a low dielectric loss (and thus exhibits a high Quality-factor[1]) at microwave frequencies. It is therefore suitable to be used as a dielectric cylindrical block (known as a *puck*) which can support whispering gallery modes in microwave resonators. In our experiment, the optical and microwave cavity are made from the same piece of

[1]The Quality-factor, Q of a resonant cavity is defined as the resonance frequency (center-frequency) f_0 divided by the bandwidth Δf:

$$Q = \frac{f_0}{\Delta f} \tag{4.5}$$

where, bandwidth $\Delta f = f_2 - f_1$, where f_2 is the upper and f_1 the lower cutoff frequency.

cryogenic sapphire. This unique feature can enable us to measure correlations between optical and microwave frequencies with an accuracy of 10^{-15} or more. Originally, this experiment was designed such that a direct comparison between the optical and microwave frequencies can be realized. However, this idea has since become obsolete with the advent of *optical frequency comb* (referred in section 3.3). The design and construction of all-sapphire Fabry-Perot cavities is discussed in the following section.

4.4 Cavity Setup

As mentioned in section 4.1, two identical frequency stabilized laser systems are required to get an independent estimate for the upper-bound of the frequency stability of an individual laser system. It is therefore necessary to design two similar cavities in each case: sapphire and ULE (Ultra Low expansivity) glass; for estimating the relative and the absolute frequency stability of the lasers.

4.5 The all-sapphire Fabry-Perot cavities

Figure 4.5 shows a picture of an all-sapphire Fabry-Perot cavity. Its construction, mounting and temperature control are discussed below.

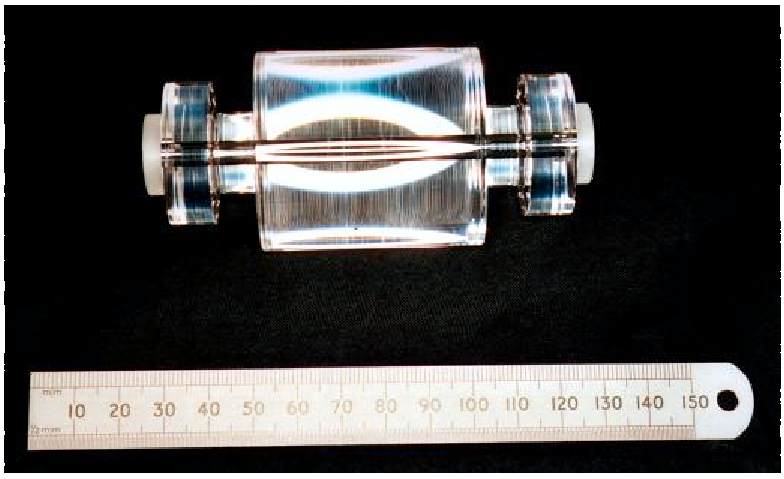

Figure 4.5: Picture of the 90mm long sapphire cavity.

4.5.1 Construction

The sapphire used for construction of the all-sapphire Fabry-Perot cavities employed in our experiment is purchased from Crystal Systems Inc (Salem, Massachusetts). The spacers are made of HEMLUX grade sapphire and the mirrors from HEMEX grade. The two Fabry-Perot cavities used in this experiment are of slightly different length (90mm and 70mm) to ensure that TEM_{00} longitudinal modes supported by each optical cavity can always be found such that the beat frequency lies within the range (300MHz) of an SRS 620 counter. The spacer for the 90mm long cavity has a diameter of 48mm with a 3.4mm diameter bore drilled through its centre. For the 70mm long cavity, the spacer is 20mm in diameter with a 3mm bore through its center. The machining and polishing of the spacer and blanks for mirrors was done by Agate Products Ltd. (Chessington, UK). The HEMEX grade sapphire mirror substrates, 20mm in diameter, were polished and converted into concave mirrors with radii of curvature 150mm and 75mm for the big and small cavity, respectively, by Research Electro Optics (Boulder, Colorado). The mirrors have a flat contacting annulus $\sim$ 5mm for optically contacting them to the spacer. The mirrors are coated with super-mirror dielectric coating for 1064nm on the concave side (reflectivity, $R > 99.99\%$) and AR coating on the other. They are slightly-wedged (20 fringes of a He-Ne laser $\sim$ 1minute angle) to prevent etalon effects caused by reflection of light from the flat surfaces of the mirror back to the laser cavity. The typical properties of the sapphire mirrors used in this experiment are compiled in Table 4.2.

Substrate	HEMEX grade sapphire
Mirror Geometry	Plano-Concave. Plane side: AR coated (1064 nm). Concave side: Super mirror coated ($R > 99.99\%$). Radius of curvature: 150mm and 75mm. Diameter: 15mm with 2.5mm contacting annulus. Thickness: 5mm. Plane surface slightly wedged $\sim$ 1minute angle.
Flatness	$\sim$ 0.13 wave @ 633 nm.
Surface Roughness	< 1.2Å

Table 4.2: Properties of Sapphire mirrors

The concave sides of the mirrors are cleaned extremely carefully using distol type iso-propyl alcohol such that the no harm is done to the super-mirror coating. This ensures that a minimal residue is left on the windows after the alcohol dries. The following procedure was used to clean the sapphire spacer:

Step 1: The sapphire spacer was put in an ultrasonic bath filled with a 20:80 solution of Decon-90 and hot water. Time: 20 mins.

Step 2: The spacer was then taken out of the solution and washed with running hot water and put in an ultrasonic bath filled with deionized water. Time: 20 mins. (N.B.: Powderless gloves are worn at all times during the cleaning process.)

Step 3: After removing the spacer from the deionized water, it was put in an ultrasonic bath filled with distol type isopropyl alcohol. Time: 20 mins.

Step 4: Step 3 was repeated with fresh distol type isopropyl alcohol. Time: 20 mins

Step 5: Finally, the spacer was left for drying on a heater in a dust free environment. Time: 2 hours.

The all-sapphire Fabry-Perot cavities are then formed by optically contacting sapphire mirrors to the spacers on either end. This operation was carried out in a clean room at Imperial College London by Dr. Mark Oxborrow with assistance from myself.

The bigger of the two cavities is enclosed within a microwave enclosure such that a whispering gallery mode can be excited around the circumference of the sapphire. This can then be used to measure correlation between optical and microwave frequencies. It is important to point out that sapphire is an anisotropic crystal and therefore its physical properties are not the same in all directions. However, the physical properties (such as, dielectric constant, thermal expansion coefficient, etc.) are symmetrical along the C-axis of the sapphire. The optic axis of the cavity is therefore aligned with the C-axis of the sapphire to within 2.5 arc-minutes to ensure a uniform dielectric constant across the circumference of the sapphire.

The two all-sapphire optical cavities are mounted horizontally inside the same dual-bath, liquid-He cryostat and their respective temperatures are actively (electronically) controlled. The design of the cryostat and the temperature control loop are discussed in the following sections.

4.5.2 The optical cryostat

Figure 4.6 shows the schematic of the optical cryostat used for this experiment.

The cryostat comprises an outer vacuum chamber, a liquid-nitrogen jacket and two liquid-helium cans; the liquid-nitrogen and two helium reservoirs

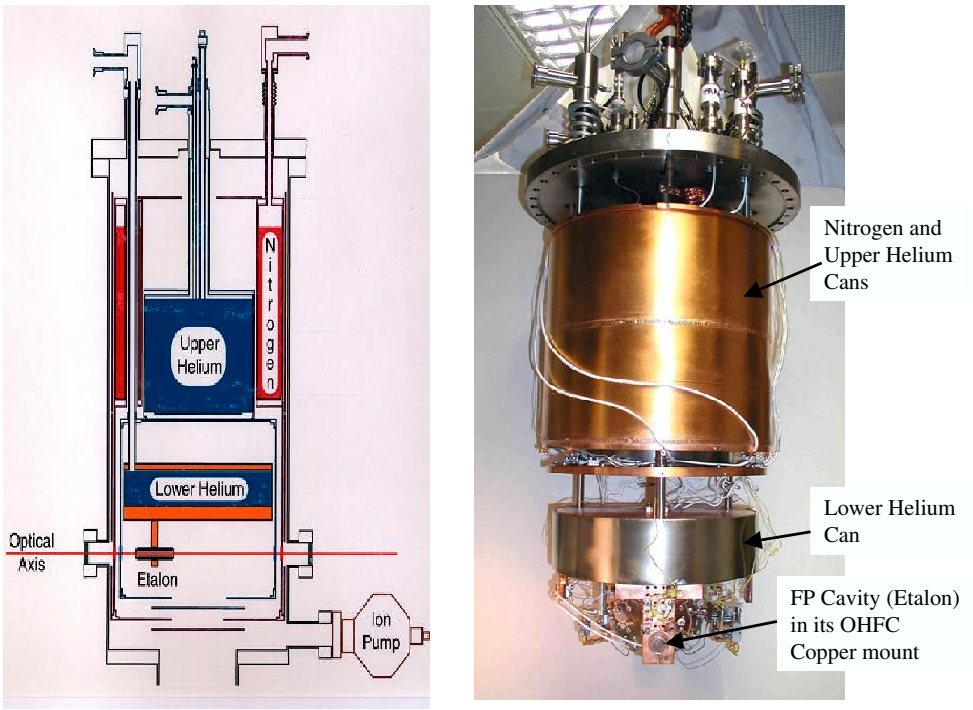

Figure 4.6: The optical cryostat. (a) Schematic of the optical cryostat showing the Nitrogen, two (upper and lower) helium cans and the optical axis. (b) Picture of the wired-up cryostat without the outer jackets.

have capacities of 11, 6 and 3.5 litres respectively. The smaller helium can is nested inside the radiation shield of the larger, upper helium can. Each optical cavity and its supporting OFHC copper structure(s) is thermally anchored (weakly) to the inner helium can's 'cold face' through copper-Niobium straps of designed thickness and length. Designing of copper-Nb straps is discussed in detail in section 4.5.5. Including the cryostat's outer vacuum chamber, there are three radiation shields, each holding four optical windows. Figure 4.7 shows a schematic of the optical routing within the cryostat.

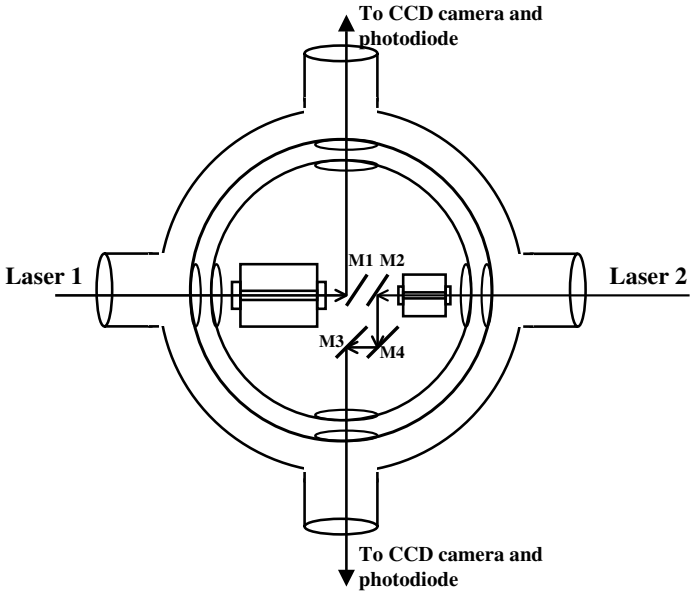

Figure 4.7: Bottom-view of the four-port optical cryostat. M1, M2, M3 and M4 are the mirrors used to steer the laser beam into the two orthogonal ports.

The design of the cryostat is such that the inner liquid-He can is well isolated from the outer environment. It thus stays cold for longer time periods (typically 7 days), compared to outer liquid He can and the liquid nitrogen jacket that have refilling times of 2 days and 17 hours, respectively.

4.5.3 Cryogenic temperature control

Ideally the two laser systems would be locked to cavities held in two different cryostats in different locations. Housing the cavities in the same cryostat is therefore a compromise since it would lead to undetectable 'common mode' fluctuations in the laser frequencies. In an attempt to reduce the level of 'common mode' fluctuations genuine measure of frequency stability of a

laser system is obtained by controlling the temperature of each of the sapphire cavities independently. Figure 4.8 shows the schematic diagram of the temperature controller used for the cavities.

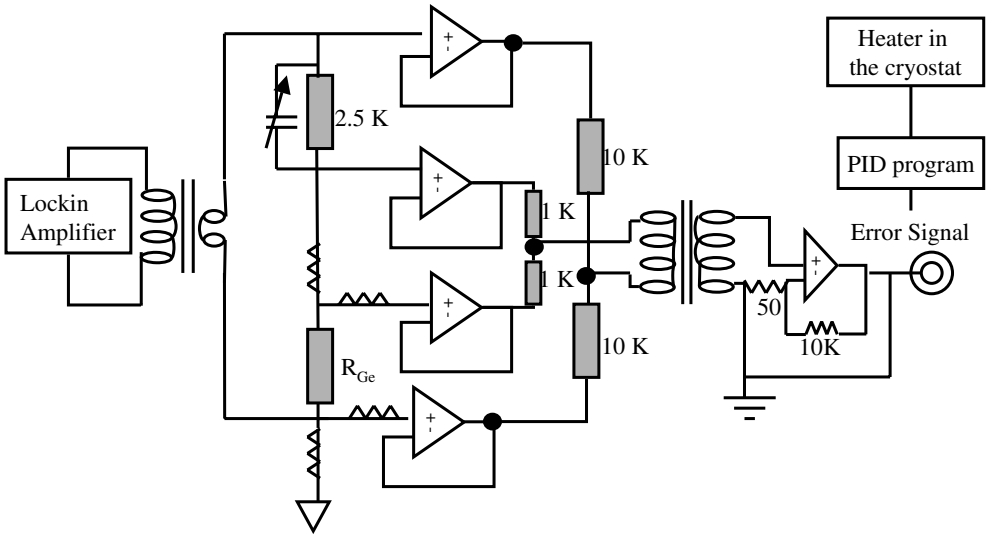

Figure 4.8: Schematic of the temperature controller used for controlling the temperature of sapphire cavities.

The temperature deviation is measured using a modified Ekin and Wagner [102] type four-wire ac-bridge circuit (shown in Figure 4.9) wired to a germanium thermistor (Lakeshore GR-200A-2500) mounted on the copper structure that supports the cavity inside the cryostat. A four-wire measurement scheme is used to avoid uncertainties in the temperature measurement associated with the lead resistances that connect thermistors to the bridge circuits. Lakeshore Quad-Twist^{TM} Cryogenic Wire QT-36 has been used for connecting the RTDs to the bridge circuit. An EG&G 7260 lock-in amplifier supplies an ac drive voltage to the bridge circuit and measures the amplitude of the synchronous error voltage returning from it. This error voltage is a direct measure of temperature deviation from the bridge's setpoint. A PID control program written in LabVIEW reads the error signal from the lock-in amplifier via a GPIB link. This program also sends instructions (again via GPIB) to a programmable current source that controls the power dissipated by a resistance heater mounted on the same copper structure that supports the cavity, thus closing the temperature control loop.

The Ekin and Wagner (EW) [101] design comprises the features of a Kelvin bridge, low-frequency ac operation and the use of voltage followers

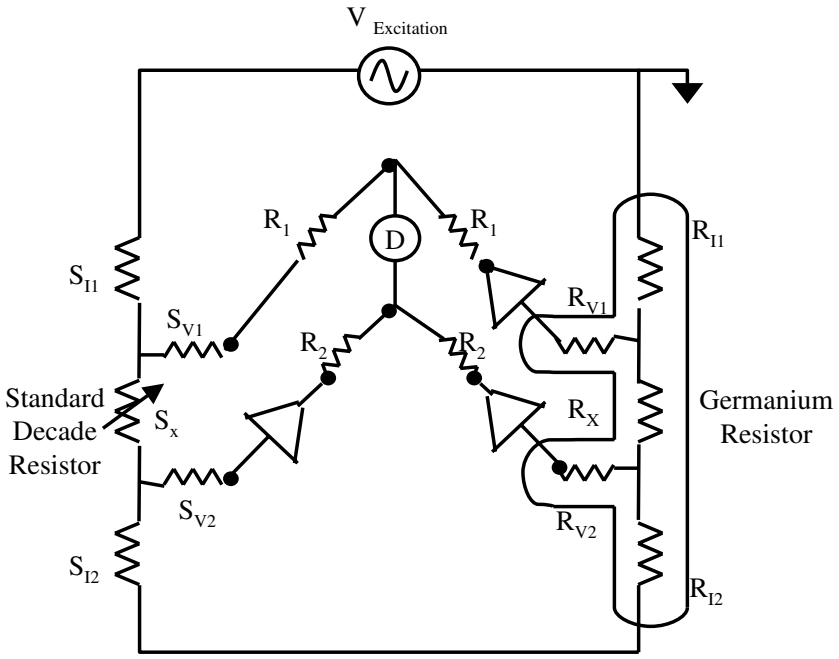

Figure 4.9: Schematic of the Ekin-Wagner bridge [102]. $V_{Excitation}$ is the excitation voltage, S_x is the standard decade resistor, S_{I1} and S_I2 are resistances is the current arm of S_x, S_{V1} and S_{V2} are resistances in the voltage arm of S_x, R_x is the Germanium resistor, R_{I1} and R_{I2} are resistances is the current arm of R_x, R_{V1} and R_{V2} are resistances in the voltage arm of R_x and D is the discriminant of the Ekin-Wagner bridge.

to avoid overloading. In Figure 4.9, R_I and S_I are the extraneous current lead resistances, R_V and S_V are the potential lead resistances associated with the unknown resistor R_x and standard resistor S_x respectively. This configuration ensures that the accuracy of the bridge primarily depends on the accuracy of the standard decade resistor, as described by Rubin and Golahny [102]. The variable capacitance C_1 is added in parallel to compensate for the capacitance of the 1m long Lakeshore Quad-Twist^{TM} Wires QT-36 that connect the Germanium thermistors to the bridge circuit. These wires are carefully heat sunk to the cryostat at various points using OFHC copper cylindrical heat sink blocks to avoid perturbations in the lead resistance.

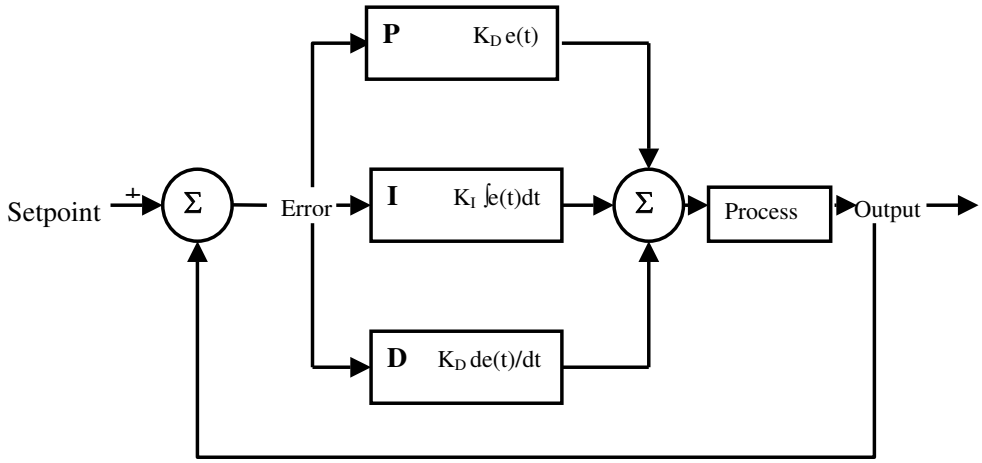

Figure 4.10: Schematic of a PID controller. Proportional, Integral and Differential gain of a PID circuit are denoted by P, I and D, respectively.

Figure 4.10 shows a schematic of a PID control loop. The output, $O(t)$ of a PID control loop is given by equation 4.6.

$$O(t) = G_P + G_I + G_D \tag{4.6}$$

In equation 4.6, G_P is the proportional gain, G_I is the Integral gain and G_D is the Differential gain. These gains are given by the following equations.

$$G_P = K_P e(t) \tag{4.7}$$

$$G_I = K_I \int e(t)dt \tag{4.8}$$

$$G_D = K_D \frac{de(t)}{dt} \tag{4.9}$$

where e(t) = Setpoint - Measurement(t) is the error signal, and K_P, K_I, K_D are constants that are used to tune the PID control loop. Hence equation 4.6 can be written as

$$O(t) = K_P e(t) + K_I \int e(t)dt + K_D \frac{de(t)}{dt} \tag{4.10}$$

The Ziegler-Nichols [103] algorithm is used for the optimization of temperature control loop. The steps involved in optimization of control using Ziegler-Nichols algorithm are given below:

Step 1: Firstly, the integral and derivative action of the controller is disabled by setting the derivative gain, K_D and integral gain, K_I of the temperature control loop to zero.

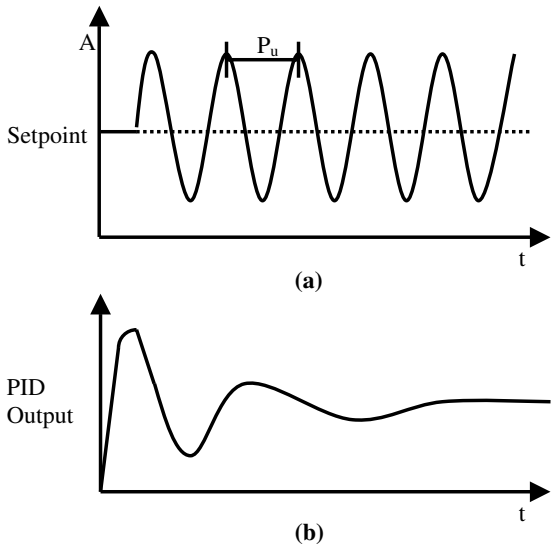

Figure 4.11: Ziegler-Nichols PID tuning algorithm. (a) Amplitude of the Error signal with respect to time with Integral and Derivative gain set to zero ($K_I = K_D = 0$) and proportional gain increased in order to achieve oscillation ($K_P = K_u$) and P_u denotes the oscillation period. (b) A perfectly tuned error signal obtained by setting the proportional gain, $K_P = 0.6K_u$, the integral gain $K_I = K_P P_u/2$, the derivative gain $K_D = K_P P_u/8$, integral time period $P_I = P_u/2$ and differential time periods $P_D = P_u/8$.

Step 2: The proportional gain, K_P is then increased such that the temperature controller starts oscillating. A measurement of the proportional gain settings K_u and the oscillation period P_u is then recorded (refer to figure 4.11).

Step 3: According to Ziegler-Nichols algorithm, the perfect tuning is then obtained by setting the proportional gain $K_P = 0.6K_u$, the integral gain $K_I = K_P P_u/2$, the derivative gain $K_D = K_P P_u/8$, integral time period $P_I = P_u/2$ and differential time periods $P_D = P_u/8$.

There are two germanium resistors (Lakeshore GR-200A-2500) mounted on each copper support that holds the cavity; one is used for controlling the temperature while the other is used for monitoring it. The resistance of the latter was measured using a digital multimeter; when the temperature control was working and Ziegler-Nichols optimized at 4.2K, the multimeter's reading fluctuated in the fourth significant decimal place every few seconds, corresponding to a temperature stability of $\sim 2\mu$K at 4.2K; the bandwidth of the PID control loop was about 1Hz. Figure 4.12 shows the plot of error signal while temperature controlled at 4.2K.

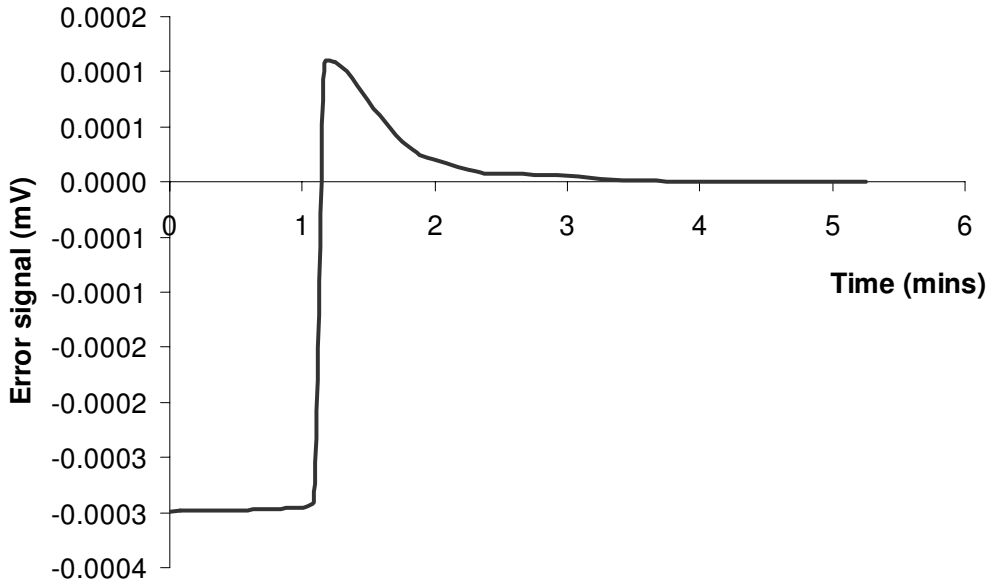

Figure 4.12: Ziegler-Nichols optimized error signal: Error signal with respect to time curve.

An additional level of temperature control is designed for the bigger of the two cavities by controlling the frequency of a high-order whispering gallery mode across the circumference of the sapphire. This microwave based temperature control has been discussed in the next section.

4.5.4 Whispering Gallery Mode and temperature control

The bigger of the two cavities (90 cm in length) is designed to have an additional level of temperature control provided by controlling the frequency of a high-order whispering-gallery mode across the circumference of the sapphire. Figure 4.13 shows the cavity inside its copper enclosure with one of its microwave ports shown in the cross-section.

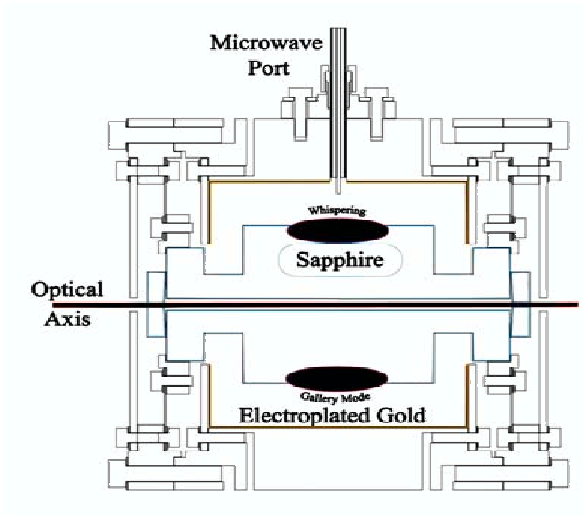

Cavity inside its copper enclosure with one of its microwave ports shown in the cross-section

Picture of the cavity inside the microwave enclosure

Figure 4.13: Sapphire cavity inside the Microwave Can

The term whispering-gallery mode (WGM) describes the electromagnetic wave that circulates around the inner surface of a dielectric sphere or cylinder as a result of total internal reflection [105]. The wavelength of this whispering gallery mode is given by equation 4.11.

$$n\lambda = \pi d\sqrt{\epsilon\mu} \tag{4.11}$$

where n is an integer, d is the diameter of the crystal, ϵ the relative permittivity and μ relative permeability. Figure 4.14 shows the trajectory of a whispering gallery mode. Due to total internal reflection the Q factors of WG-resonators are only limited by the losses in the dielectric. Using sap-

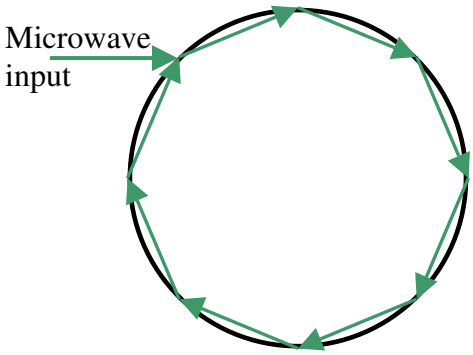

Figure 4.14: Trajectory of a Whispering Gallery Mode: WGM travels across the circumference of the dielectric.

phire at cryogenic temperatures extremely high quality factors $> 10^7$ can be achieved around 10 GHz.

In our experiment, the existence of a microwave whispering-gallery mode was with a line-width of just 81 Hz at a frequency of 9.236 GHz, corresponding to a Q-value of 114 million has been observed at near 4.2K. The change in frequency of this whispering gallery mode can be measured with respect to Cs Microwave frequency standard and fed back through a PID control loop to a resistance heater attached to the cavity mount, providing an additional level of temperature control. This cavity therefore acts as a microwave frequency reference can then be used to measure correlation between optical and microwave frequencies.

4.5.5 Thermal Anchoring of the cavities

In the initial design, thermal anchoring of the cavities was done using copper straps that linked the cold face of the cryostat to OFHC copper supports that hold the cavities (Figure 4.15).

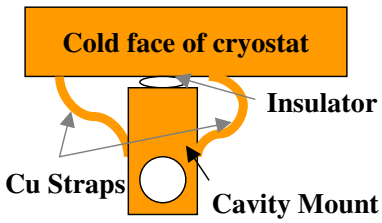

Figure 4.15: Initial design for thermal anchoring of the cavities to the cold face of cryostat. A simple Cu strap is used to connect the cold face of the cryostat to the cavity mount.

A crude analysis of the thermal time constants of our system was performed in the following manner. The rate of heat transfer through a material depends upon the temperature gradient and the thermal conductivity of the material. Power per unit area transported through a material is given by equation 4.12.

$$\frac{Q}{\Delta t} = \frac{\kappa A(T_{hot} - T_{cold})}{L} \tag{4.12}$$

where κ is the thermal conductivity of the material, A is the area, L is the length and Δt is the thermal time constant. In terms of specific heat capacity of the material, Q can be written as follows

$$Q = mc\Delta T \tag{4.13}$$

where m is the mass, c is specific heat capacity and ΔT is the temperature change. From equation 4.12 and 4.13, we get

$$mc = \frac{\kappa A \Delta t}{L} \tag{4.14}$$

Thus, the thermal time constant Δt can be written as

$$\Delta t = \frac{mcL}{\kappa A} \tag{4.15}$$

where L is the length m is the mass, c is the specific heat capacity, κ is the thermal conductivity and A is the area of the material. In the case of four 10 cm long Cu straps, the thermal time constant Δt at room temperature was calculated to be 8 days and 12 hours assuming the following values for copper: thermal conductivity $\kappa_{Cu} = 401$ W/m-K [104] at 300K, specific heat capacity of copper $c_{Cu} = 0.385$ J/g-K [104] at 300 K. However, with the same number of straps at 77K (thermal conductivity $\kappa_{Cu} = 647$ W/m-K [104]), the steady state thermal time constant would be 5 days, 4 hours and 48 mins and at 4K (thermal conductivity $\kappa_{Cu} = 16200$ W/m-K [104]) this time constant would be around 5 hours. With these sort of time constants it would take more than a week for the cavities to reach liquid He temperatures. It was therefore necessary to enhance the thermal anchoring design either by increasing the thickness or the number of the Cu straps used to connect cavity supports to the cold face of the cryostat or design a hybrid strap. The major issue with increasing the number or the thickness of the copper straps was the high thermal conductivity of Cu κ_{Cu} at liquid Helium temperatures. The thermal conductivity of copper increases by a factor of ~ 40 from room temperature to liquid Helium temperature. High thermal conductivity reduces the time constant of the straps drastically at low temperatures and unfortunately it

also leads to heating of the cold face of the cryostat when the temperature controller heats the cavities (to reach a setpoint just above 4K). It was therefore necessary to carefully design some bigger straps to decrease the time constants at high temperatures. The hybrid strap design in our experiment consists of copper straps combined with thicker strips of super-conducting Niobium, as shown in figure 4.16. Although, the thermal conductivity of

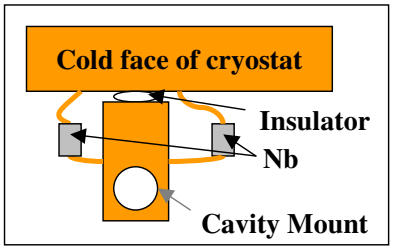

Figure 4.16: Hybrid strap design. A rectangular Nb strip is attached between two copper straps that connect the cold face of the cryostat to the cavity mount.

super-conducting Niobium ($\kappa_{Nb} = 218.97$ W/m-K [104]) is much lower compared to copper ($\kappa_{Cu} = 401$ W/m-K [104]) at room temperature 300K; it increases only by a factor of 2 at liquid-He ($\sim$ 4K) temperatures $\kappa_{Nb} = 436$ W/m-K [104] compared to copper where the thermal conductivity increases by a factor of 40 at liquid-He temperatures ($\kappa_{Cu} = 16200$ W/m-K [104]). This allows us to use thicker straps such that the time constants are lower without compromising on the heat generation at liquid-He temperatures.

In case of hybrid straps, the steady state heat transfer time constant is given by equation 4.16

$$\Delta t = mc(\frac{L_{Cu}}{\kappa_{Cu}A_{Cu}} + \frac{L_{Nb}}{\kappa_{Nb}A_{Nb}}) \tag{4.16}$$

In case of eight 10 cm long Cu straps attached to 2 cm long and 1.5 cm wide niobium straps, thermal time constant Δt at room temperature was calculated to be 1 day and 13 hours and 12 mins, assuming the following thermal conductivity values for copper and niobium: $\kappa_{Cu} = 401$ W/m-K [104] and $\kappa_{Nb} = 218.97$ W/m-K [104] at 300 K , specific heat capacity of Copper $c_{Cu} = 0.385$ J/g-K [104] at 300 K. However, with same number of straps at 77K ($\kappa_{Cu} = 647$ W/m-K [104],$\kappa_{Nb} = 300$ W/m-K), the steady state thermal time constant would be 1 day, 1 hour and at 4K ($\kappa_{Cu} = 16200$ W/m-K [104], $\kappa_{Nb} = 436$ W/m-K) this time constant would be around 30 minutes. Table 4.3 shows the comparison of time constants between two types of straps at different temperatures.

Figure 4.17 shows the cavities mounted inside the cryostat.

Temperature	**Time constant for 4 Cu straps**	**Time constant for 8 hybrid straps**
Room temperature ∼300K	8 days 12 hours	1 day 13 hours and 12 minutes
Liquid N_2 temperature ∼77K	5 days 4 hours and 48 minutes	1 days 1 hour
Liquid He temperature ∼4K	5 hours	30 minutes

Table 4.3: Comparison of the thermal time constants between two types of straps.

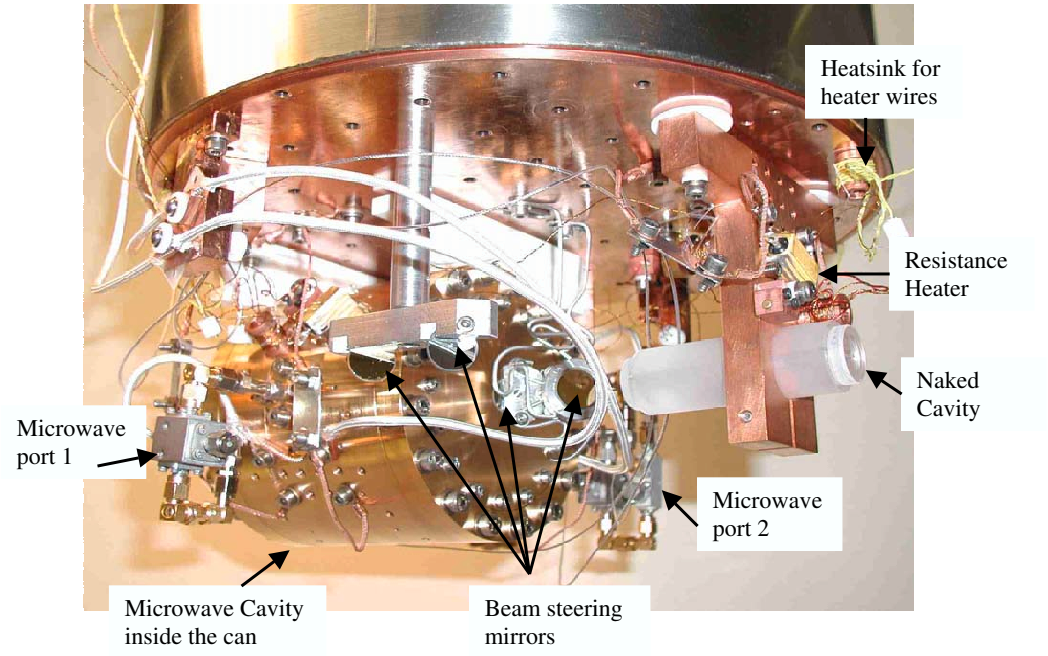

Figure 4.17: Cavities inside the cryostat

Unfortunately the temperature control and the thermal time constants measurements could not be completed due to an ice blockage in the inlet tube of one of the liquid-He cylinders of the cryostat. Further, to our dismay, one of the cavity mirrors became detached from spacer while the cryostat was warming up. This was due to the uneven surface polishing on one end of the spacer. The mirrors and spacer of the broken cavity were then send to USA for repolishing. Given that this seemed likely to cause a significant delay in the experiment, it was decided that I should spend the interim time working on the alternative scheme based on ULE cavities. This experiment had been developed separately and was at that time being run by Stephen Webster.

4.6 Ultra-low expansivity (ULE) glass cavities

Figure 4.18 shows a picture of the ULE cavity. The construction, mounting

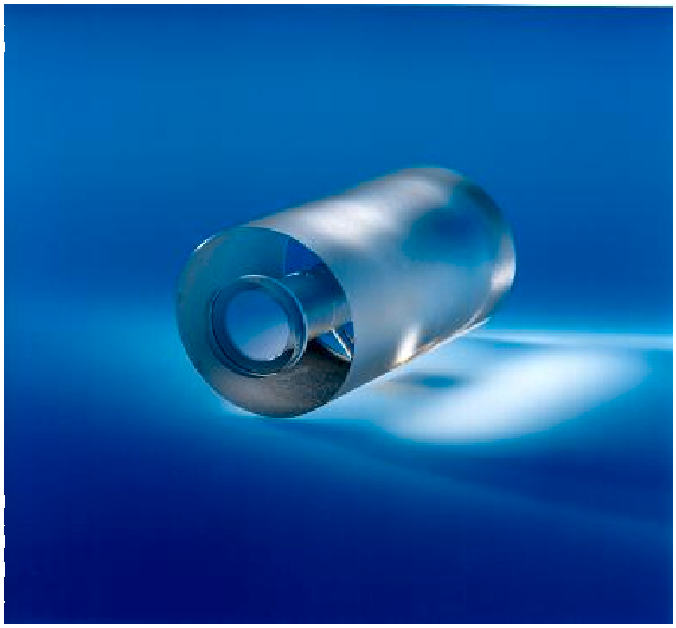

Figure 4.18: Picture of one the ULE cavities used in our experiment.

and temperature control of ULE cavities is described below.

4.6.1 Construction

Corning's ULE glass has been used in the construction of ULE glass cavities employed in our experiment. Ultra Low Expansion Glass is a titanium silicate glass manufactured by flame hydrolysis. This glass is formed as large boules, typically 1.5 meters in diameter by 15 cm thick that can used to make several kind of products [106]. According to Corning's material datasheet [107], ULE's mean coefficient of thermal expansion (CTE) is $0 \pm 30 \times 10^{-9}$/K from 278K to 308K with a 95% confidence level.

The two cavities are formed by optically contacting two highly reflective concave supermirrors (Reflection Coefficient, $R = 0.99998$, radii of curvature = 300mm) polished and coated at Research Electro-Optics, Boulder, Colorado, with a tubular spacer of 100mm length, 60mm outer diameter and 21mm inner diameter in each case. These cavities have a free spectral range of 1.5 GHz, and finesses of $\sim 155,000$ and $\sim 180,000$ derived from the $1/e$ decay time of their resonances [108].

4.6.2 Mounting of ULE cavities

The two ULE Fabry Perot cavities are placed within two temperature controlled evacuated chambers made of aluminium (pressure $< 10^{-7}$ bar maintained using an ion pump). In the vacuum, each of these cavities is supported on three conical diamond styli within an aluminium cylinder to isolate them from any high-frequency vibrations. Base of one of the styli is fixed whereas

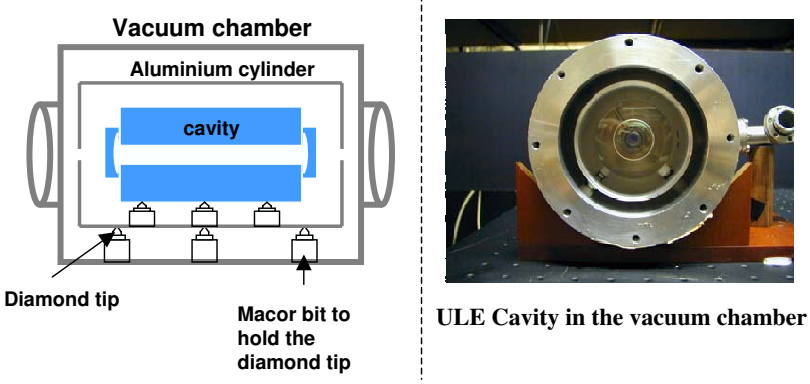

Figure 4.19: ULE cavity inside the vacuum chamber

the other two styli are held semi-rigidly to allow a small amount of movement of the cavities. An extra level of high-frequency vibration isolation is provided by supporting each of these cylinders on three diamond styli inside the two independent temperature controlled vacuum chambers (Figure 4.19).

Apart from the passive vibration isolation provided by placing the cavities on Diamond tips inside the vacuum chamber and an Optical table, we use an active vibration isolation (AVI) system. The active vibration elements used in our experiments are available at www.stabletable.biz. Optical table is placed on the active vibration isolation elements that compensate for any low frequency ground vibration which travel through the cavity by employing a servo feedback control loop. In an AVI system, inertial feedback is used via electromagnetic transducers to provide not only isolation from building vibrations, but also isolation from vibration sources placed on the system itself [112]. Active vibration isolation elements provide isolation that begins at $1-2$ Hz and increase rapidly to 35 db beyond 10 Hz. The lack of any low frequency resonance means much better performance of the cavity stabilized laser systems. The whole apparatus is situated within a double-walled acoustic measurement chamber. The inner room of the chamber is $\approx$ 7m cube with a wall thickness of $\approx$ 0.5m. It rests upon five damped supports and is surrounded by a void of $\approx$ 1m width, which separate it from the outer room. Both the inner and the outer rooms are sealed with massive doors (2.5 and 1.5 tons, respectively). The acoustic noise level within the room is $<$ 25 dBA (in 1/3-octave bandwidths) for frequencies of $>$ 60Hz, 25-40 dBA in the range 10-60 Hz, and 10-25 dBA in the range 210 Hz. The level of vibrations is $\leq 10^{-4}\text{ms}_{rms}^{-2}$ $\text{Hz}^{-1/2}$ in the range 10-100 Hz [108]. This room was not purpose-build for our experiments as originally it was designed to perform acoustic standards measurements.

4.6.3 Temperature Control

Temperature fluctuations in each of the cavities is measured by a thermistor attached to the corresponding vacuum chamber for each cavity using an ac wheatstone bridge. These fluctuations are then fed back through a PID control loop to the heater wire that is wrapped around the outside of the vacuum chambers. Figure 4.20 shows the temperature controller circuit used to control the temperature of ULE cavities. This temperature controller is also optimized using the Ziegler-Nichols algorithm described in section 4.5.3. The temperature of each cavity is controlled at $\simeq$ 301K (just above room temperature) with an accuracy of $< 100\mu$K.

4.7 Pound-Drever-Hall (PDH) locking

The theory of PDH locking technique has been described in detail in section 2.7.3 of this thesis. In both the sapphire and ULE experiments de-

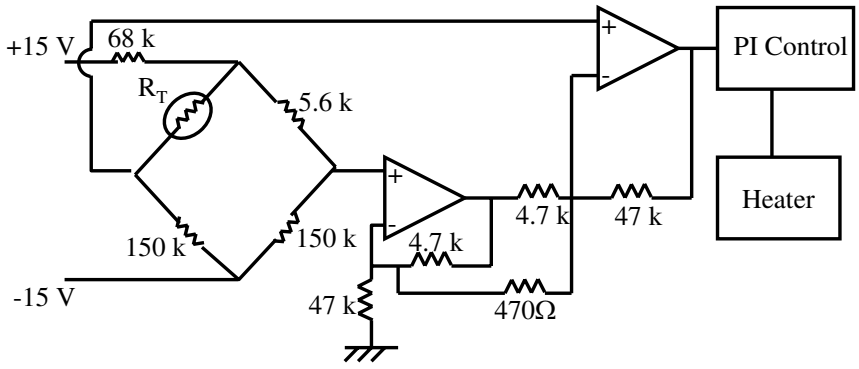

Figure 4.20: Temperature Controller circuit used for the ULE cavities

scribed here, a 1064nm, NPRO (Non-Planar-ring-Oscillator) type ND:YAG laser's frequency is locked using the Pound-Drever-Hall [45] frequency locking scheme to the TEM_{00} mode of a Fabry-Perot (FP) cavity by feedback to a piezoelectric transducer bonded to the laser crystal. A fraction of this laser's output is transferred to the second cavity in the case of the ULE cavities by a polarization-maintaining[2] fiber and using a beam splitter in the case of the sapphire cavities. An offset in frequency between the closest TEM_{00} modes of the two Fabry-Perot cavities $\sim$ 473MHz for the sapphire cavities and $\sim$ 227MHz for the ULE cavities is bridged using acousto-optic modulators (AOMs). Light is locked to the second cavity in each case by feedback to the driver of a double-passed AOM in its input beam path via a voltage-controlled oscillator. In this way, the AOM makes fast frequency corrections to the light without causing deviation to the output beam.

In the PDH locking scheme, the error signal provides a direct measure of fluctuations in the frequency of the laser beam. It is therefore necessary to carefully maximize this signal by ensuring optimum coupling of the laser light into the TEM_{00} mode of the Fabry-Perot cavity. The various steps involved in achieving a good PDH error signal are described in the following sections.

4.7.1 Mode-Matching

In the sapphire experimental setup, light from the 1064nm laser described in section 4.2 is divided into two parts using a 50:50 beam splitter. A part

[2]A polarization-maintaining fiber is an optical fiber in which the polarization planes of light waves launched into the fiber are maintained during propagation with little or no cross-coupling of optical power between the polarization modes.

of this beam is mode-matched[3] to the TEM_{00} mode of the 90 mm long all sapphire Fabry-Perot cavity placed inside the cryostat. The other part of this beam is double-passed through an AOM as shown in figure 4.1 and mode-matched to the smaller 70 mm long cavity also placed in the same cryostat. Mode matching is obtained by modifying the initial laser waist using a combination of concave/convex lenses to match the natural waist of the cavity. The propagation of a Gaussian laser beam through thin lenses was studied using a free Labview based Gaussian Beam Calculator program developed by David Thompson [113].

As mentioned previously, the laser used in the sapphire experiment is a 1064nm NPRO type Nd:YAG laser (Innolight Mephisto 1200 NE). The laser waist is 0.366 mm with a beam divergence θ of 3.8mrad [72]. Beam divergence is the angle at which the beam spreads transversely. This is inversely related to the waist by equation 4.17.

$$\theta = \frac{\lambda}{\omega_0} = \frac{\omega(z)}{z} \tag{4.17}$$

The laser beam waist is then matched to the natural waist of the two Fabry-Perot cavities using two lens (a concave and a convex) configuration to ensure maximum coupling of the beam into TEM_{00} mode of each cavity. The natural waist of the cavity is calculated as if light originates in the resonator and stays there (Figure 4.21) [56]. The beam wavefront at the end of the cavity matches

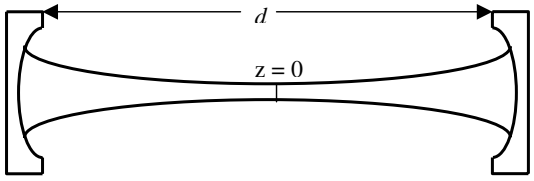

Figure 4.21: Beam propagation inside a Fabry-Perot cavity. d is the distance between the two mirrors of the cavity.

the mirrors' radius of curvature, R and is planar ($z = 0$) at the center of the cavity. The light beam is at its smallest size at the center of the cavity and this position is referred to as the cavity waist. The cavity waist is a function of the mirrors' radius of curvature, R and the mirror separation, d [56]. It can be expressed as:

$$\omega_0^2 = \frac{\lambda}{\pi}\left[\frac{d}{2}\left(R - \frac{d}{2}\right)\right]^{1/2} \tag{4.18}$$

[3]Mode-matching is the process of maximizing the coupling of a free space Gaussian beam into a specific mode (typically TEM_{00}) of an optical device (single mode fiber, Fabry-Perot Resonator etc).

The beam spot size is a function of the distance from the waist to any position on the beam, z. It is expressed as:

$$\omega^2(z,\omega) = {\omega_0}^2 \left[1 + \left(\frac{\lambda(z-z_0)}{\pi {\omega_0}^2}\right)^2\right] \tag{4.19}$$

The Gaussian Beam Calculator program [113] determines the position of two mode-matching lenses ($f = 160$ mm and $f = -160$ mm in the case of the 90 mm long cavity, $f = 250$ mm and $f = -250$ mm in the case of the 70 mm long cavity) that match the laser beam waist to the waist of the two cavities. The natural waists of the 90 mm and 70 mm long cavities employed in our experiment are 0.160 mm and 0.112 mm, respectively. This method is also used in the Ultra Low Expansivity (ULE) cavities experiment, in which the light beam from the 1064 nm non-planar-ring-oscillator (NPRO) type Nd:YAG laser (Model Lightwave-126) is divided into two parts using a beam splitter. A part of this beam is mode-matched to the TEM_{00} one of the ULE cavities and the other part is transferred using a polarization maintaining fiber to mode-match to the TEM_{00} mode of the other cavity. The two ULE cavities used in this experiment were formed using concave mirrors with radius of curvature 300 mm and were of exactly the same length 100 mm. These cavities thus had a natural waist of 0.195 mm. The Lightwave-126 laser employed in this experiment had a waist size of 0.38 mm and Gaussian beam calculator program was used to determine the positioning of the mode-matching lenses.

After the mode-matching lens positions have been determined they are placed in the beam path, the laser frequency is tuned slowly to identify the TEM_{00} mode of the Fabry-Perot cavity. This is achieved using a CCD camera in the beam path of the transmitted light. Figure 4.22 shows the lower order Transverse Electro Magnetic (TEM) modes of a Fabry Perot cavity. The angle of incidence and height of the beam is adjusted to increase the coupling in the TEM_{00} mode of the cavity. Once the TEM_{00} mode is bright enough to saturate the CCD camera, it is replaced by a Photodiode whose output is measured on an Oscilloscope. The transmitted power is maximized further by adjusting the height and angle of incidence of the beam to achieve optimum coupling.

4.7.2 Phase modulation of the laser beam

In the PDH locking scheme, the laser beam that is incident on a Fabry-Perot (FP) cavity is phase modulated and the fluctuations in the laser's frequency are measured by comparing the reflected beam with the modulation signal.

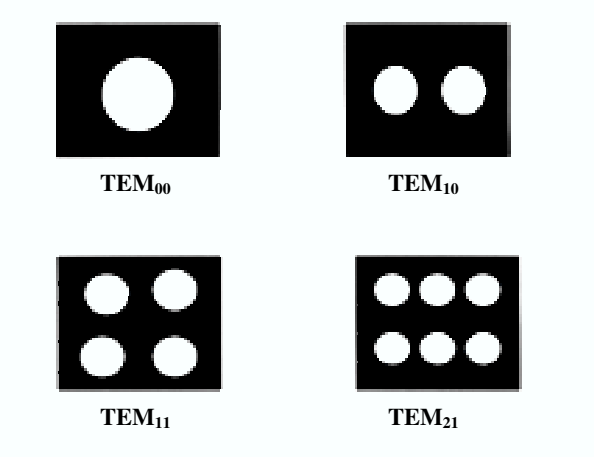

Figure 4.22: Transverse Electro Magnetic (TEM) Modes of a Fabry Perot cavity [114] when the laser frequency is scanned by applying a 5kHz triangular wave.

The laser beam in our experiment is phase modulated at a frequency of 10.6 MHz using the Leysop low voltage electro-optic modulator (Model EM 200L). Electro-optic modulators are built with electro-optic crystals exhibiting the Pockels effect[4]. The transmitted beam is phase modulated with the electric signal applied to the crystal. Let us assume that the electric field of a laser beam with frequency ω leaving the electro-optic modulator (EOM) is given by $Ae^{i\omega t}$. If a sinusoidally varying potential is applied to the EOM with frequency Ω and small amplitude β, a time dependent phase is added to laser beam and can be expressed as:

$$Ae^{i\omega t + i\beta \sin(\Omega t)} \tag{4.20}$$

Since β is small a Taylor expansion can be applied to the exponential:

$$Ae^{i\omega t}(1 + i\beta \sin(\Omega t)) \tag{4.21}$$

Applying the sine identity $\sin(x) = (e^{ix} - e^{-ix})/2i$, equation 4.21 can be written as:

$$Ae^{i\omega t}\left(1 + \frac{\beta}{2}(e^{i\Omega t} - e^{-i\Omega t})\right) = A\left(e^{i\omega t} + \frac{\beta}{2}(e^{i(\omega+\Omega)t} - e^{i(\omega-\Omega)t})\right) \tag{4.22}$$

Equation 4.22 implies that there is the original carrier frequency plus two small sidebands, one at $\omega + \Omega$ and another at $\omega - \Omega$. It is important to

[4]The Pockels effects can also be termed as linear electro-optic effect whereby a change in the refractive index of a crystal to which an electric field is applied is proportional to the electric field.

note that in equation 4.21 only the first term is used in the Taylor series expansion. In principle, an infinite number of sidebands are generated using an EOM. Using Bessel functions, equation 4.20 can be written as

$$Ae^{i\omega t+i\beta\sin(\Omega t)} = Ae^{i\omega t}\left(\sum_{k=0}^{\infty} J_k(\beta)e^{ik\Omega t} + \sum_{k=0}^{\infty}(-1)^k J_k(\beta)e^{-ik\Omega t}\right) \tag{4.23}$$

Equation 4.23 gives the amplitude of all the sidebands. This analysis is essentially the same as described in section 2.7.3. However, it is described again here to keep the continuity.

The impedance of the Leysop low voltage electro-optic modulator (Model EM 200L) used in our experiment needs to be matched to a 50 ohm, 10.6 MHz frequency oscillator. Impedance matching[5] is achieved using an air-core transformer. The air-core transformer is made by using a plastic ring with approximately 5 cm outer diameter and 3.5 cm inner diameter. A 2mm thick copper wire is then wound across the ring to form primary and secondary arms of the transformer. The coupling between the two arms can be adjusted by moving the primary arm towards and away from the secondary. Figure 4.23 shows the schematic of the impedance matching circuit of the Electro-optic modulator (EOM).

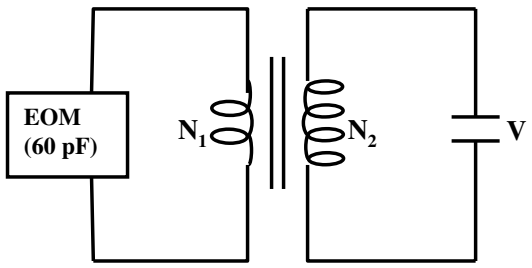

Figure 4.23: Impedance matching circuit of Electro-optic modulator (EOM). V is a crystal voltage source of frequency of 10.6 MHz and 50 ohm internal resistance.

The voltage and current in the primary arm of the transformer V_1 is given by the following equations

$$V_1 = \frac{N_1}{N_2}V_2 \tag{4.24}$$

[5]In electrical engineering, the maximum power (transfer) theorem states that to obtain maximum power from a source with a fixed internal impedance, the impedance of the load must be made the same as that of the source. Impedance matching is the process that attempts to make the output impedance of a source equal to the input impedance of the load to which it is ultimately connected. This ensures that the power transfer is maximized and reflections from the load are minimized

and

$$I_1 = \frac{N_2}{N_1} I_2 \tag{4.25}$$

The effective resistance R' of the load in the primary circuit is given by

$$R' = \frac{V_1}{I_1} = \left(\frac{N_1}{N_2}\right)^2 \frac{V_2}{I_2} \tag{4.26}$$

which can be written as

$$R' = \left(\frac{N_1}{N_2}\right)^2 R \tag{4.27}$$

In our experiment, the effective resistance of the load (EOM) calculated at the oscillation frequency (f = 10.6 MHz) is equal to 250.24 Ω ($X_C = 1/(2\pi f C)$), the resistance of the frequency source R = 50 Ω. According to equation 4.27, the impedance match in our case can be obtained by using a transformer of approximately 1 : 2.24. Rounding the approximate number of turns calculated by equation 4.27 to the nearest integer values the number of turns in the primary circuit was set to 5 and secondary to 11 in case of our air core transfer. Figure 4.24 shows the transmitted signal through the cavity measured using a photodiode when a triangular wave is applied to the PZT (peizo-electric transducer) to sweep laser frequency by few tens of MHz.

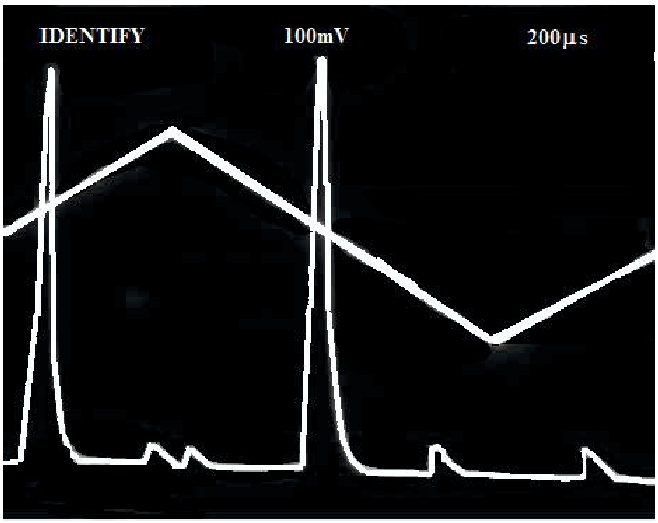

Figure 4.24: Transmitted signal through the Fabry-Perot (FP) cavity with EOM sidebands measured using a photodiode. A sine wave of a few kHz is applied to the PZT attached to the laser crystal. The signal appear asymmetrical due to slow response of the photodiode.

4.7.3 Pound Drever Hall (PDH) error signal

The theory of generation of a PDH error signal has been described in detail in section 2.7.3 of this thesis. Experimentally, after phase modulation of the laser frequency using an EOM, the Pound Drever Hall (PDH) error signal is generated by mixing the reflected beam with the phase modulation frequency of the local oscillator. The reflected beam is picked off using a combination of polarizing beam splitter (PBS) and a $\lambda/4$-plate in the beam path as shown in figure 4.25. A fast photodiode is then used to measure the reflected beam which is amplified and mixed with a part of the RF modulation signal that provides the phase modulation using a radio frequency (RF) mixer. The output of this mixer is then passed through a low-pass filter to generate the PDH error signal. In practice there are unequal phase delays in two signal paths at the input of the mixer: the RF signal used for phase modulation and the sine term measured in reflection using the photodiode at the modulation frequency $\Omega = 10.6$ MHz. The phase delay is compensated using a phase shifter.

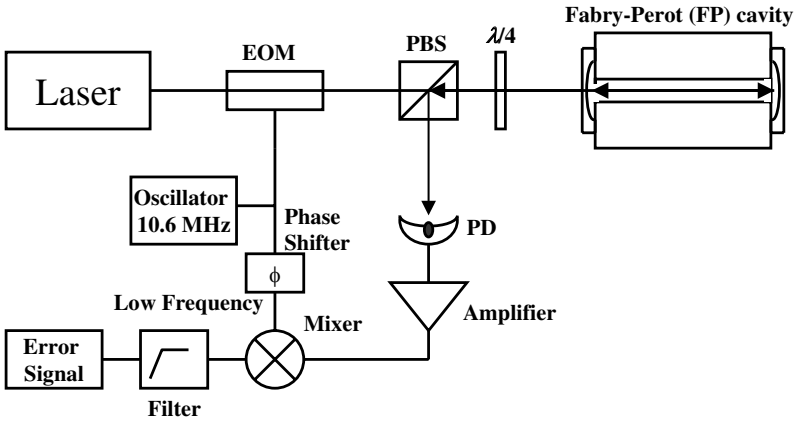

Figure 4.25: Generation of PDH error signal. In this figure, EOM is the electro-optic modulator, PBS is the polarizing beam splitter and PD is the photodiode

Ideally, the dc value of the error signal should remain null. However, residual amplitude modulation (RAM)[6] generated by the phase modulator (EOM) leads to a persistent problem in the PDH locking technique. The detection of this RAM gives a non-zero baseline and therefore the technical noise of the laser is transferred at the detection frequency [100]. The RAM is reduced in our experiment by using a Glan-Taylor Polarizer in the beam path

[6]Residual amplitude modulation is caused by the misalignment of the angles between the incident polarization and the crystallographic axis of the phase modulation crystal

before the EOM that matches the angle between the incident polarization and crystallographic axis of the phase modulator (EOM).

4.7.4 Servo loop

As described in section 2.7.5 of this thesis, the servo in a control loop amplifies the error signal and drives the actuator that compensates for the frequency fluctuations. Figure 4.26 shows the servo circuit used in our experiment. The theory of the loop servo circuit as been described in detail in section 2.7.5 of this thesis. The servo output is then fed back to the PZT (peizo electric

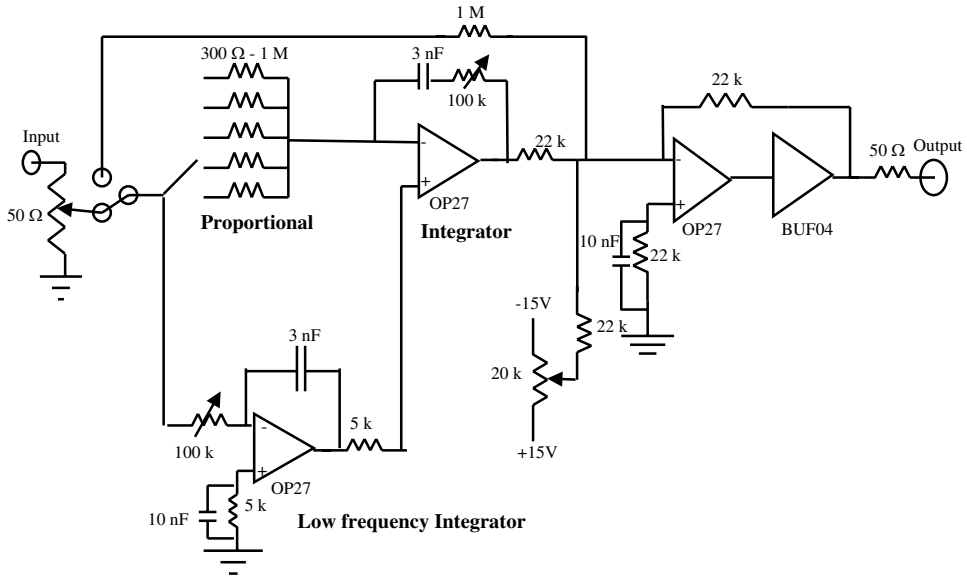

Figure 4.26: Loop filter with bypass topology. It is similar to the circuit presented in figure 2.14 apart from the fact that all the resistance values and type op-amp used are described accurately in this figure.

transducer) that converts the voltage fluctuations to frequency changes in the laser. With the system in lock, the servo gain is optimized by first setting the Integral, low-frequency gain to zero and increasing the proportional gain (R = 300Ω to 1MΩ) until the output of the servo starts to oscillate. The proportional gain is then reduced by a factor of 3 and the integral gain component is adjusted by using 100kΩ potentiometer until the output starts oscillate again. The resistance is set such that the servo output just stops oscillating. Finally, the low frequency integral gain is increase until the servo output starts oscillating. This resistance is again adjusted to keep the servo output just below oscillating. The low frequency integrator has a cut off at

frequency f_1 which corresponds to the cavity linewidth. The bode plot of the integrator is shown in figure 2.16.

4.7.5 Conclusion

This chapter describes in detail the various design aspects of both the sapphire and ULE glass cavities experimental setups. The type of lasers used, cavity design, mounting, temperature control and mode-matching technique has also been explained great detail. It also describes the PDH locking setup including the phase modulation and servo control loop with all the relevant circuit diagrams and components used in our experiment.

Chapter 5

Results

5.1 Introduction

This chapter explains the results obtained in the experiments performed using the two experimental setups (one with sapphire cavities and the other using ULE cavities), both of which have been described in Chapter 4 of this thesis. Initially, the experiments were started using the sapphire cavities, however, due to the breakdown of one of the sapphire cavities while the cryostat warmed up from liquid-He to liquid-N_2 temperature, the experiments could not be continued. This situation was then reviewed at the National Physical Laboratory and Imperial College London and it was decided to send the cavity mirrors and spacer to the United States for repolishing. Even optimistic estimates of the time would take suggested there need a period of approximately six months during which the sapphire experiment would be out of commission. In the mean time, there were some experiments that could be performed using ULE cavities experimental setup at National Physical Laboratory. The decision to switch attention to the ULE experiment proved to be justified as the downtime of the sapphire experiment turned out to be longer than one year. The experimental results obtained using the two setups are described below.

5.2 Finesse measurement - sapphire cavity

As described in the section 2.7.3 of this thesis, power in the reflected signal and hence the sensitivity of the error signal in a Pound Drever Hall locking scheme is directly proportional to the finesse of the Fabry-Perot cavity used in the experiment. It is therefore advantageous to use a cavity with as high finesse as possible. The finesse is a measure of the sharpness of the trans-

mission peaks of a cavity, and is defined as the ratio of FSR[1] (free spectral range) to transmission peak width at half the maximum of the amplitude (often referred to as *full width at half maximum* or FWHM). The finesse of a cavity is a function of mirror reflectivity - the higher the mirror reflectivity, the higher is the finesse of the cavity. The value of finesse is given by the following relation:

$$\mathcal{F} = \frac{FSR}{\Delta\nu_{FWHM}} = \frac{\pi(R_1R_2)^{1/4}}{1-\sqrt{R_1R_2}} \tag{5.1}$$

where R_1 and R_2 are the reflectivity of the two mirrors used in the cavity. The cavity mirrors used in our experiment are thus polished to obtain a reflectivity R > 99.99%. In in a real Fabry-Perot cavity [43, 115], the surface absorption and parallelism affects the finesse. The finesse in such a case can be expressed as :

$$\mathcal{F} = \frac{1}{\frac{1}{{\mathcal{F}_C}^2} + \frac{1}{{\mathcal{F}_P}^2} + \frac{1}{{\mathcal{F}_S}^2} + \frac{1}{{\mathcal{F}_\theta}^2} + \frac{1}{{\mathcal{F}_D}^2}} \tag{5.2}$$

where $\mathcal{F}_C$ is theoretical cavity finesse due to mirrors reflectivity and cavity losses,

$$\mathcal{F}_C = \frac{\pi(R_1R_2)^{1/4}e^{-\alpha L/2}}{1-\sqrt{R_1R_2}e^{-\alpha L/2}} \tag{5.3}$$

$\mathcal{F}_P$ is surface parallelism finesse,

$$\mathcal{F}_P = \frac{\lambda}{\sqrt{3}\beta CA} \tag{5.4}$$

$\mathcal{F}_S$ is plate spherical deviation finesse,

$$\mathcal{F}_S = \frac{M}{2}\frac{\lambda}{633nm} \tag{5.5}$$

$\mathcal{F}_\theta$ is incident beam divergence dependant,

$$\mathcal{F}_\theta = \frac{\lambda}{L\tan^2(\theta)} \tag{5.6}$$

$\mathcal{F}_D$ is diffraction limited finesse,

$$\mathcal{F}_D = \frac{CA^2}{2L\lambda} \tag{5.7}$$

[1]The free spectral range of a Fabry-Perot cavity is the spacing between transmission maximums of the cavity and is a function of the optical path length between the reflectors, given by, $\Delta\nu = c/2L$.

and λ is central wavelength, α is linear cavity loss coefficient (αL) is the round-trip loss, β is tilt angle between surfaces (typically $\sim$ 1 arcsec), CA is etalon clear aperture diameter, L is the distance between mirrors or the cavity length, M is surface flat accuracy in fraction of wavelength (eg., for $\lambda/100$; $M = 100$), θ is incident beam divergence. It is therefore quite difficult to estimate the finesse of a Fabry-Perot cavity theoretically unless all the attributes of equation 5.2 are known accurately.

The finesse of the sapphire cavity employed in our experiment was measured by introducing an AOM (acouto-optic modulator) in the laser beam path and initially locking the frequency shifted beam using the Pound Drever Hall (PDH) locking scheme to the sapphire Fabry-Perot cavity (Figure 5.1). The AOM power is then switched off while the transmitted signal is being

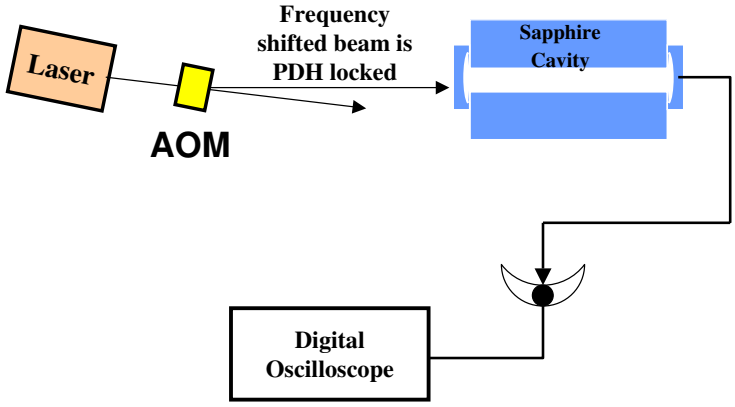

Figure 5.1: Experimental setup for finesse measurement. An acousto-optic modulator (AOM) is used to shift the frequency of the beam before it locked to the cavity. The transmitted signal is measured on a digital oscilloscope after the AOM is switched off.

measured on a digital oscilloscope. After the AOM was switched off, the decay of the transmitted light was recorded with the digital oscilloscope. An exponential decay equation is then fitted to this output using a program written in Mathematica. Figure 5.2 shows the decay time measurement and the equation that fits this measurement.

$$y(t) = 0.37734 \exp(-t/19.97484) + 0.00318 \tag{5.8}$$

Equation 5.8 is the exponential decay of light inside the cavity with a time constant of $\tau_s \approx 19.975\mu$ s. The finesse $\mathcal{F}$ of the cavity is related to the decay time $\tau_s = \mathcal{F}L/c\pi$, which allows us to determine $\mathcal{F}$ to be $\approx 188,260$. This finesse measurement was performed after the cavity mirror and spacer were repolished and optically contacted by Dr. Mark Oxborrow with help from

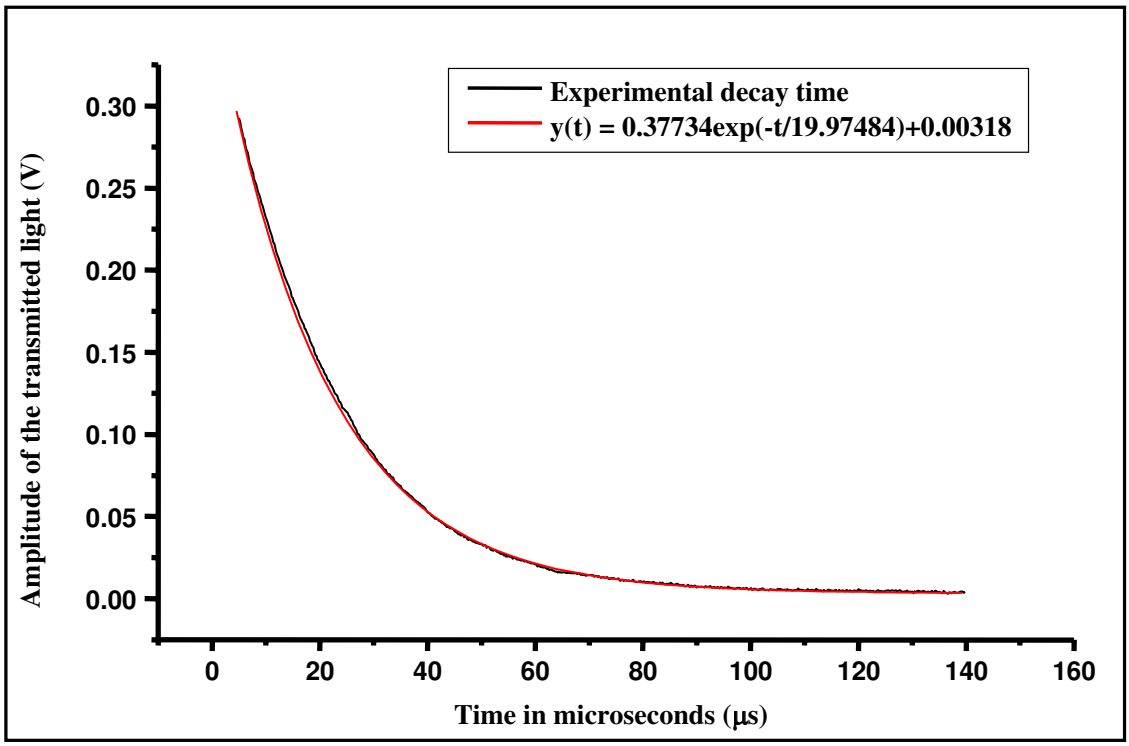

Figure 5.2: Experimental decay time of the cavity.

myself at the clean room in Imperial College London. However, a strange phenomenon was observed when the 1064 nm laser light was incident on the cavity - the maximum fractional power transmitted through the cavity, when the laser light is in resonance and mode-matched to the TEM_{00} mode of the cavity, was observed to be approximately 0.015%. Initially, it was attributed to the patchy coating on sapphire supermirrors. However, a finesse measurement of $\approx 188,260$ implied that the reflectivity was still high. Although this did not make sense there was no other alternative than to remove the optically contacted mirror from one end of the cavity and adjust the position of this mirror such that the transmission through the cavity is maximized when the 1064 nm laser light is in resonance with the TEM_{00} mode of the cavity. Further work was carried out on this experiment by Dr. Mark Oxborrow and is discussed in section 6.2.2 of this thesis.

5.3 Turning Point measurements - ULE cavity

5.3.1 Beat note experiment

As described in the earlier sections of this thesis, optical local oscillators with supreme frequency stability form a key component of optical frequency standards. Development of reliable sub-Hertz linewidth sources plays an important part in the overall development of optical clocks and, given the difficulty in achieving such a goal, it may even be that the ultimate success of the technique rests on this issue. The motivation for the experiments performed in this thesis is to investigate the experimental conditions required to achieve sub-Hertz laser linewidths. The experimental setup for the two systems used at the National Physical Laboratory are described in detail in Chapter 4 of this thesis. As mentioned earlier in section 5.1, the stability measurements could not be performed for the sapphire cavities due to the breakdown of one of the cavities. However, in case of the ULE cavities, it was possible to make significant progress.

The 1064 nm laser's light was stabilized to one of the ULE Fabry-Perot cavity, using the Pound Drever Hall(PDH) locking scheme by feeding back the PDH error signal to the peizo-electric tuning element bonded to the laser crystal. A part of this beam is transferred via optical fibre to the second platform where its frequency is shifted into resonance with a second Fabry-Perot cavity. An offset in frequency between the closest TEM_{00} modes of the two FP cavities of 227 MHz is bridged by an acousto-optic modulator. Light is locked to the second cavity by feedback to a double-passed AOM in

its input beam path via a voltage-controlled oscillator. A relative measure of the stability is then obtained through a heterodyne beat measurement of the two beams, one from the laser and other from the AOM, each locked to its own cavity, by picking off small portions of the two beam and combining them on a photodiode. With light simultaneously locked to both cavities, the heterodyne beat provides a direct measure of the linewidths of relative frequency fluctuations between the two cavity resonances. The beat frequency is amplified, mixed down to 50kHz and input to a fast Fourier transform network analyzer. Typically this beat frequency drifts at a rate of ≈ 0.5 Hz/s owing to residual thermal fluctuations of the cavities that results in changes in their lengths because they are not controlled at zero of thermal expansion. A matching linear sweep is applied to the synthesizer that is used to mix down this beat signal. Figure 5.3 shows the heterodyne beat taken after

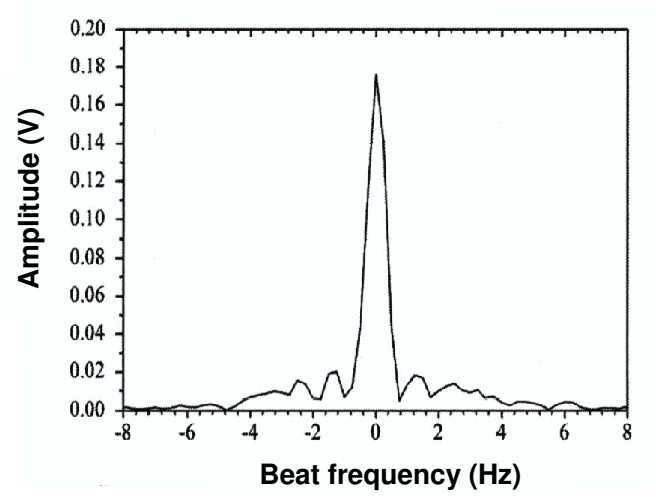

Figure 5.3: Heterodyne beat between light locked to two independent etalons; resolution bandwidth, 0.25 Hz. [108]

drift compensation with a measurement bandwidth of 0.25Hz (4-s integration time). The relative linewidth, after deconvolution of the instrumental bandwidth, is 0.65Hz, from which the absolute linewidth is deduced to be ≈ 0.46Hz. An analysis of the beat frequency variance is also performed using a time-interval counter. Figure 5.4 shows the fractional root Allan-deviation of the beat signal as a function of averaging time. For $\tau \leq 1$ s the deviation is well described by the $\tau^{-1/2}$ law, as is expected for the white frequency noise, apart from a small shoulder near 0.05 s that is due to a small level of residual vibration near 20Hz. For 1s $< \tau \leq$ 20s the deviation exhibits frequency flicker noise and reaches a minimum of 1.3×10^{-15}, corresponding

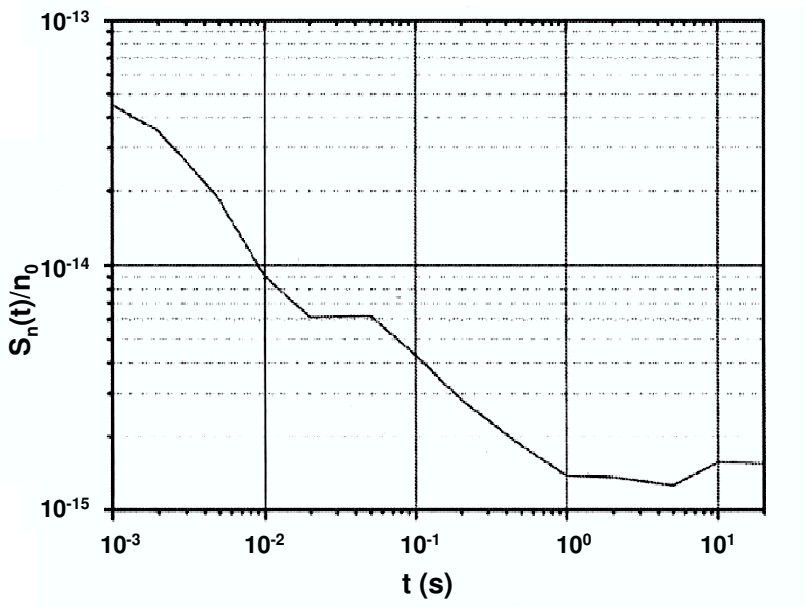

Figure 5.4: Fractional root Allan deviation of the beat frequency with respect to the averaging time. [108]

to a deviation of 0.37 Hz at 5 s. This implies an absolute frequency stability of 9×10^{-16}.

Furthermore, error signals are used to analyze the frequency of the lasers both inside and outside the servo loop. The error signal from the PDH locking of the first cavity is fed to a Fourier-transform-network analyzer when the servo lock is engaged. The residual noise on this in-loop signal gives a measure of how well the light is stabilized to the cavity resonance [39]. The frequency offset between the two cavities is set such that the light light locked to the first cavity is resonant with the second. The servo locked to the second cavity is not engaged and the PDH error produced from the second is used to analyze the frequency of the light. This out-of-loop signal provides a measure of the frequency stability of the light locked to the first cavity relative to the resonance frequency of the second cavity. Figure 5.5 shows the power spectral density for both in-loop and out-of-loop error signals. The in-loop noise is at a much lower level than the out-of-loop noise for frequencies > 50mHz. Hence in this case, the first cavity can be considered as the frequency reference and the out-of-loop signal gives an indication of the relative frequency frequency of the cavity resonances. The relative linewidth calculated from this frequency modulation spectrum [58], after subtraction of the dc component, is 0.98 Hz (full width at half-power). The absolute linewidth of the light locked to one of the cavity is at least a factor of $\sqrt{2}$ smaller, ≈ 0.69

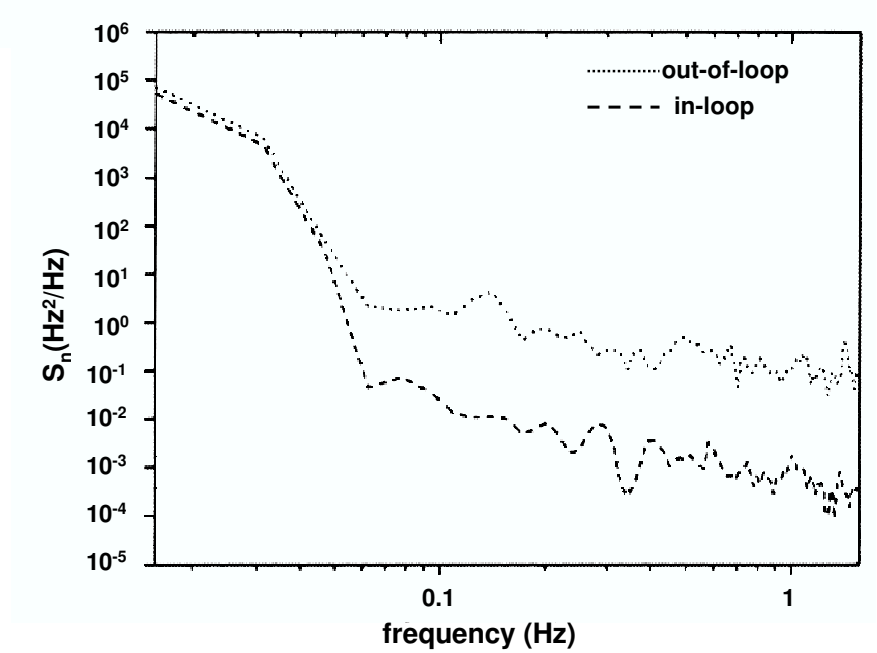

Figure 5.5: Power spectral density of in-loop and out-of-loop error signals; resolution bandwidth, 15.63 mHz. [108]

Hz. This is in reasonable agreement with the absolute linewidth calculated from the beat frequency measurement. A test of the locking accuracy for this setup showed that the relative fluctuation between the error signal's amplitude and offset led to a linewidth of 0.3Hz [131]. Hence, it is likely that the frequency stability of the light is no longer determined by residual fluctuations of the laser source, but is limited only by the stability of the optical resonance to which it is locked. It can therefore be said that the measured relative fluctuations are from independent sources [116].

The stability at short time scales is still thought to be limited by structural instability of the cavity. This can further be reduced by attempting to increase the isolation of the cavities from their environment [117, 119]. However, at longer timescales (> 1 s) the stability is limited by the temperature drift and due to its unpredictability, the rate also has to be continuously updated when compensating during measurements. It was therefore important to investigate ways of reducing this drift and/or rendering it predictable.

5.3.2 Turning point experiment

The most likely cause of this drift is thought to be the residual temperature fluctuations causing expansion or contraction in the spacer material (ULE

glass). The Corning ULE glass used in the construction of the cavities in our experiment is designed to have a zero thermal expansion coefficient ($\alpha = 0$) close to room temperature (as shown in figure 5.6). This has been measured using a non destructive ultrasonic measurement technique [107]. However,

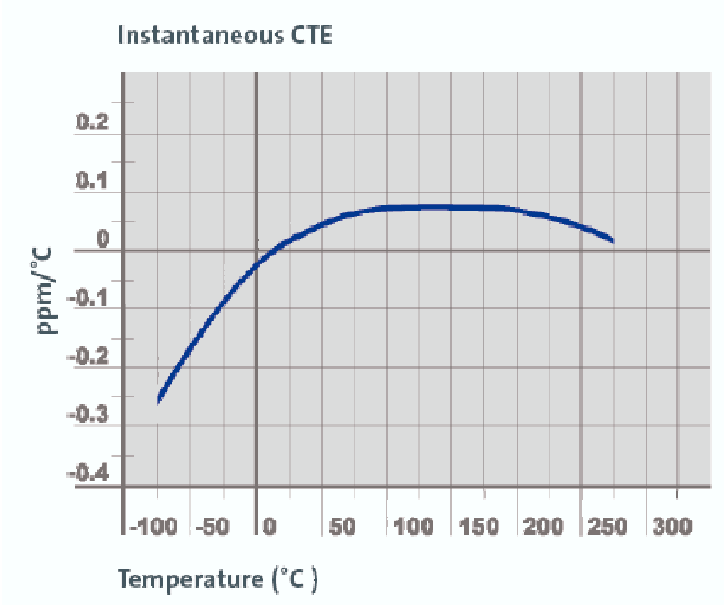

Figure 5.6: Instantaneous coefficient of thermal expansion (CTE) of ULE glass [107].

the manufacturer specifies a temperature range of 5 to 35 degrees C for zero thermal expansion coefficient [106]. The mean coefficient of linear thermal expansion α of ULE cavity is given by

$$\alpha = \frac{1}{L}\left(\frac{\Delta L}{\Delta T}\right) = \frac{1}{\nu}\left(\frac{\Delta \nu}{\Delta T}\right) \tag{5.9}$$

where L is the length of the ULE cavity, $(\Delta L/\Delta T)$ is the change in length of the cavity with temperature, ν is the resonance frequency and $(\Delta \nu/\Delta T)$ is the change is frequency with respect to temperature.

Initially, the measurements were carried out (figure 5.3) with the temperature of both the ULE cavities controlled at 30° C. However, it was not clear whether this temperature was the point at which thermal expansion coefficient of ULE glass vanishes. Hence, an experiment was designed to determine the temperature of ULE cavities at which the thermal expansion coefficient becomes zero. In this experiment, two NPRO type NdYAG lasers are used, each locked to its own cavity, and a heterodyne beat is measured on

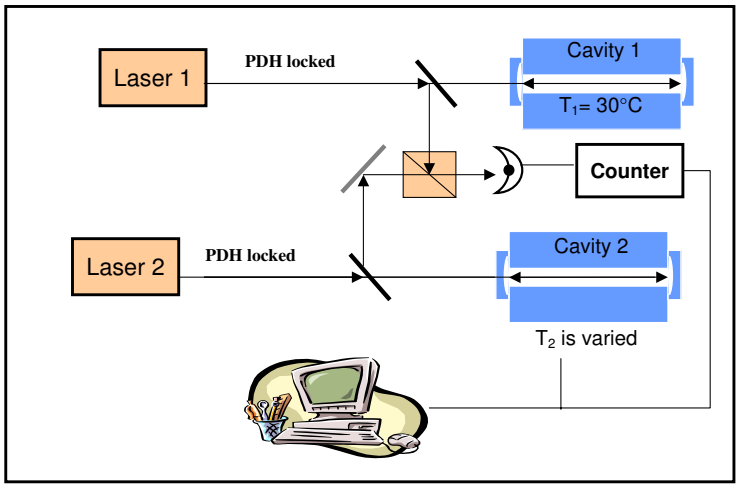

Figure 5.7: Schematic of *Turning point* measurement experimental setup

a frequency counter (figure 5.7). The temperature of one cavity is controlled at 30° C, whilst the temperature of the second is varied. Initial experiments performed by Stephen Webster seemed to show that the temperature at which the zero in thermal expansivity occurs, evidenced by a *turning point* in the beat frequency, is below room temperature. Hence, the vacuum chamber and cavity mounting were modified for cooling, as shown in figure 5.8. Peltier elements are used to cool the cavities below room temperature. The

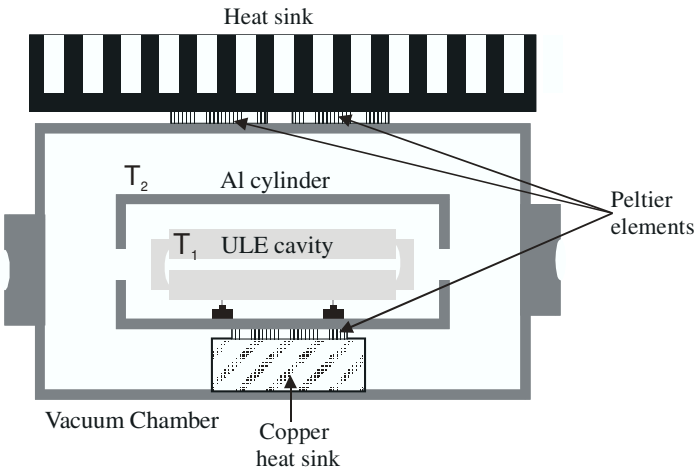

Figure 5.8: Vacuum chamber setup for cooling

temperature of the aluminium cylinder, T_2 is measured using a thermistor in a Wheatstone bridge. However, the temperature of the cavity, T_1 cannot be

measured directly and is inferred from a heat exchange model. There is minimal contact between the cylinder and the cavity, the latter being supported on three diamond tips, and the dominant mechanism for heat transfer is radiation. Energy radiated per second Q, is then given by the Stefan-Boltzmann Law of Radiation:

$$Q = \epsilon\sigma A({T_2}^4 - {T_1}^4) \tag{5.10}$$

where σ is the Stefan-Boltzmann constant[2], ϵ is the emissivity, A is the area, T_2 is the temperature of the outer cylinder and T_1 is the temperature of the cavity. The internal energy of the cavity in terms of mass m and volume V can be written as:

$$Q = mc\frac{dT_1}{dt} = c\rho\frac{dT_1}{dt} \tag{5.11}$$

where c is the specific heat capacity and ρ is the density of ULE glass. Equations 5.10 and 5.11 imply

$$c_p\rho V\frac{dT_1}{dt} = \epsilon\sigma A({T_2}^4 - {T_1}^4) \tag{5.12}$$

Equation 5.12 can then be written as [132]:

$$c_p\rho V\frac{dT_1}{dt} = \frac{\sigma A({T_2}^4 - {T_1}^4)}{\left(\frac{1}{\epsilon_1} + \frac{1-\epsilon_1}{\epsilon_2}\left(\frac{r_1}{r_2}\right)\right)} \tag{5.13}$$

where ϵ_1 and r_1 are the emissivity and radius of the cavity respectively, and ϵ_2 and r_2 are the emissivity and radius of the aluminium cylinder. Assuming that changes in the temperature are relatively small, the rate of change of T_1 can be approximated as

$$\frac{dT_1[t]}{dt} = c(T_2[t] - T_1[t]) \tag{5.14}$$

where c can be considered a constant and is given by

$$c = \frac{4{T_1}^3\sigma A}{c_p\rho V\left(\frac{1}{\epsilon_1} + \frac{1-\epsilon_2}{\epsilon_2}\left(\frac{r_1}{r_2}\right)\right)} \tag{5.15}$$

Multiplying equation 5.14 by e^{ct} on both sides,integrating between the limits $-\infty$ and τ, and exploiting the properties of Laplace transforms, one obtains the following solution for T_1 in terms of T_2 as a function of time:

$$T_1[t] = T_2[0]\int_{-\infty}^{0} e^{c(t-\tau)}dt + \int_{0}^{\tau} T_2[t]e^{c(t-\tau)}dt \tag{5.16}$$

[2]The value of Stefan-Boltzmann constant $\sigma = 5.67 \times 10^{-8}\mathrm{Wm}^{-2}\mathrm{K}^{-4}$

Some of the parameters encapsulated in the constant c, such as the emissivities, are not accurately known, therefore c is left as a free parameter. T_2 is measured for both heating and cooling and an initial guess made for c using reasonable values in order to calculate T_1. The beat frequency, which has also been recorded as a function of time is then plotted as a function of T_1. The value of c is then iterated until as good an overlap as possible is achieved for the cooling and heating curves. Figure 5.9 shows the beat frequency measurement with respect to the calculated temperature of ULE cavity using equation 5.16. The temperature of the aluminium cylinder and the beat frequency were recorded over a period of 3 days for the heating as well as cooling. It is clear from figure 5.9 that a turning point in beat frequency for both cavities occurs at around 12°C indicating that the thermal expansivity has passed through zero. The heating and cooling curves do not overlap perfectly due to the simplicity of the model used. For example, no allowance has been made for the presence of thermal gradients within the cavity itself. This measurement was further refined by scanning smaller ranges of temperatures over longer time periods such that the cavity was nearer to equilibrium at all times. A value of 11.7°C for the temperature of zero expansivity was obtained for both cavities. This is not surprising since both the cavities were made from the same batch of ULE glass. Figure 5.10 shows thermal expansivity, obtained by taking the derivative of the beat frequency, as a function of temperature. A fit to the data yields a slope of 2×10^{-9} K^{-2}, for the rate of change of α with temperature. Hence, the temperature of the ULE cavity only needs to be within a degree of the zero to obtain a low expansion coefficient. Controlling both cavities at the zero in expansivity, the beat frequency was measured over a period of a one and a half days. This result is shown in figure 5.11 The total frequency change is 4.5kHz over a period of 140,000 seconds, or a drift rate ~ 30 mHz/s compared with ~ 500 mHz/s for the previous beat frequency experiment. The measurement is a relative one between the two cavities, therefore, it is hard to predict absolute drift in each cavity. However, it is clear from this measurement that the drift is now relatively predictable and is likely to be isothermal in nature. In the ULE cavities, one also expects a temperature independent *creep* at the level of a few tens of mHz/s, as has been measured elsewhere [120], and it is most probably this effect which is apparent now in the frequency.

5.4 Conclusion

The optical finesse of the 90mm long sapphire cavity was measured to be $\approx 188,260$. Unfortunately, before any beat measurement data could be taken

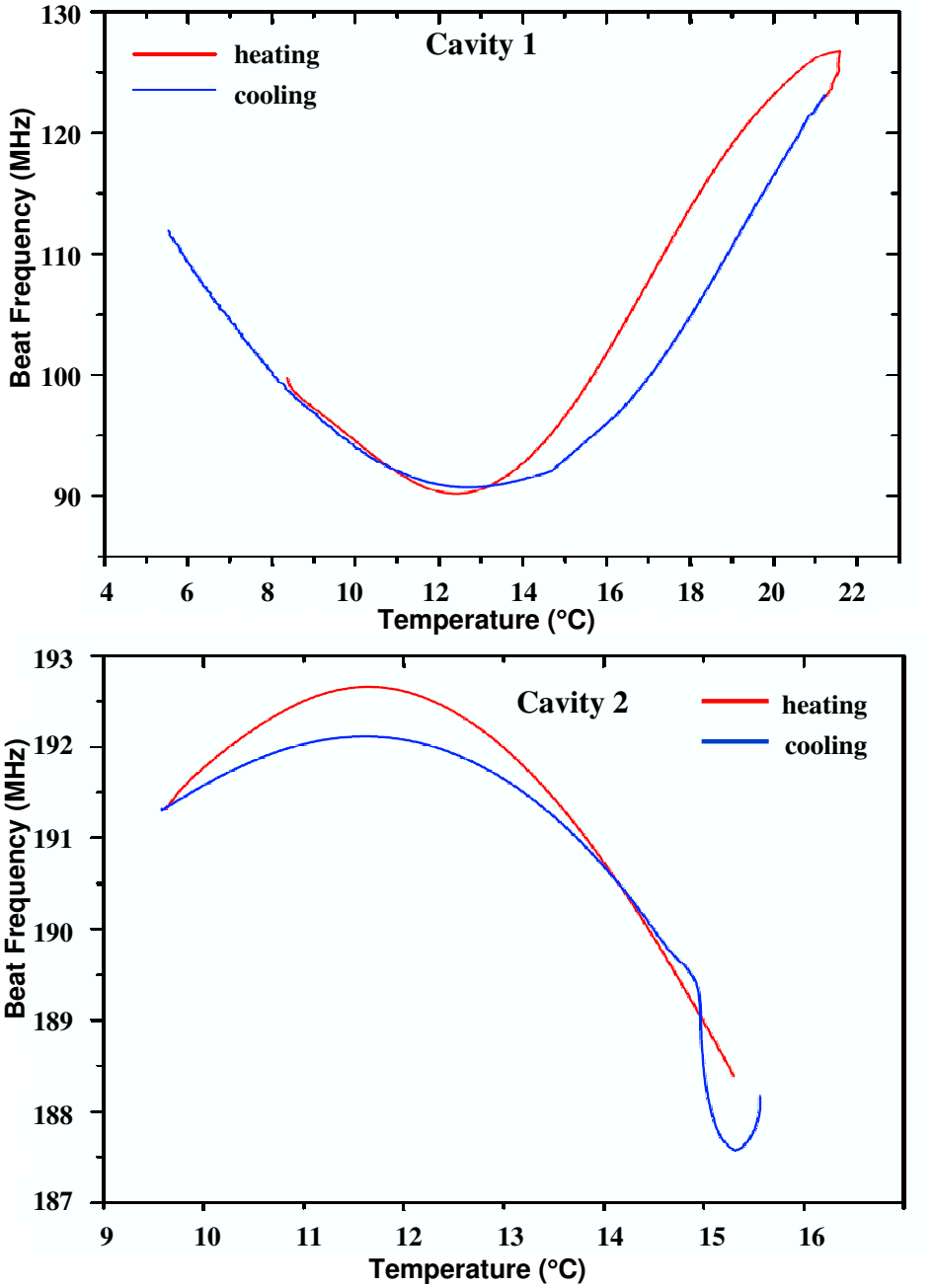

Figure 5.9: Beat Frequency as a function of calculated cavity temperature T_1. The overlap between the heating and cooling curves is not perfect due to the simplicity of the model used to derive the temperature scale. For e.g.,no allowance had been made for the presence of thermal gradients within the cavity itself which is assumed to be in thermal equilibrium throughout.

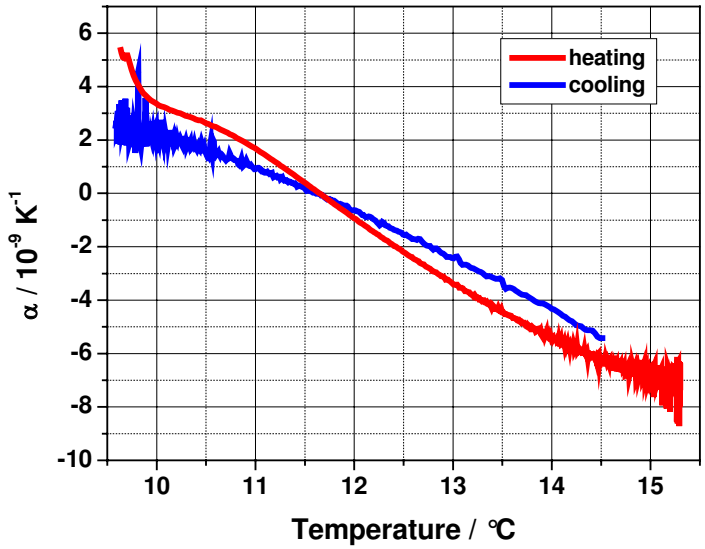

Figure 5.10: Thermal expansivity as a function of cavity temperature. This measurement was taken every few minutes over a over a period of 3 days.

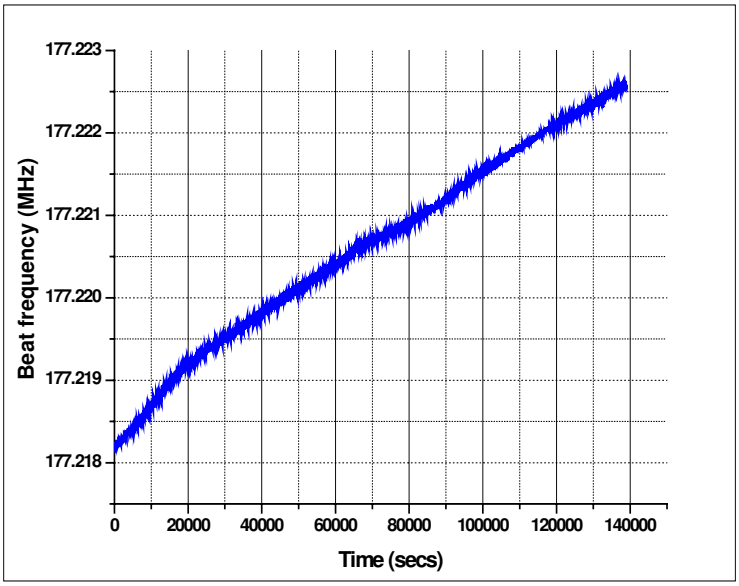

Figure 5.11: Drift over extended period of time

at 4.2K (with both cavities under full temperature control), the mirror at one end of the cavity became detached from the spacer during a slow warm-up from liquid-He to liquid-N_2 temperature. Some initial measurements after PDH locking of laser frequency to the cavities at room temperature revealed a beat frequency of $\approx$ 180 MHz. The cavity mirrors and the spacer were then sent to the United States for repolishing. In the mean time, ULE experiments were carried out and the results have been discussed in this chapter.

A laser linewidth of 0.5Hz has been demonstrated for Nd:YAG laser locked to a high finesse Fabry-Perot cavity made of ULE glass and a stability of a part in 10^{15} is reached at 1s. A zero in the expansivity of the ULE material has been located at a temperature of 11.7 degrees C with the help of a simple heat transfer model. Control of the cavities at this temperature has reduced the relative drift to a level of 30 mHz/s and it is predictable over the long term. Hence it should be possible with compensation to extend the high stability achieved at short timescales into the long term such that an ion trap frequency measurement can be performed. Thermal fluctuations, of the Brownian noise type, may pose the ultimate limit to the laser stability and this issue requires more investigation. Further improvements at short time scales may be achieved by implementing a vibration insensitive cavity design (as discussed in section 6.2.1). Long-term stability can only be improved by reduction of the residual thermal drift.

Chapter 6

Future Work and Conclusions

6.1 Review of the major contributions in this thesis

This thesis concludes with discussion of the effects limiting the frequency stability at the sub-hertz level of a laser frequency-stabilized to a high finesse Fabry-Perot cavity. The cavities used for the experiments described in this thesis are made of two materials: ULE glass (at room temperature) and Sapphire (at liquid-He temperature $\approx$ 4K). In both cases, two similar cavities are employed to get an independent measure of relative frequency stability. A NPRO (non-planar ring oscillator) type Nd:YAG laser's frequency is stabilized to one of the cavities using the Pound-Drever-Hall locking technique by feeding back the PDH error signal to the peizo-electric tuning element bonded to the laser crystal. A part of this beam is transferred via optical fibre to the second platform where its frequency is shifted into resonance with a second Fabry-Perot cavity and locked to it using an acousto-optic modulator (AOM). The PDH locking scheme has been described in detail in section 2.7.3 of this thesis. A relative measure of the stability is obtained through a heterodyne beat measurement of the two beams, one from the laser and other from the beam that passes through the AOM, each locked to its own cavity, by combining the two beams on a photodiode.

Frequency stability results could not be obtained in case of sapphire cavities as one of the mirror became detached from the spacer while the cryostat warmed up from liquid-He to liquid-N_2 temperature. A finesse of $\approx 188,260$ was measured for this cavity. The decay measurement technique used for calculating the finesse has been discussed in section 5.2 of this thesis.

In case of ULE cavities, a laser linewidth of 0.5Hz has been demonstrated for Nd:YAG laser locked to a high finesse Fabry-Perot cavity made of ULE

glass corresponding to a frequency stability of a few parts in 10^{15} at 1s. It is important to point out that during this measurement a drift ~ 0.5Hz/s was compensated to first order. The two main factors that limit the frequency stability of such lasers at the subhertz level are thought to be the following: structural instability of the cavity at shorter timescales and temperature drift due to its unpredictability at longer timescales (> few seconds). The turning point experiment explained in section 5.3 of this thesis is an attempt to reduce the temperature drift for ULE cavities and/or render it predictable such that the long term stability of such lasers can be improved. A simple heat transfer model is used to locate the zero in thermal expansivity of ULE cavity which is around ~ 11.7°C. A long term drift in beat frequency was measured after controlling the cavities at this temperature. This drift was calculated to be $\approx$ 30mHz/s. The measurement is a relative one between the two cavities, therefore, it is hard to predict absolute drift in each cavity. However, it is clear from this measurement that the drift is now relatively predictable and is likely to be isothermal in nature. In the ULE cavities, one also expects a temperature independent *creep* at the level of a few tens of mHz/s. This has been measured elsewhere [120], and it is most probably this effect which was apparent now in the long term beat frequency frequency measurement.

6.2 Future Work

6.2.1 ULE Cavities

Ultrastable lasers are an essential element of optical frequency standards where they are used both to probe an atomic transition and to provide a measurable output. As discussed in chapter 2, an ultrastable laser comprises of an oscillator stabilized to a passive optical cavity. In case of high fidelity control systems, the output frequency is defined by the cavity to which the laser frequency is stabilized. Hence, the dimensional stability of the cavity becomes paramount in such applications. External vibrational forces acting on the cavity cause it to distort and the sensitivity of a cavity to such forces is described in terms of a frequency shift caused by a given degree of acceleration. It is typically of the order of ($\sim$ 100 kHz/ms^{-2}) [109]. Subhertz laser linewidths have been achieved in several experiments [21, 19, 108, 110], in quiet conditions with active as well as passive vibration isolation. However, vibrational forces remain the dominant source of instability at 0.1-10 s time scale. The extreme sensitivity of cavities to vibrations therefore need to be overcome in order to envisage such an apparatus leaving the boundaries

of a specialized laboratory. The availability of ultra narrow atomic references [121], where the observed quality factor, Q is determined by the laser linewidth, also motivates the pursuit of even greater stability. It could be possible to isolate the cavity further from vibrations. However, given the range of contributing frequencies < 10 Hz, the difficulty and expense will far outweigh the return in performance. A better approach by far is to reduce the sensitivity of the cavity to vibrations. This approach has been followed at several laboratories [117, 118, 109] with some success. The rationale behind this approach is discussed below.

Vibration insensitivity measurement - Theory

An optical cavity comprises two highly reflective concave mirrors bonded to a spacer with a central bore and has axial symmetry. The optical mode coincides with the symmetry axis and has a small diameter at the mirror surface relative to the cavity dimensions. Vibration insensitivity in such a case, can be obtained by keeping the distance between the two points at the centers of the mirror surfaces invariant, when a force is applied to the support. This may simply be achieved through symmetrical mounting: a force applied through the mount will cause one half of the cavity to contract while the other half expands with the result that there is no net change in dimension[1] . An obvious way to implement such a system is to hold the cavity vertically about its plane of symmetry with its axis aligned with gravity. A reduced acceleration sensitivity of 10 kHz/ms^{-2} has been demonstrated using this approach [117]. A cavity mounted with its axis horizontal sags asymmetrically under its own weight. However, through optimization of the support positions, the distance between the centers of the mirrors can be made invariant. In such a case, a vertical acceleration sensitivity of 1.5 kHz/ms^{-2} has been demonstrated [118]. Further work on achieving vibration insensitivity in the ULE experiment described in this thesis was carried out by Dr. Stephen Webster at National Physical Laboratory, Teddington. Stephen achieved a similar level of result as Nazarova [118] at PTB, Germany (a vertical acceleration sensitivity < 0.1 kHz/ms^{-2} by removing material from the underside of the cavity [109].

The geometry of the cavity described in reference 6.1 is shown in figure 6.1. Square *cutouts* are made in the lower side of the cylindrical spacer and the cavity is supported at four points. The *cutouts* compensate for the vertical vibrational forces and the vibration insensitivity in the horizontal

[1]It should be pointed out that vibrations cause flexing of the cavities rather than contraction or expansion. However, such an effect can be replicated by the simple model of expansion and contraction mentioned in this section.

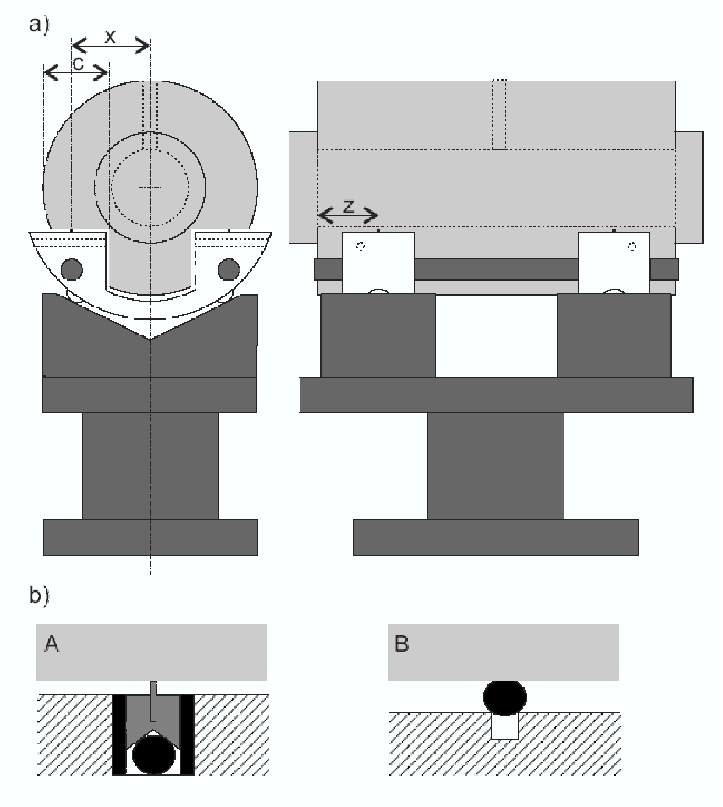

Figure 6.1: a) Cutout cavity on mount. The cavity is represented by the light gray shaded area. The support *yokes* are shown in white. Spacer length, 99.8 mm; diameter, 60 mm; axial bore diameter, 21.5 mm; vent-hole diameter 4 mm. The mirrors are 31 mm in diameter and 8 mm thick. The parameters relevant to the design, the cut depth c and the support coordinates x and z are indicated. b) Details of the support point in cross section. The black shaded areas represent rubber tubes and spheres. Two different mounting options were tested. Case A: Diamond stylus set into a cylindrical ceramic mount, cushioned on all sides by a rubber tube, and from below by a rubber sphere. The stylus digs into the underside of the cavity, and can be considered to be in rigid contact with it. Case B: 3-mm-diam rubber sphere recessed into a cylindrical hole in the yoke. [109]

plane is achieved by symmetrically mounting the cavity. Comsole Multi-Physics Version 3.2 [122] is used to perform the finite element analysis of such a physical system. A static stress-strain model is applied as the frequencies of interest are $<$ 10Hz and therefore can be considered to be at dc relative the first structural resonance ($\sim$ 10 kHz). A detailed analysis of the modeling is given in reference [109]. For a detailed description of finite-element based analysis of cavity deformation under the influence of vibration noise for a number of different cavities and support configurations, the reader is referred to the work of Chen et al [123].

The cavity spacer and mounts were made to the design as shown in figure 6.1. The mirrors and spacer both are made of ULE glass. The two highly reflective concave super-mirrors (Reflection Coefficient, $R = 0.99998$, radii of curvature = 350mm) are optically contacted to the newly designed spacer, concentric with its axis. The cavity is then placed symmetrically on the mount. The symmetrical placement with respect to the mount is ensured with help of small grub screws set within the yokes (see the caption figure 6.1) that can nudge the cavity from either side. Along the horizontal axis symmetrical placement is done by eye and is accurate to within half a millimeter. The yokes can slide along the parallel rods, which ensure that symmetry is maintained while allowing adjustment of z. The cavity has to be lifted off and then replaced back on the support for this adjustment. The difficulty with four contact points is ensuring symmetry of the restoring forces acting at these points. It is therefore necessary to ensure that the forces acting on the base are split equally between the contact points. Figure 6.1b) shows the two types of contact used for this setup. In both cases the contact is made compliant using rubber tubes and/or spheres. As these are by far the most elastic elements of the whole support, they in fact define the compliance. The task of achieving force symmetry is thus simplified. The two things that need to be kept in mind are: the stiff part of the mount is symmetric and the compliant elements are identical.

Vibration insensitivity measurement - Results

The response of the cavity to vibrations is measured using the setup shown in figure 6.2. Two Nd:YAG lasers at 1064 nm are frequency controlled to two independent optical cavities. One of the cavities is modified as described above. Light from both lasers is picked off using beam splitters and then combined on a fast photodiode to obtain a beat note. The beat note provides a measure of relative frequency fluctuations between the two systems. The power spectrum of these fluctuations is analyzed using a frequency to voltage converter. Both the cavities are placed on active vibration isolation

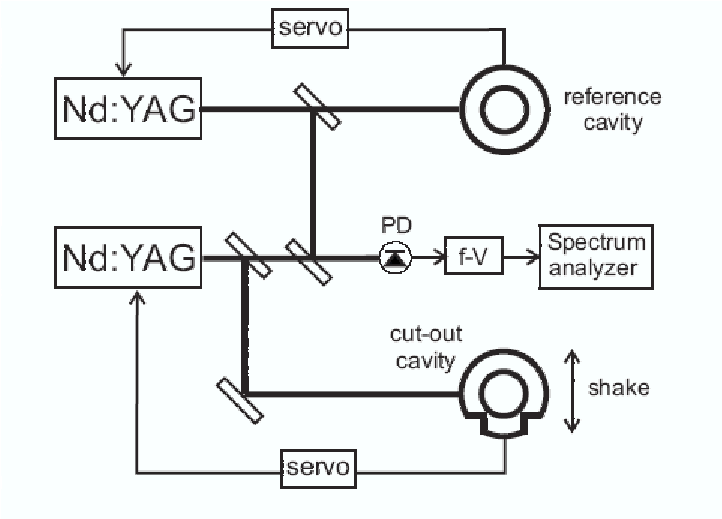

Figure 6.2: Schematic of experimental setup for measuring vibration response. PD: photodiode; f-V: frequency-to-voltage converter. The thicker lines indicate beam paths; the thinner lines indicate electronic signal paths. [109]

(AVI) platforms. The active vibration isolation is switched on for the reference cavity whereas for the newly modified cavity, the AVI is used in reverse as a *shaker*: a sinusoidal acceleration can be applied along any one of three orthogonal axes to which the axes of the cavity are aligned. The amplitude of the acceleration on the platform is measured using a three-axis seismometer. A drive frequency of 15 Hz is chosen and this modulation at the drive frequency can be resolved in the power spectrum. A response is then derived from the modulation amplitude and measured acceleration. The experimental and theoretical model response to vertical vibrations in such a system as a function of support position (c = 18.45 mm, x = 22 mm, and z = 17 mm) is shown in figure 6.3. A very good discussion of these results is given in reference [109]. The response to horizontal vibrations is more difficult to null as it depends critically upon the symmetry of the mount [109]. For case A:(figure 6.1) where the cavity is mounted on the diamond styli, the null in the vertical direction is good (as shown in figure 6.3). However, the response in horizontal direction varies in the range $10 - 100$ kHz/ms^{-2}. For case B:(figure 6.1) where the diamond stili are replaced with rubber spheres, the horizontal response is 3.7(0.9) kHz/ms^{-2} in line with (perpendicular to) the cavity axis, while the vertical response is < 0.1 kHz/ms^{-2}. A better result is achieved in case B because the rubber spheres are more horizontally compliant than the rubber tubes and also they are closer to being geometrically identical than the components used in case A. However, a problem with

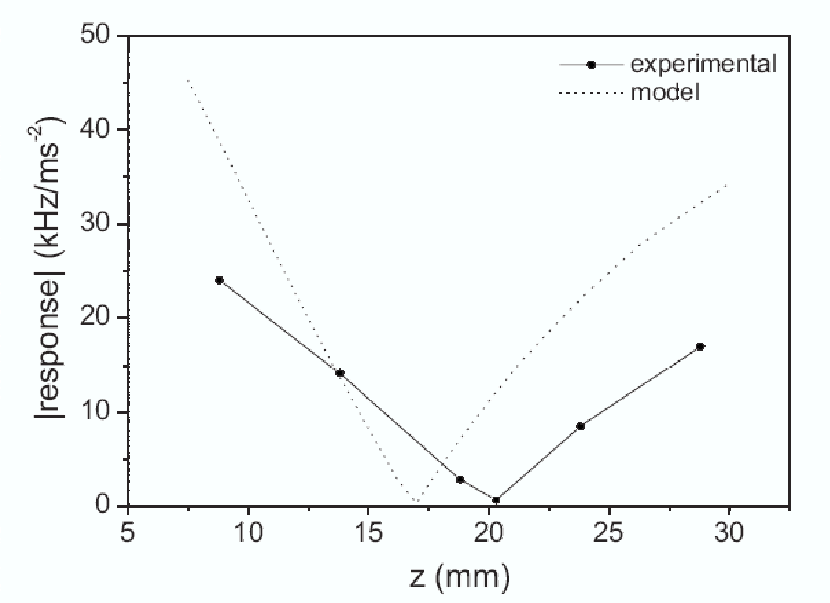

Figure 6.3: Plot of experimental response of cutout cavity to vertical acceleration as a function of the support position. $c = 18.45$ mm, $x = 22$ mm, and $z = 17$ mm. The response predicted by the model is also shown. This is calculated by converting the displacement to the frequency change this would induce, taking into account that the center points of the two mirrors are displaced by equal and opposite amounts.The minimum value for the vertical vibrations is 0.6 kHz/ms^{-2} for $z = 20.3$ mm [109].

using elastic contact points such as rubber sphere in case B is that the whole support becomes resonant, which was tested by driving the AVI tables used in our experiment at high frequencies. The response was found to be broadly resonant, amplified upto a factor of seven at 40Hz. This however was not considered to be a serious problem as the AVI table has an attenuation of 35 dB for frequencies $>$ 10Hz. Hence, this resonant response can be compensated for by the high degree of isolation that an AVI provides. Accelerations at frequencies $<$ 10 Hz make a dominant contribution to the frequency noise, however, the attenuation of an AVI falls off in this range and it ceases to isolate below $\sim$ 2Hz. For the vibration insensitivity to be of use, it is vital that the effective dc response of the cavity be reduced which is achieved by the cutout design.

Future Work

A good qualitative agreement between the experimental results and the theoretical model is shown in figure 6.3. However, there are certain discrepancies that need to be addressed. The model predicts a null at lower z and the gradient about the null is also larger. The dependence of the null on experimentally adjustable parameters diminishes the importance of the model's accuracy, as a null can be found over a wide range of values. Further work therefore needs to be done to discover the origin of these discrepancies. The results obtained in this experiment offer more than two orders of magnitude lower sensitivity to vertical vibrations compared to the work of Notcutt et al. [117] and more than an order of magnitude ($>$ factor of three) lower sensitivity to vertical or horizontal vibrations compared to the work of Nazarova et al. [118]. In terms of preferred mounting direction of the cavity (horizontal or vertical), the cavity is most sensitive to vibrations along its axis. It is therefore beneficial to align the cavity axis with the direction of least vibration. The AVI platforms used in this work have little dependence of the magnitude of acceleration on direction, hence, there is no preferred orientation of the cavity.

Once the vibration insensitivity is achieved, the frequency stability of light controlled to the cavity will become limited by dimensional changes due to thermal fluctuations of the mirror substrates and their coatings [119]. To suppress such fluctuations, it would be better for the cavity to be longer, such that they become a smaller fraction of the cavity's total optical length. Locating the zero in response of the cavity to vibrations relies upon accurate positioning of the support points and balancing of the restoring forces at those points. The absolute experimental errors in position or force are unlikely to change significantly when the cavity's length is increased, and

the cavity's strain is proportional to each of these absolute errors. The increase in the length of the cavity therefore should not affect the vibration insensitivity. The cavity length may thus be increased while maintaining the same vibration insensitivity with the advantage that the effect of thermal fluctuations will be reduced.

6.2.2 Sapphire cavities

As described in section 5.2 of this thesis, the newly polished sapphire mirrors and spacer were optically contacted at at the clean room in Imperial College London. However, a strange phenomenon was observed when the 1064 nm laser light was incident on the cavity - the maximum fractional power transmitted through the whole cavity, when the laser light is in resonance with the TEM_{00} mode of the cavity, was observed to be approximately 0.015%. Initially, it was attributed to the patchy coating on sapphire supermirrors. Hence, it was decided to remove the optically contacted mirror from one end of the cavity and adjust the position of this mirror such that the transmission through the cavity is maximized when the 1064 nm laser light is in resonance with the TEM_{00} mode of the cavity. This work was carried on by Dr. Mark Oxborrow at National Physical Laboratory. For the first (and last!) time in its 13 year history, the experiment was finally fully assembled and gotten to work, with the cavities/resonator at liquid-helium temperature, on the 24th April 2007. In particular, the optical mirrors on the ends of each spacer did not de-contact upon cooling down. Data was collected intermittently until April 28th, at which point it was concluded that no significant improvements in the stabilities of the two (optical and microwave) beat notes could be obtained without major alterations identified and discussed here briefly.

In the course of this last experimental run, it was observed that the commercial (Innolight Mephisto) Nd:YAG laser used to supply the optical rigs two interrogating laser beams suffered intermittently (once every half an hour or so, lasting about a minute) from a storm of severe relaxation oscillations, causing severe amplitude modulation of its output beam of sufficiently severity to cause a severe drop in the quality of both PDH error signals, and often causing these optical servos to fall out of lock. As no immediate remedy for preventing these oscillations could be devised, only several sections of data, each lasting several tens of minutes, were obtained. An analysis of a representative such section provides the results shown in figure 6.4.

No obvious correlation between the optical and microwave beat frequency could be discerned from figure 6.4, suggesting that fluctuations in the temperature (hence the dimensions: length and circumference) of the 90-mm optical cavity were not the most significant cause of instability. Compared

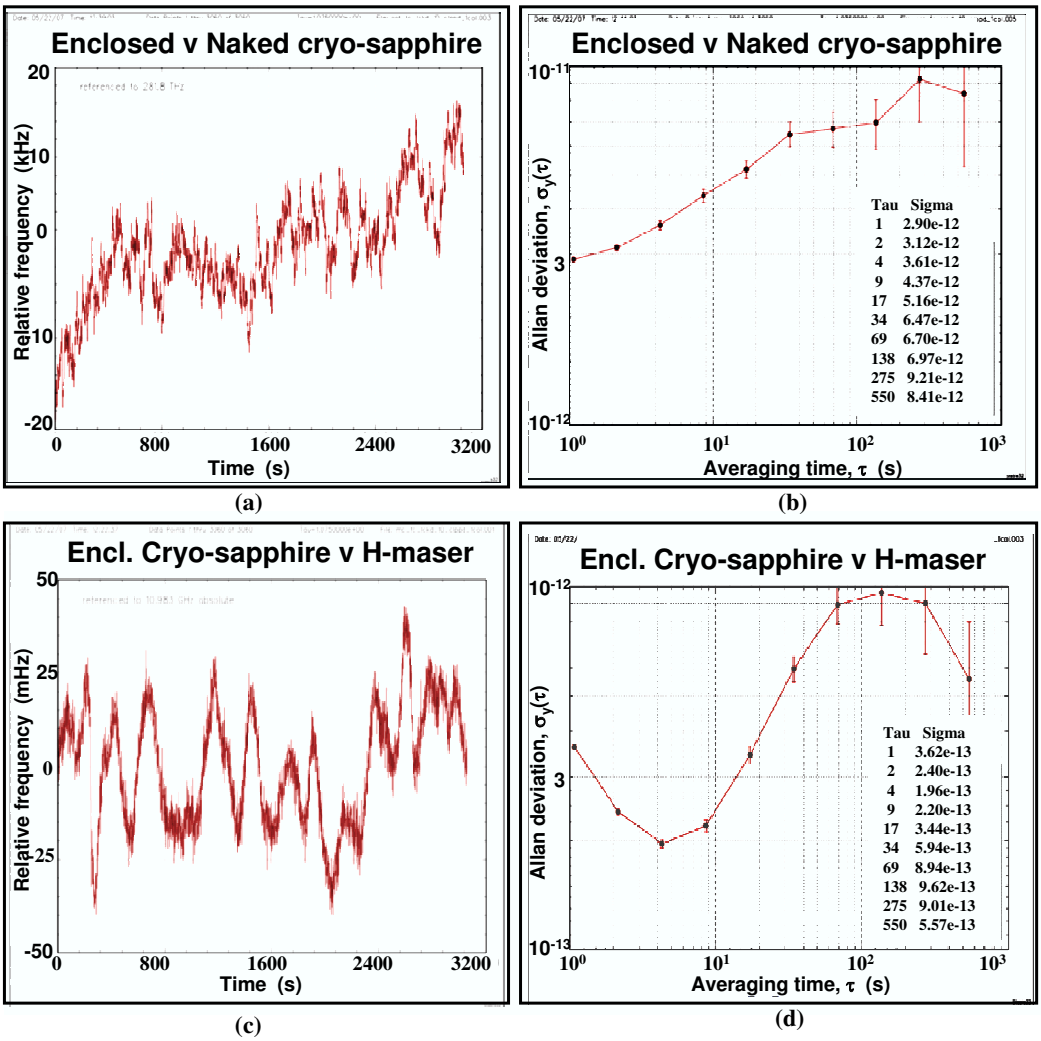

Figure 6.4: The top two graphs (a) and (b) show the optical frequency stability: (a) Normalized beat frequency difference between the 90-mm optical cavity (housed inside a microwave enclosure) and the naked 70-mm cavity supported with a copper clamp. (b) The relative fractional-frequency root Allan deviation corresponding to the beat-note data in (a). The bottom two graphs (c) and (d) show the microwave frequency stability: (c) Normalized beat frequency difference between the 10.983,250, GHz output of WGmode cryo-sapphire microwave oscillator and the output of an H-maser-referenced Anritsu 69253A synthesizer (set to 10.983 GHz, exactly). (d)Relative fractional-frequency root Allan deviation corresponding to the beat-note data in (c).

to what has been achieved both elsewhere [30] and in other experiments at NPL over recent years, both the optical and microwave stabilities displayed in figure 6.4 ($\sim 3 \times 10^{-12}$ at 1 second and $\sim 2 \times 10^{-13}$ at 5 seconds, respectively) were poor. It must be born in mind, however, that it was the very first time that the experiment had ever worked and several obvious technical improvements that suggested themselves during the experimental run were never implemented. A few (less-obvious) explanations or excuses for the observed poor stabilities were identified and are mentioned below:

- The thermal resistance of the copper-niobium hybrid straps between the cryogenic sapphire cavities/resonator and the cryostat cold face at liquid-helium temperature were set too high, leading to poor temperature control. The addition of extra copper straps between the optical cavity and the cryostats cold face could have easily provided the required reduction in thermal resistance, but this was not implemented.

- Due to the high thermal resistance of the hybrid straps, the enclosed optical cavity was not maintained at its frequency versus temperature turnover point of its 10.983 GHz whispering-gallery mode. In addition, the bandwidth of the cavities temperature-control servos, implemented via LabView was restricted to less than a Hz due to a software bug. It was thus not surprising that the observed stability at 5 seconds (and above) is approx. 100 times worse than that obtained with NPLs pair of 9.204 GHz cryo-sapphire WG-mode microwave oscillators. (Note that, at short time periods $< 5 - 10$ seconds , the measured stability is dominated by fluctuations in the frequency of the H-masers 10-MHz reference and instabilities in the Anritsu synthesizer.)

- The way in which the two optical cavities were supported could have imposed significant The way in which the two optical cavities were supported could have imposed significant (and fluctuating) mechanical strains. The enclosed optical cavity was supported from its ends within a copper enclosure, the naked etalon around its middle by a copper clamps as described in section 4.5.2. and 6a.

- Due to the swinging and deformation of the cryostats insert (as its temperature profile changed as helium boiled off), the optical alignment had to be regularly readjusted so as to maintain optical power through each cavity (hence and error signal for locking). It was noted that such adjustments had a significant effect on both the temperature of each cavity/resonator and upon the optical and microwave beat-frequencies themselves. This indicated that optical heating could significantly pull

the cavities' temperatures. This pulling phenomenon was probably exacerbated by the optical cavities' poor thermal anchorage. Applying lower optical power was not an option as this caused the PDH error signals to be unacceptably noisy.

Unfortunately, all these improvements could not be implemented due to financial constraints on this project. Hence, no further progress has been made in this case.

6.2.3 Conclusion

This chapter summarizes major contributions of the thesis and further work that has been done or being planned on both sapphire and ULE cavities. The vibration insensitivity setup designed and developed by Stephen Webster at National Physical laboratory including the future plans has been explained. The final measurements and improvements that need to be implemented in case of the sapphire experimental setup have also been presented. No further work has been planned for improving the sapphire experimental setup due to the long timescales that were involved in getting some initial measurements and the financial constraints that limit the funding to this experiment.

Appendix A

Characterization of laser noise

A.1 Spectral density to Allan variance relation

If the fractional frequency fluctuations in the laser output are denoted by $y(t)$, then the auto-correlations function $R_y(\tau)$ is given by

$$R_y(\tau) = \langle y(t)y(t+\tau)\rangle = \lim T \to \infty \frac{1}{T}\int_0^T y(t)y(t+\tau)d\tau \tag{A.1}$$

and by Weiner-Kintchine relationships, the spectral density of the fractional frequency fluctuations $S_y(f)$ is

$$S_y(f) = \int_{-\infty}^{\infty} R_y(\tau)\exp(-j2\pi f)d\tau \tag{A.2}$$

As described in section 2.3.2, Allan variance ${\sigma_y}^2(\tau)$ is

$${\sigma_y}^2(\tau) = \langle \frac{\overline{y}_{i+1} - \overline{y}_i{}^2}{2}\rangle = \frac{1}{2}\left\langle \left(\frac{1}{\tau}\int_{t_{i+1}}^{t_{i+1}+\tau} y(t)dt + \frac{1}{\tau}\int_{t_i}^{t_i+\tau} y(t)dt\right)^2\right\rangle \tag{A.3}$$

The above equation can be can be written as the convolution of $y(t)$ with *impulse function* $h_A(t)$ shown in fig 1.

$${\sigma_y}^2(\tau) = \left\langle (y(t)\otimes h_A(t))^2\right\rangle = \left\langle \left[\int_{-\infty}^{\infty} y(t)h_A(\tau - t)dt\right]^2\right\rangle \tag{A.4}$$

Using the Parseval's theorem the above equation can be written as

$${\sigma_y}^2(\tau) = \left\langle \int_{-\infty}^{\infty} \left|F\left[y(t)h_A(\tau - t)\right]\right|^2 df\right\rangle \tag{A.5}$$

where $F\left[y(t)h_A(\tau - t)\right]$ is the Fourier transform of $[y(t)h_A(\tau - t)]$. By the convolution property of the Fourier transform

$$\sigma_y{}^2(\tau) = \left\langle \int_{-\infty}^{\infty} |F[y(t)]|^2 \, |F[h_A(t)]|^2 \, df \right\rangle \tag{A.6}$$

Or,

$$\sigma_y{}^2(\tau) = \int_{-\infty}^{\infty} \left\langle |F[y(t)]|^2 \right\rangle df. \int_{-\infty}^{\infty} \langle |F[h_A(t)]| \rangle^2 \, df \tag{A.7}$$

The first term in equation A.7 is the spectral density of the fraction frequency fluctuations and second term is the the square of the Fourier transform of the *impulse function*. Thus equation A.7 can be re-written as

$$\sigma_y^2(\tau) = \int_{-\infty}^{\infty} S_y(f) \frac{sin^4(\pi f \tau)}{(\pi f \tau)^2} df = 2 \int_0^{\infty} S_y(f) \frac{sin^4(\pi f \tau)}{(\pi f \tau)^2} df \tag{A.8}$$

Bibliography

[1] A. Cook, *The observational foundations of Physics* (Cambridge University Press, 1994).

[2] The speed of light in vacuum is exactly equal to 299,792,458 meters per second.

[3] L. Hollberg, C. W. Oates, E. A. Curtis, E. N. Ivanov, S. A. Diddams, Th. Udem, H. G. Robinson, J. C. Bergquist, R. J. Rafac, W. M. Itano, R. E. Drullinger, D. J. Wineland, *Optical Frequency Standards and Measurements*, IEEE Journal of Quantum Electronics **37**, 1502-1513 (2001).

[4] S. A. Diddams, Th. Udem, J. C. Bergquist, E. A. Curtis, R. E. Drullinger, L. Hollberg, W. M. Itano, W. D. Lee, C. W. Oates, K. R. Vogel, D. J. Wineland, *An optical clock based on a single trapped 199Hg+ ion*, Science **293**, 825 (2001).

[5] Diode pumped non planar ring oscillator (Nd:YAG) laser manufactured by Lightwave electronics has a linewidth of $<$ 5kHz over 1msec.

[6] Coherent laser Group,*MBR110 Specifications.*

[7] American National Standards for Telecommunications, *Telecom Glossary 2000*, Web resource http://www.atis.org/tg2k/

[8] National Institute of Standards and Technology, *A revolution in Time Keeping*, Web resource http://physics.nist.gov/GenInt/Time/revol.html

[9] Becker and Sauter, *Electromagnetic Fields and Itercations*, Vol. 2.

[10] I. I. Rabi, *On the process of space quantization*, Phys. Rev. **49**, 324-328 (1936).

[11] S. Millman, J. R. Zacharias, *The Signs of Nuclear Magnetic Moments of Li^7, Rb^{85}, Rb^{87} and Cs^{133}*, Phys. Rev. **51**, 1049-1052 (1937).

[12] NIST, *Glossary: Time and Frequency from A to Z*, Web resource http://www.boulder.nist.gov/timefreq/general/enc−st.htm

[13] NIST, *Glossary: Time and Frequency from A to Z*, Web resource http://www.boulder.nist.gov/timefreq/general/glossary.htm

[14] Encyclopedia, *World iQ dictionary* , Web resource http://www.wordiq.com/definition/Accuracy

[15] Environmental Monitoring and Assessment Program, *Glossary*, Web resource http://www.epa.gov/emap/html/pubs/docs/resdocs/

[16] J. Reichert, R. Holzwarth, Th. Udem, and T. W. Hänsch, *Measuring the frequency of light with modelocked lasers*, Opt. Comm. **172**, 59-68 (1999).

[17] Long−Sheng Ma, Z. B. A. Bartels, L. Robertsson, M. Zucco, R. S. Windeler, G. Wilpers, C. Oates, L. Hollberg, S. A. Diddams, *Optical Frequency Synthesis and Comparison with Uncertainty at the 10^{-19} Level*, Science **303**, 1843-1845 (2004).

[18] S. A. Diddams, L. Hollberg, Long−Sheng Ma, L. Robertsson, *Femtosecond−laser−based optical clockwork with instability $< 6.3 \times 10^{-16}$ in 1s*, Opt. Lett. **27**, 58-60 (2002)

[19] M. Eichenseer, A. Yu. Nevsky, Ch. Schwedes, J. Von. Zanthier, and H. Walther, *Towards an Indium Single−Ion Optical Frequency Standard*, J. Phys. B **36**, 553-559 (2003)

[20] B. C. Young, F. C. Cruz, W. M. Itano, and J. C. Bergquist, *Visible Lasers with Subhertz Linewidths*, Phys. Rev. Lett. **82**, 3800-3802 (1999)

[21] B. C. Young, R. J. Rafac, J. A. Beall, F. C. Cruz, W. M. Itano, D. J. Wineland and J. C. Bergquist, *Hg+ optical frequency standard: Recent progress*, Laser Spectroscopy XIV Internation Conference, edit by R. Blatt (World Scietific, Singapore), 61-70 (1999)

[22] L. Marmet, A. Madej, K. Siemsen, J. Bernard, B. Whitford, IEEE Trans. Instrum. Meas. **46**, 169 (1997).

[23] J. L. Hall, Proc. SPIE **1837**, 2 (1992).

[24] F. Bayer−Helms, H. Darnedde, G. Exner, Metrologia **21**, 49 (1985).

[25] J. P. Richard and J. J. Hamilton,*Cryogenic monocrystalline silicon Fabry−Perot cavity for the stabilization of laser frequency*, Rev. Sci. Instrum. **62**, 2375-2378 (1991).

[26] C. T. Taylor, M. Notcutt, and D. G. Blair, *Cryogenic, all−sapphire, Fabry−Perot optical frequency reference*, Rev. Sci. Instrum. **66**, 955-960 (1995).

[27] S. Seel, R. Storz, G. Ruoso, J. Mlynek and S. Schiller *Cryogenic optical resonators: a new tool for laser frequency stabilization at the 1 Hz level*, Phys. Rev. Lett. **78**, 4741 (1997).

[28] S. Schiller et al., Proc. Soc. Photo−Opt. Instrum. Eng. **2378**, 138 (1995).

[29] M. Notcutt, C.T. Taylor, A.G. Mann, R. Gummer and D.G. Blair, *Cryogenic system for a sapphire Fabry−Perot optical frequency standard* Cryogenics **36**, 13-16 (1996).

[30] H. Müller, S. Herrmann, C. Braxmaier, S. Schiller, A. Peters, *Modern Michelson−Morley experiment using cryogenic optical resonators*, Phys. Rev. Lett. **91**, 020401 (2003).

[31] H. Müller, S. Herrmann, C. Braxmaier, S. Schiller, A.Peters, *Theory and technology for a modern Michelson−Morley Test of Special Relativity*, Appl. Phys. B **77**,719-731 (2003).

[32] H. Müller, S. Herrmann, A. Saenz, A. Peters, C. Lämmerzahl, *Optical cavity tests of Lorentz invariance for the electron*, Phys. Rev. D **68**, 116006 (2003).

[33] H. Müller, C. Braxmaier, S. Herrmann, A. Peters, and C. Lämmerzahl *Electromagnetic cavities and Lorentz invariance violation*, Phys. Rev. D **67**, 056006 (2003).

[34] H. Müller, C. Braxmaier, S. Herrmann, O. Pradl, C. Lämmerzahl, J. Mlynek, S. Schiller and A. Peters *Testing the foundations of relativity using cryogenic optical resonators*, Int. J. Mod. Phys. D **11**, 1101-1108 (2002).

[35] C. Lämmerzahl, C. Braxmaier, H. Dittus, H. Müller, A. Peters and S. Schiller, *Kinematical test theories for Special Relativity: a comparison*, Int. J. Mod. Phys. D **11**, 1109-1136 (2002).

[36] C. Braxmaier, H. Müller, O. Pradl, J. Mlynek, A. Peters and S. Schiller *Tests of Relativity Using a Cryogenic Optical Resonator*, Phys. Rev. Lett. **88**, 010401 (2002).

[37] G. Ruoso, R. Storz, S. Seel, S. Schiller and J. Mlynek, *Nd:YAG laser frequency stabilization to a supercavity at the 0.1 Hz level*, Optics Comm. **133**, 259-262 (1997).

[38] T. Day, E.K. Gustafson and R.L. Byer, *Sub−hertz relative frequency stabilization of two diode laser−pumped Nd:YAG lasers locked to a Fabry−Perot interferometer*, IEEE J. of Quantum Electronics **28**, 1106-1117 (1992).

[39] Ch. Saloman, D. Hills and J.L. Hall, *Laser stabilization at millihertz level*, J. Opt. Soc. Am. B **5**, 1576-1587 (1988).

[40] M.W. Hamilton, *An introduction to stabilized lasers*, Contemporary Physics **30**, 21-33 (1989).

[41] A. Yariv, *Optical Electronics in Modern Communications*, 5^{th} Edition (1996).

[42] P.W. Milloni and J.H. Eberly, *Lasers* (1988).

[43] A.E. Siegman, *Lasers*, University Science Books (1987).

[44] M. Roberts, P. Taylor, P. Gill, *Laser linewidth at the hertz level*, NPL Report CLM (1999).

[45] R.W.P. Drever, J.L. Hall, F.V. Kowalski, J. Hough, G.M. Ford, A.J. Munley and H. Ward, *Laser phase and frequency stabilization using an optical resonator* , Appl. Phys. B **31**, 97-105 (1983).

[46] J. Rutman and D.F. Walls, *Characterization of frequency stabilty in Precision frequency sources*, Proc. of IEEE **79**, 952-959 (1991).

[47] D.W. Allan, , IEEE Trans. Ultraso. Ferroelec. Freq. Contr. **34**, 647-654 (1987).

[48] L. Ju and D.G. Blair, *Compound Pendulum Test Mass Systems for Laser Interferometer Gravitational Wave Detectors*, Meas. Sci. Technology **5**, 1053-1060 (1994).

[49] K. Beauchamp and C. Yuen, *Digital Methods for Signal Analysis*, Cambridge university Press(1979).

[50] E.A. Curtis, *Quenched narrow−line laser cooling of 40Ca with application to an optical clock based on ultracold neutral Ca atoms*, PhD Thesis, University of Colorado (2003).

[51] L.S. Cutler and C.L. Searle, *Some aspects of the theory and measurements of frequency fluctuations in frequency standards*, IEEE Proc. **54**, 136-154 (1966).

[52] D.W. Allan, H. Hellwig, P. Kartaschoff, J. Vanier, J. Vig, G.M.R. Winkler, and N. Yannoni, *Standard Terminology for Fundamental Frequency and Time Metrology*, Proc. of the 42nd Annual Symposium on Frequency Control, 419-425 (1988).

[53] D.W. Allan, *Statistics of atomic frequency standards* IEEE Proc. **54**, 221-230, (1966).

[54] Y. Liu and J. Ohtsu, *Dynamics and Chaos Stabilization of Semiconductor Lasers with Optical Feedback from an Interferometer*,IEEE J. of Quantum Electronics **33**, 1163-1169, (1997).

[55] C.H. Henry, *Theory of phase noise and the Power spectrum of a single mode injection Laser*, IEEE J. of Quantum Electronics **QE-19**, 13911397, (1983).

[56] E. Hecht, *Optics*, 2^{nd} edition, (1987).

[57] F.J. Mendieta, H. Mejía, M. Corona, *A processor for the real time measurement of oscillator Allan Variance*, Instrumentation and Development **3**, 21-28, (1996).

[58] D.S. Elliot, R. Roy and S.J. Smith, *Extracavity laser bandshape and bandwidth modification*, Phys. Rev. A **26**, 12-18, (1982).

[59] B. Dahmani, L. Hollberg and R. Drullinger *Frequency stabilization of semiconductor lasers by resonant optical feedback*, Opt. Lett. **12**, 876-878 (1987).

[60] D.A. Shaddock, M.B. Gray and D.E. McClelland, *Frequency locking a laser to an optical cavity by use of spatial mode interference*, Opt. Lett. **24**, 1499-1501,(1999).

[61] J. Harrison and A. Moordian, *Laser spectroscopy VIII*, 354,(1985)

[62] J. Lazar,O. Číp and B. Růžička, *The design of a compact and tunable extended−cavity semiconductor laser*, Meas. Sc. and Tech. **15**, N6-N9, (2004).

[63] M.G. Littman, *Single−mode operation of grazing−incidence pulsed dye laser*, Opt. Lett. **3**, 138140, (1978).

[64] C.J. Hawthorn, K.P. Weber and R.E. Scholtena, *Littrow configuration tunable external cavity diode laser with fixed direction output beam*, Rev. of sci. instr. **72**, 4477-4479, (2001).

[65] Encyclopedia of Laser Physics and Technology *Extended Cavity Diode Laser, ECDL* , http://www.rp−photonics.com/extended_cavity_diode_lasers.html.

[66] C.E. Wieman and L. Hollberg, *Using diode lasers for atomic physics*, Rev. Sci. Instrum. **62**, 120 (1991). This is a review paper about diode lasers and atomic physics.

[67] T.J. Kane and R.L. Byer, *Monolithic, unidirectional single−mode Nd:YAG laser*, Opt. Lett. **10**, 65-67, (1985).

[68] T.J. Kane, A.C. Nilsson and R.L. Byer, *Frequency stability and offset locking of a laser−diode−pumped Nd:YAG monolithic nonplanar ring oscillator*, Opt. Lett. **12**, 175-177, (1987).

[69] T. Day, *Frequency stabilized solid state lasers for coherent optical communications*, PhD thesis, Stanford university, (1990).

[70] A.C. Nilsson, E.K. Gustafson and R.L. Byer, *Eigenpolarization theory of monolithic nonplanar ring oscillators*, J. Quantum Elec. **25**, 767-790, (1989).

[71] Mephisto, *Innolight GmbH Products Techincal details*, Web resource http://www.innolight.de/products/mephisto/technical−details.htm

[72] Innolight GmbH, *Mephisto Series Users Manual*.

[73] T.W. Hänsch and B. Couillaud, *Laser frequency stabilization by polarization spectroscopy of a reflecting reference cavity*, Opt. Commun. **35**, 441-444, (1980).

[74] R.L. Barger, M.S. Sorem and J.L. Hall, *Frequency stabilization of a cw dye laser*, App. Phys. Lett. **22**, 573-575, (1973).

[75] J. Helmecke, S.A. Lee and J.L. Hall, *Dye laser spectrometer for ultrahaigh spectral resolution: design and performance*, App. Opt. **21**, 1686-1694, (1982).

[76] Y.V. Troitskii, *Optimization and comparison of the characteristics of optical intereference discriminators*, Sov. J. of Quantum Electron. **8**, 628-631, (1978).

[77] Eric.D. Black, *An introduction to Pound−Drever−Hall frequency stabilization*, Am. J. of Physics **69**, 79-87, (2001).

[78] P. Horowitz and W. Hill *The Art of Electronics*, Cambridge University Press.

[79] *Encyclopedia of Laser Physics and Technology*, http://www.rp−photonics.com/.

[80] T. Baer, F. V. Kowalski, and J. L. Hall, *Frequency stabilization of a 0.633−Mum He−Ne longitudinal Zeeman laser*, Applied Optics **19**, 3173, (1980).

[81] Reza Mansouri and Roman U. Sexl, *A test theory of special relativity: I. Simultaneity and clock synchronization* , General Relativity and Gravitation **8**, No. 7, 497-513, (1977).

[82] H.P. Robertson, *Postulate versus Observation in the Special Theory of Relativity*, Rev. Mod. Phys. **21**, 378382, (1949).

[83] A. Einstein, *On the Motion of Small Particles Suspended in Liquids at Rest Required by the Molecular−Kinetic Theory of Heat**, Web Resource http://www.math.princeton.edu/∼mcmillen/molbio/papers/Einstein_diffusion.pdf
*Originally published in Ann. d. Phys. **17**, 549-560, (1905).

[84] A.A. Michelson and E.H. Morley, *On the relative motion of the earth and the luminiferous ether*, Am. J. Sci. **34**, 333-345.

[85] H. Müller, S. Herrmann, C. Braxmaier, S. Schiller and A. Peters, *Precision test of the isotropy of light propagation*, Appl. Phys. B **77**, 719731, 2003.

[86] G. Stephenson and C.W. KilMister, *Special Relativity for Physicists.*

[87] M.A. Rothman, *Discovering the natural laws: The Experimental Basis of Phyiscs.*

[88] A. Brillet and J.L. Hall, *Improved Laser Test of the Isotropy of Space*, Phys. Rev. Letters **42**, No. 9, Page 549-552, 1979.

[89] P. Antonini, M. Okhapkin, E. Gökülü and S. Sciller, *Tests of constancy of speed of light with rotating cryogenic optical resonators*, Phys. Rev. A **71**, Page 050101(R)-050105(R), 2005.

[90] D. Hills and J.L. Hall, *Improved Kennedy−Thorndike Experiment to Test Special Relativity* , Phys. Rev. Lett. **64**, No. 15, Page 1697- 1700, 1990.

[91] D.A. Jennings, C.R. Pullock, F.R. Peterson, R.E. Drullinger, K.M. Evenson, J.S. Wells, J.L. Hall and H.P. Layer, *Direct frequency measurements of the I_2−stabilized He−Ne 473 THz (632 nm) laser*, Opt. Lett. **8**, Page 136- 138, 1983.

[92] D.A. Jennings, K.M. Evenson and D.J.E. Knight, *Optical Frequency Measurements*, Proc. IEEE **74**, Page 168- 179, 1986.

[93] C.R. Pollock, D.A. Jennings, F.R. Petersen, J.S. Wells, R.E. Drullinger, E.C. Beaty, and K.M. Evenson, *Direct frequency measurements of transitions at 520 THz (576 nm) in iodine and 260 THz (1.15 nm) in neon*, Opt. Lett. **8**, Page 133- 135, 1983.

[94] T.H. udem, J. Reichert, R. Holzwarth, and T.W. Hänsch, *Accurate measurements of large optical frequency differences with a mode−locked laser*, Opt. Lett. **24**, Page 881- 883, 1999.

[95] J. Reichert, R. Holzwarth, T.H. udem, and T.W. Hänsch, *Measuring the frequency of light with mode−locked lasers*, Opt. Comm. **172**, Page 59- 68, 1999.

[96] S. Schiller, C. Lämmerzahl, H. Müller, C. Braxmaier, S. Herrmann, and A. Peters, *Experimental limits for low−frequency space−time fluctuations from ultrastable optical resonators*, Phys. Rev. D **69**, Page 027504, 2003.

[97] H. Müller, S. Herrmann, A. Saenz, A. Peters, and C. Lämmerzahl, *Tests of Lorentz invariance using hydrogen molecules*, Phys. Rev D **70**, Page 076004, 2004.

[98] D. Colladay and V.A. Kostelecký, *Lorentz−violating extension of the standard model* Phys. Rev. D **58**, 116002, 1998.

[99] D. Colladay and V.A. Kostelecký, *CPT violation and the standard model* Phys. Rev. D **55**, 6760, 1997.

[100] M. Gehrtz, G.C. Bjorklund and E.A. Whittaker, *Quantum−limited laser frequency−modulation spectroscopy*, J. Opt. Soc. Amer. B, **2**, 1510-1526, 1985.

[101] J.W. Ekin and D.K. Wagner, *A Simple ac Bridge Circuit for Use in Four−Terminal Resistance Thermometry* Rev. Sci. Instrum. **41**, 1109, 1970.

[102] L.G. Rubin and Y. Golahny, *An Improved ac Bridge Circuit for Use in Four−Terminal Resistance Thermometry* Rev. Sci. Instrum. **43**, 1758, 1972.

[103] Z. Nichols, *Optimum settings for automatic controllers* Trans. ASME **64**, 759, 1942.

[104] *efunda Engineering Fundamentals* Web resource http://www.efunda.com/materials/elements/.

[105] H.M. Nussenzveig, *Diffraction Effects in Semiclassical Scattering* Cambridge University, Cambridge, UK, 1992.

[106] *ULE corning Zero expansion glass* Web resource http://www.besoptics.com/.

[107] *Ultra Low Expansion Glass Datasheet* Web resource http://www.corning.com/docs/specialtymaterials/pisheets/UleBro91106.pdf.

[108] S.A. Webster, M. Oxborrow and P. Gill *Subhertz−linewidth Nd:YAG Laser* Optics Letters **29**, 1497, 2004.

[109] S.A. Webster, M. Oxborrow and P. Gill *Vibration insensitive optical cavity* Phys. Rev. A **75**, 011801-(R), 2007.

[110] H. Stoehr, F. Mensing, J. Helmke and U. Sterr *Diode laser with 1 Hz linewidth* Optics Letters **31**, 736, 2006.

[111] *Table Stable* Web resource http://www.tablestable.biz/AVI−350−S.php.

[112] *Table Stable* Web resource http://www.tablestable.biz/pdf/Manual

[113] *Original Code Consulting* Web resource http://www.originalcode.com/programs_scientific.html#GaussianBeam

[114] E. Hecht, *Optics*, 2^{nd} edition, (1987), 583.

[115] B.E.A. Saleh and M.C. Teich, *Fundamental of Photonics*, Wiley−Interscience, New York, 1991, chapter 9.

[116] S.A. Webster, S. Pugla, M. Oxborrow and P. Gill, *High Stability Nd:YAG Laser*, European Space Agency Conference, 2005.

[117] M. Notcutt, L. Ma and J.L. Hall, *Simple and compact 1−Hz laser system via improved mounting configuration of a reference cavity*, Optics Letters **30**, 1815-1817, 2005.

[118] T. Nazarova, F. Riehle and U. Sterr, *Vibration−insensitive reference cavity for an ultra−narrow−linewidth laser* , Appl. Phys. B: Lasers Opt. **83**, 531, 2006.

[119] K. Numata, A. Kemery and J. Camp, *Thermal−Noise Limit in the Frequency Stabilization of Lasers with Rigid Cavities*, Phys. Rev. Lett. **93**, 250602, 2004.

[120] G.P. Barwood, P. Gill, H. Klein and W.R.C. Rowley, *Clearly resolved secular sidebands on the* $^2S_{1/2} - ^2 D_{5/2}$ *674−nm, clock transition in a single trapped* Sr^+ *ion*, IEE. Trans. Instr. Meas. **46**, 133-136, April 1997.

[121] K. Hosaka, S.A. Webster, P.J. Blythe, A. Stannard, D. Beaton, H.S. Margolis, S.N. Lea and P. Gill, *An optical frequency standard based on the electric octupole transition in* $^{171}Yb^+$, IEE. Trans. Instrum. Meas. **54**, 759, 2005.

[122] *COMSOL Multiphysics, version 3.2, COMSOL Ab., Stokholm, Sweden.* Available online at http://www.comsol.com/

[123] L. Chen, J.L. Hall, J. Ye, T. Yang, E. Zang and T. Li, *Vibration−induced elastic deformation of Fabry−Perot cavities*, Phys. Rev. A **74**, 053801, 2006.

[124] J.K. Ranka, R.S. Windeler, and A.J. Stentz, *Visible continuum generation in air−silica microstructure optical fibers with anomalous dispersion at 800 nm*, Opt. Lett., **25**, 2527, 2000.

[125] W.J. Wadsworth, J.C. Knight, A. Ortigosa−Blanch, J. Arriaga, E. Silvestre, and P.St.J. Russell, *Soliton effects in photonic crystal fibers at 850 nm*, Electron. Lett., **36**, 5354, 2000.

[126] D.J. Jones, S.A. Diddams, J.K. Ranka, A. Stentz, R.S. Windeler, J.L. Hall and S.T. Cundiff, *Carrier−envelope phase control of femtosecond mode−locked lasers and direct optical frequency synthesis*, Science, **288**, 635639, 2000.

[127] R. Holzwarth, Th. Udem, T.W. Hänsch, J.C. Knight, W.J. Wadsworth and P.St.J. Russell, *Optical frequency synthesizer for precision spectroscopy*, Phys. Rev. Lett.,**85**, 22642267, 2000.

[128] Th. Udem, S.A. Diddams, K.R. Vogel, C.W. Oates, E.A. Curtis, W.D. Lee, W.M. Itano, R.E. Drullinger, J.C. Bergquist and L. Hollberg, *Absolute frequency measurements of the Hg^+ and Ca optical clock transitions with a femtosecond laser*, Phys. Rev. Lett., *86*, 49964999, 2001.

[129] H. Schnatz, B. Lipphardt, J. Helmcke, F. Riehle and G. Zinner, *First phase−coherent frequency measurement of visible radiation*, Phys. Rev. Lett., **76**, 1821, 1996.

[130] J. Stenger, T. Binnewies, G. Wilpers, F. Riehle, H.R. Telle, J.K. Ranka, R.S. Windeler and A.J. Stentz, *Phase−coherent frequency measurement of the Ca intercombination line at 657 nm with a Kerr−lens mode−locked femtosecond laser*, Phys. Rev. A, *63*, 021802(R), 2001.

[131] M. Oxborrow, S.A. Webster and P. Gill, *Stability of Nd:YAG "flywheel" lasers locked to ultra−high−finesse etalons made from either ULE or mono−crystalline sapphire*, Proceedings of the Sixth Symposium on Frequency Standards and Metrology (World Scientific), 571-573, 2002.

[132] *Total emissivity ϵ in case of two concentric cylinders is given by $\epsilon = \frac{1}{\left(\frac{1}{\epsilon_1}+\frac{1-\epsilon_1}{\epsilon_2}\left(\frac{r_1}{r_2}\right)\right)}$, where ϵ_1, r_1 are the emissivity and radius of the first cylinder and ϵ_2, r_2 are the emissivity and radius of the second cylinder.*

[133] B. Willke , S. Brozek and K. Danzmann *Frequency stabilization of a monolithic Nd:YAG ring laser by controlling the power of the laser-diode pump source* Optics Letters, **25**, 1019-1021.

[134] T.J. Kane and E.A.P. Cheng *Fast frequency tuning and phase locking of diode pumped Nd:YAG lasers* Optics Letters, **13**, 970-972.

[135] Encyclopedia of Laser Physics and Technology *Nonplanar ring oscillators*, http://www.rp−photonics.com/nonplanar_ring_oscillators.html.

[136] Encyclopedia of Laser Physics and Technology *Fabry-Perot Interferometers*, http://www.rp−photonics.com/fabry_perot_interferometers.html.